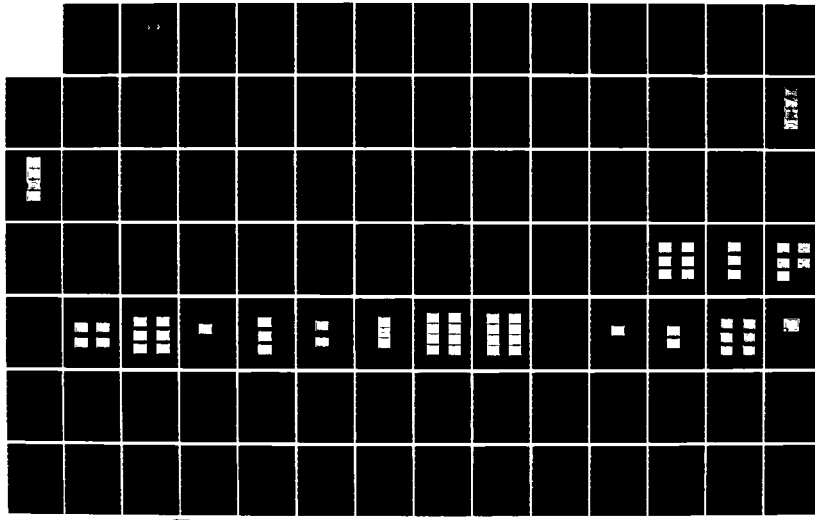


AD-A173 086 HIGH ENERGY SURGE ARRESTER TECHNOLOGY DEVELOPMENT PART 1/2
2(C) GENERAL ELECTRIC CO PHILADELPHIA PA SPACE SYSTEMS
DIV D M TASCA 28 FEB 86 86SDS4239 DNA-TR-86-85-PT-2
UNCLASSIFIED DNA001-82-C-0241 F/G 9/1 NL





MICROCOPY RESOLUTION TEST CHART
NATIONAL BUREAU OF STANDARDS-1963-A

AD-A173 086

(12)

DNA-TR-86-85-PT-2

HIGH ENERGY SURGE ARRESTER TECHNOLOGY DEVELOPMENT

Part II, Phase I

General Electric Company
Space Systems Division
Valley Forge Space Center
P. O. Box 8555
Philadelphia, PA 19101-8555



28 February 1986

Technical Report

CONTRACT No. DNA 001-82-C-0241

Approved for public release;
distribution is unlimited.

THIS WORK WAS SPONSORED BY THE DEFENSE NUCLEAR AGENCY
UNDER RDT&E RMSS CODES B326082466 X99QAXVC00009 H2590D
AND B326083466 X99QAXVC00009 H2590D.

DTIC FILE COPY

Prepared for
Director
DEFENSE NUCLEAR AGENCY
Washington, DC 20305-1000

86 10 21 054

DISTRIBUTION LIST UPDATE

This mailer is provided to enable DNA to maintain current distribution lists for reports. We would appreciate your providing the requested information.

- Add the individual listed to your distribution list.
- Delete the cited organization/individual.
- Change of address.

NAME: _____

ORGANIZATION: _____

OLD ADDRESS**CURRENT ADDRESS**

TELEPHONE NUMBER: () _____

SUBJECT AREA(s) OF INTEREST:

DNA OR OTHER GOVERNMENT CONTRACT NUMBER: _____

CERTIFICATION OF NEED-TO-KNOW BY GOVERNMENT SPONSOR (if other than DNA):

SPONSORING ORGANIZATION: _____

CONTRACTING OFFICER OR REPRESENTATIVE: _____

SIGNATURE: _____

UNCLASSIFIED

SECURITY CLASSIFICATION OF THIS PAGE

AD-A173086

REPORT DOCUMENTATION PAGE				Form Approved OMB No. 0704-0188 Exp. Date: Jun 30, 1986
1a. REPORT SECURITY CLASSIFICATION UNCLASSIFIED		1b RESTRICTIVE MARKINGS		
2a. SECURITY CLASSIFICATION AUTHORITY N/A since Unclassified		3. DISTRIBUTION / AVAILABILITY OF REPORT Approved for public release; distribution is unlimited.		
2b DECLASSIFICATION/DOWNGRADING SCHEDULE N/A since Unclassified				
4 PERFORMING ORGANIZATION REPORT NUMBER(S) 86SDS4239		5 MONITORING ORGANIZATION REPORT NUMBER(S) DNA-TR-86-85-PT-2		
6a. NAME OF PERFORMING ORGANIZATION General Electric Company Space Systems Division	6b OFFICE SYMBOL (If applicable)	7a. NAME OF MONITORING ORGANIZATION Director Defense Nuclear Agency		
6c. ADDRESS (City, State, and ZIP Code) Valley Forge Space Center P.O. Box 8555 Philadelphia, PA 19101-8555		7b. ADDRESS (City, State, and ZIP Code) Washington, DC 20305-1000		
8a. NAME OF FUNDING / SPONSORING ORGANIZATION	8b OFFICE SYMBOL (If applicable)	9 PROCUREMENT INSTRUMENT IDENTIFICATION NUMBER DNA 001-82-C-0241		
8c. ADDRESS (City, State, and ZIP Code)		10 SOURCE OF FUNDING NUMBERS		
		PROGRAM ELEMENT NO 62715H	PROJECT NO X99QAXV	TASK NO C
		WORK UNIT ACCESSION NO DH005668		
11. TITLE (Include Security Classification) HIGH ENERGY SURGE ARRESTER TECHNOLOGY DEVELOPMENT Part II, Phase I				
12 PERSONAL AUTHOR(S) Tasca, Danta M.				
13a. TYPE OF REPORT Technical	13b TIME COVERED FROM 820630 TO 860228	14 DATE OF REPORT (Year, Month, Day) 860228	15 PAGE COUNT 130	
16. SUPPLEMENTARY NOTATION This work was sponsored by the Defense Nuclear Agency under RDT&E RMSS Codes B326082466 X99QAXVC00009 H2590D and B326083466 X99QAXVC00009 H2590D.				
17 COSATI CODES		18 SUBJECT TERMS (Continue on reverse if necessary and identify by block number) High Energy Surge Arrester Solid State Arrester Self Recovering Arrester Metal Oxide Varistor Saturable Magnetics		
19 ABSTRACT (Continue on reverse if necessary and identify by block number) This document is Part II of the final technical report for Phase I of Defense Nuclear Agency Contract DNA 001-82-C-0241 "High Energy Surge Arrester Technology Development." The overall objective of this program was the development of improved high energy surge arresters (HESAs) to protect installations from EMP induced on extended networks. The EMP threat was defined in terms of a composite threat envelope which embodied the high frequency aspects of high altitude EMP (HEMP), the high current level of source region EMP (SREMP) and the high charge level of nuclear induced lightning (NIL). The installations of concern included power lines, C³ lines and antennas.				
20 DISTRIBUTION AVAILABILITY OF ABSTRACT <input type="checkbox"/> UNCLASSIFIED UNLIMITED <input checked="" type="checkbox"/> SAME AS RPT <input type="checkbox"/> DTIC USERS		21 ABSTRACT SECURITY CLASSIFICATION UNCLASSIFIED		
22a. NAME OF RESPONSIBLE INDIVIDUAL Betty L. Fox		22b. TELEPHONE (Include Area Code) (202) 325-7042	22c. OFFICE SYMBOL DNA/STI	

DD FORM 1473, 84 MAR

83 APR edition may be used until exhausted

All other editions are obsolete

SECURITY CLASSIFICATION OF THIS PAGE

UNCLASSIFIED

UNCLASSIFIED

SECURITY CLASSIFICATION OF THIS PAGE

19. ABSTRACT (Continued)

This phase

distribution system and is documented in a companion volume. Part II of Phase I, which is the subject of this volume, is associated with the development of a HESA for an RF/C³ transmitter antenna.

The present program has shown that improved HESAs can be developed for practical RF/C³ applications. A unique and innovative all solid state, self recovery HESA design concept was developed using existing metal oxide varistor and saturable magnetic device technologies. This design concept, which is based on a two element hybrid protective device approach, has the dual capability to provide high voltage/fast rise time and long pulse/high current threat protection. The first element provides delay-free protection against the fast risetime HEMP threat and was implemented using our metal oxide power varistor product line technology which General Electric developed. The second element provides the high energy relief for the first element, and was implemented using saturable magnetics.

Detailed analytical design equations were derived and extensive material characteristics were experimentally obtained in support of this development. Much of this work involved the generation of singular information which was required to support the solutions to the design problems encountered in meeting the design challenge using realistic hardware. Two proof-of-principle prototype units were designed and fabricated using the technology established in the program.

Based on the positive results obtained to date, and the interest exhibited by the survivability technical community, it is recommended that the Phase II portion of the program be initiated in order to establish detailed performance evaluations of the prototypes. Based on a successful conclusion of the Phase II work it would be further recommended that additional work be undertaken to optimize the performance characteristics achievable with the various elements comprising the HESA. It is envisioned that the HESA technology developed under this program can be transferred to use in operational systems once this is achieved.

SECURITY CLASSIFICATION OF THIS PAGE

UNCLASSIFIED

PREFACE

This report was prepared by the General Electric Company, Space Systems Division, Philadelphia, Pennsylvania, under Defense Nuclear Agency Contract DNA001-82-C-0241. Technical monitoring of the contract at the Defense Nuclear Agency was under the direction of George Baker and Major William Farmer. The program manager at General Electric was Joseph Peden and the principal investigator was Dante Tasca.

The author wishes to acknowledge the following individuals for their contributions to the work reported herein: M. Bortulin, D. Noble, B. Pokol, D. Swant and R. Yadavalli of General Electric, Space Systems Division; S. Korn and B. Wolff of General Electric, Semiconductor Products Department; G. Foster of Hill Air Force Base; M. Bell and A. Peterson of JAYCOR; M. Chalet of Ceramic Magnetics Incorporated; and, W. Martin of Magnetics Incorporated.

Accesion For	
NTIS CRA&I	<input checked="" type="checkbox"/>
DTIC TAB	<input type="checkbox"/>
Unannounced	<input type="checkbox"/>
Justification	
By	
Distribution /	
Availability Codes	
Dist	Avail and/or Special
A-1	

CONVERSION TABLE

Conversion factors for U.S. Customary to metric (SI) units of measurement

MULTIPLY TO GET	BY	TO GET DIVIDE
	BY	
angstrom	1.000 000 X E -10	meters (m)
atmosphere (normal)	1.013 25 X E +2	kilo pascal (kPa)
bar	1.000 000 X E +2	kilo pascal (kPa)
barn	1.000 000 X E -28	meter ² (m ²)
British thermal unit (thermochemical)	1.054 350 X E +3	joule (J)
calorie (thermochemical)	4.184 000	joule (J)
cal (thermochemical)/cm ²	4.184 000 X E -2	mega joule/m ² (MJ/m ²)
curie	3.700 000 X E +1	*giga becquerel (GBq)
degree (angle)	1.745 329 X E -2	radian (rad)
degree Fahrenheit	$T_K = (T^{\circ}F + 459.67)/1.8$	degree kelvin (K)
electron volt	1.602 19 X E -19	joule (J)
erg	1.000 000 X E -7	joule (J)
erg/second	1.000 000 X E -7	watt (W)
foot	3.048 000 X E -1	meter (m)
foot-pound-force	1.355 818	joule (J)
gallon (U. S. liquid)	3.785 412 X E -3	meter ³ (m ³)
inch	2.540 000 X E -2	meter (m)
jerk	1.000 000 X E +9	joule (J)
joule/kilogram (J/kg) (radiation dose absorbed)	1.000 000	Gray (Gy)
kilotons	4.183	terajoules
kip (1000 lbf)	4.448 222 X E +3	newton (N)
kip/inch ² (ksi)	6.894 757 X E +3	kilo pascal (kPa)
ktap	1.000 000 X E +2	newton-second/m ² (N-s/m ²)
micron	1 000 000 X E -6	meter (m)
mil	2.540 000 X E -5	meter (m)
mile (international)	1.609 344 X E +3	meter (m)
ounce	2.834 952 X E -2	kilogram (kg)
pound-force (lbs avoirdupois)	4.448 222	newton (N)
pound-force inch	1.129 846 X E -1	newton-meter (N-m)
pound-force/inch	1.751 268 X E +2	newton/meter (N/m)
pound-force/foot ²	4.788 026 X E -2	kilo pascal (kPa)
pound-force/inch ² (psi)	6.894 757	kilo pascal (kPa)
pound-mass (lbm avoirdupois)	4.535 924 X E -1	kilogram (kg)
pound-mass-foot ² (moment of inertia)	4.214 011 X E -2	kilogram-meter ² (kg·m ²)
pound-mass/foot ³	1.601 846 X E +1	kilogram/meter ³ (kg/m ³)
rad (radiation dose absorbed)	1.000 000 X E -2	**Gray (Gy)
roentgen	2.579 760 X E -4	coulomb/kilogram (C/kg)
shake	1.000 000 X E -8	second (s)
slug	1.459 390 X E +1	kilogram (kg)
torr (mm Hg, 0° C)	1.333 22 X E -1	kilo pascal (kPa)

*The becquerel (Bq) is the SI unit of radioactivity; 1 Bq = 1 event/s.

**The Gray (Gy) is the SI unit of absorbed radiation.

TABLE OF CONTENTS

Section	Page
PREFACE.....	iii
CONVERSION TABLE.....	iv
LIST OF ILLUSTRATIONS.....	vi
LIST OF TABLES.....	x
1 INTRODUCTION.....	1
2 HESA PROTECTION REQUIREMENTS AND DESIGN APPROACH.....	3
3 METAL OXIDE VARISTOR ELEMENT.....	8
3.1 AC Equivalent Circuit.....	9
3.2 Voltage-Current Characteristics.....	11
3.3 Dielectric Characteristics.....	13
3.4 RF Loss Characteristics.....	18
3.5 RF Self Heating Loss Reduction Methods.....	25
3.6 High Energy Absorption Capability.....	33
4 SATURABLE MAGNETICS ELEMENT.....	35
4.1 AC Equivalent Circuit.....	35
4.2 Switching Characteristics.....	35
4.3 Permeability Characteristics.....	52
4.4 RF Loss Characteristics.....	58
4.5 RF Self Heating and Thermal Stress Reduction Methods.....	62
4.6 Optimization of the Saturable Magnetic Device Configuration.....	76
5 PROTOTYPE DESIGN.....	88
5.1 Saturable Magnetics Design.....	89
5.2 Metal Oxide Varistor Design.....	93
5.3 Prototype Configuration.....	98
6 CONCLUSIONS AND RECOMMENDATIONS.....	110
7 LIST OF REFERENCES.....	111

LIST OF ILLUSTRATIONS

Figure		Page
1	Generalized RF/C ³ HESA concept.....	5
2	"Metal oxide varistor - saturable magnetics" solid state HESA switching characteristics.....	6
3	AC equivalent circuit of the medium voltage type GE-MOV® Varistor material.....	10
4	Idealized voltage current characteristics for a 1Ω - cm medium voltage varistor.....	12
5	Pulse response characteristics of the X531 GE-MOV® Varistor (2.54 mm thick and 1.14 cm contact diameter - V @ 1 mA DC = 350 volts).....	14
6	Pulse response characteristics of the X532 GE-MOV® Varistor (2.92 mm thick and 1.14 cm contact diameter - V @ 1 mA DC = 600 volts).....	15
7	Pulse V-I characteristics of the X531 GE-MOV® Varistor.....	16
8	AC dielectric characteristics of DD medium voltage GE-MOV® Varistors.....	17
9	Specific reactance of various medium voltage GE-MOV® Varistors.....	19
10	Varistor geometry and equivalent circuit for RF loss analyses.....	21
11	GE-MOV® Varistor insertion loss equivalent circuit.....	21
12	Maximum RF standby power capability of X531 GE-MOV® Varistors.....	26
13	Maximum RF standby power capability of X532 GE-MOV® Varistors.....	27
14	"RF Self Heating" loss reduction technique for high power, high frequency varistor applications.....	29
15	Equivalent circuit for the varistor "RF Self Heating" loss reduction technique.....	29
16	Pulse forward V-I characteristics of the Unitrode IN5811 diode.....	31
17	Capacitive reactance of the Unitrode IN5811 diode.....	31

LIST OF ILLUSTRATIONS

Figure		Page
18	Pulse ratings of typical medium voltage GE-MOV® Varistors.....	34
19	Simplified AC equivalent circuit of a saturable magnetic device.....	36
20	Toroidal core of magnetic material.....	37
21	Device switching characteristics - 6 turns on a Magnetics Incorporated F43813 toroid.....	40
22	Device saturation recovery characteristics - 4 turns on a Magnetics Incorporated F43813 toroid.....	41
23	Device saturation charge characteristics - 6 turns on a Magnetics Incorporated F43813.....	42
24	Device high saturation charge characteristics - 6 turns on a Magnetics Incorporated F43813 toroid.....	44
25	Device switching characteristics - 6 turns on a Magnetics Incorporated F43813 toroid with a 10 mil gap.....	45
26	Device saturation recovery characteristics - 4 turns on a Magnetics Incorporated F43813 toroid with a 10 mil gap.....	46
27	Device saturation charge characteristics - 6 turns on a Magnetic Incorporated F43813 toroid with a 10 mil gap.....	47
28	Device high saturation charge characteristics - 6 turns on a Magnetics Incorporated F43813 toroid with a 10 mil gap.....	48
29	Device switching characteristics - solid rod through 10 Magnetics Incorporated F42206 toroids.....	49
30	Device switching and residual magnetism characteristics - 6 turns on a Ceramic Magnetics Incorporated CMD5005 toroid.....	50
31	Device switching and residual magnetism characteristics - 6 turns on a Ceramic Magnetics Incorporated CN20 toroid.....	51
32	Device saturation recovery characteristics - 6 turns on a Ceramic Magnetics Incorporated CMD5005 toroid.....	53
33	Device saturation recovery characteristics - 6 turns on a Ceramic Magnetics Incorporated CN20 toroid.....	54

LIST OF ILLUSTRATIONS

Figure	Page
34 Device switching and residual magnetism characteristics - 6 turns on a Ceramic Magnetics Incorporated CM5005/84-17-3 toroid with a 10 mil gap.....	55
35 Comparison of experimental and calculated "V-t" saturation levels for 6 turns on a Ceramic Magnetics Incorporated CMD5005/84-17-3 toroid with a 10 mil gap.....	56
36 Equivalent circuit of a magnetic toroid containing a gap.....	57
37 Relative permeability of Ceramic Magnetics Incorporated CMD5005 ferrite materials.....	59
38 Saturable magnetic device insertion loss equivalent circuit.....	60
39 Free air core loss characteristics of Magnetics Incorporated Type F material at 30 MHz as a function of toroid turns.....	63
40 Core loss characteristics - 3 turns on a Magnetics Incorporated F41306 toroid.....	64
41 Core loss characteristics - 10 turns on a Magnetics Incorporated F41306 toroid.....	65
42 Core loss characteristics - 3 turns on a Magnetics Incorporated F42206 toroid.....	66
43 Core loss characteristics - 3 turns on a Magnetics Incorporated F43813 toroid.....	67
44 Core loss characteristics - 6 turns on a Magnetics Incorporated F43813 toroid.....	68
45 Core loss characteristics - solid rod through 10 Magnetics Incorporated F41306 toroids.....	69
46 Core loss characteristics - 3 turns on a Ceramic Magnetics Incorporated CN20 toroid.....	70
47 Core loss characteristics - 3 turns on a Ceramic Magnetics Incorporated CMD5005 toroid.....	71
48 Core loss characteristics - 10 turns on a Ceramic Magnetics Incorporated CMD5005 toroid.....	72
49 Core loss characteristics - 30 turns on a Ceramic Magnetics Incorporated CMD5005 toroid.....	73

LIST OF ILLUSTRATIONS

Figure		Page
50	Core loss characteristics - 3 turns on a Ceramic Magnetics Incorporated MN60 toroid.....	74
51	Core loss characteristics - 3 turns on a Ceramic Magnetics Incorporated MN80 toroid.....	75
52	Core loss characteristics of the Figure 43 device after reconfiguring back to toroid form with a 10 mil total RTV gap.....	77
53	Core loss characteristics - 3 turns on a Ceramic Magnetics Incorporated CMD5005/84-17-3 toroid with a 10 mil RTV gap.....	78
54	Core loss characteristics - 8 turns on a Ceramic Magnetics Incorporated CMD5005/84-17-3 toroid with a 10 mil RTV gap.....	79
55	Coaxial geometry of magnetic material.....	81
56	Coaxial configuration of the saturable magnetics element of the prototype HESA.....	89
57	Equivalent capacitance circuit for each of the two diode/varistor strings used in the prototype HESA.....	94
58	Schematic diagram of the prototype HESA.....	98
59	Total parts content of the prototype HESA.....	99
60	Total parts content of the diode/varistor/capacitor assembly.....	100
61	Diode/varistor/capacitor subassembly.....	101
62	Total parts content of the saturable magnetics subassembly.....	102
63	Saturable magnetics subassembly.....	103
64	Total parts content of the housing subassembly.....	104
65	Housing subassembly.....	105
66	Housing, saturable magnetics and diode/varistor/ capacitor subassemblies.....	106
67	Completely assembled prototype HESA.....	107

LIST OF TABLES

Table		Page
1	Maximum RF standby power capability of Unitrode IN5811 diodes combined with GE-MOV® Varistors.....	32
2	Ferrite toroidal cores evaluated for basic device response characterizations.....	36
3	Thermal stability test results for Ceramic Magnetics Incorporated dielectrically gapped CMD5005 toroids (a = 1.27 cm, b = 2.72 cm, s = 0.889 cm).....	86
4	Low level input impedance characteristics of a prototype HESA at various stages of assembly.....	108
5	Medium power VSWR characteristics of a 50 ohm terminated prototype HESA with internal capacitors removed.....	109
6	Low power VSWR characteristics of a 50 ohm terminated prototype HESA.....	109

SECTION 1

INTRODUCTION

This document is Part II of the Final Technical Report for Phase I of DNA Contract DNA001-82-C-0241, "High Energy Surge Arrester Technology Development." The overall objective of the program was the development of improved high energy surge arresters (HESA's) to protect installations from EMP induced on extended networks. The EMP threat was defined in terms of a composite threat envelope which embodied the high frequency aspects of high altitude EMP (HEMP), the high current level of source region EMP (SREMP) and the high charge level of nuclear induced lightning (NIL). The installations of concern included power lines, C³ lines and antennas.

The program was divided into two separate phases. Phase I was concerned with HESA development and fabrication of two proof-of-principle prototype units for each of two separate applications. Phase II will address the detailed performance evaluation of the prototypes. Part I of Phase I was associated with the development of a HESA for a power distribution system and is documented in a companion volume. Part II of Phase I, which is the subject of this volume, is associated with the development of a HESA for an RF/C³ transmitter antenna.

The HESA developments were implemented using a low-risk approach in that they did not require any new device/technology breakthroughs to be created, but rather represented reasonable extensions of presently available technology. The key feature of the HESA design concept was to develop a two element hybrid protective device which had the dual capability to provide high voltage/fast rise time and long pulse/high current threat protection. The first element was implemented using General Electric (GE) developed metal oxide power varistor product line technology. At the present time GE is a world-wide supplier of zinc oxide

to OEM suppliers of surge arresters as well as the leading manufacturer of zinc oxide surge arresters. The second element provides the high energy relief for the first element, and was implemented using a saturable magnetic device concept for the RF/C³ HESA.

The overall design which was developed here represents an all solid state, self recovering HESA and is described in detail in the following sections.

SECTION 2

HESA PROTECTION REQUIREMENTS AND DESIGN APPROACH

The "proof-of-principle" prototype HESA was developed for use in the generic RF/C³ application as described below (Reference 2.1):

- 50 ohm RF transmitter
- 2 kW peak power (1 kW RMS)
- 2-30 MHz operating frequency, with a 100 MHz upper limit goal

The imposed threat, as obtained from generic system analyses (Reference 2.2), which was used in the HESA design was as follows:

- 600 KV open circuit voltage
- 10 KA short circuit current
- 30 ns rise time
- 2 ms pulse width
- 5 pulses, 1 second apart

The corresponding HESA protection requirements (Reference 2.1) for this application/threat model were defined as follows:

- clamp line to \leq 900 Volts
- self recover
- insertion loss \leq 2 db

Spark gaps have been the traditional approach used to protect high power RF transmitters against pulsed power threats. Spark gaps, on one hand, are attractive since they have a very low insertion loss and clamp at a very low level when turned on. They do, however, have a dV/dt dependency as well as total charge capability limitations. There are also some concerns with respect to self-recovery when placed across very high power transmitter outputs. The initial design concept for the HESA was to provide an approach to augment a spark gap whereby the dV/dt and total charge limitations would be negated as well as any self recovery considerations.

One such design concept which had been previously conceived at General Electric, and which utilizes solid state components, would be as shown in Figure 1. Here a metal oxide varistor (MOV) device is used to provide instantaneous voltage clamping capability at a moderate voltage level with a minimal dV/dt response. The spark gap triggers at some time later at this moderate voltage level, but in a time well in advance of when the MOV energy limit is reached. Once the spark gap triggers, the voltage drops to below the MOV conduction point and the MOV turns off. Even as the spark gap is conducting the "voltage-time" product across a saturable magnetic device is building up. Once the "Vt" product reaches the saturation level of the magnetic device and at a time well in advance of the spark gap reaching its total charge limitation, the material is switched from a "high μ " condition to a " $\mu = 1$ " condition, with a corresponding decrease in impedance. Current is eventually all transferred to the saturated inductor at a low voltage corresponding to the "IR" drop across the inductor wiring. At this point the spark gap turns off and the assembly will continue to clamp at a very low voltage value until the threat is removed. At this point, the magnetic device is taken out of saturation and reset to its initial state providing a material with low residual magnetism is used.

It became obvious in considering this design approach that one desirable simplification would be to eliminate the spark gap and utilize the "Vt" switching of the inductive element to "off-load" the MOV well before its energy limit was reached. The qualitative switching characteristics of this all solid state design concept are shown in Figure 2. The MOV is again used to provide instantaneous clamping of the imposed threat. At time " t_1 " when the "Vt" product for saturation is reached, the inductor is switched from a high impedance to a low impedance. Current now begins to be transferred from the MOV to the saturated inductor. The transfer time " $t_2 - t_1$ " is controlled by the "L/R" time constant of the saturated inductor and the effective MOV resistance. Since the MOV clamps at a somewhat constant value its effective instantaneous resistance increases as the current through it decreases. Hence the L/R time constant is non-linear and of such a nature as speed up the current transfer time.

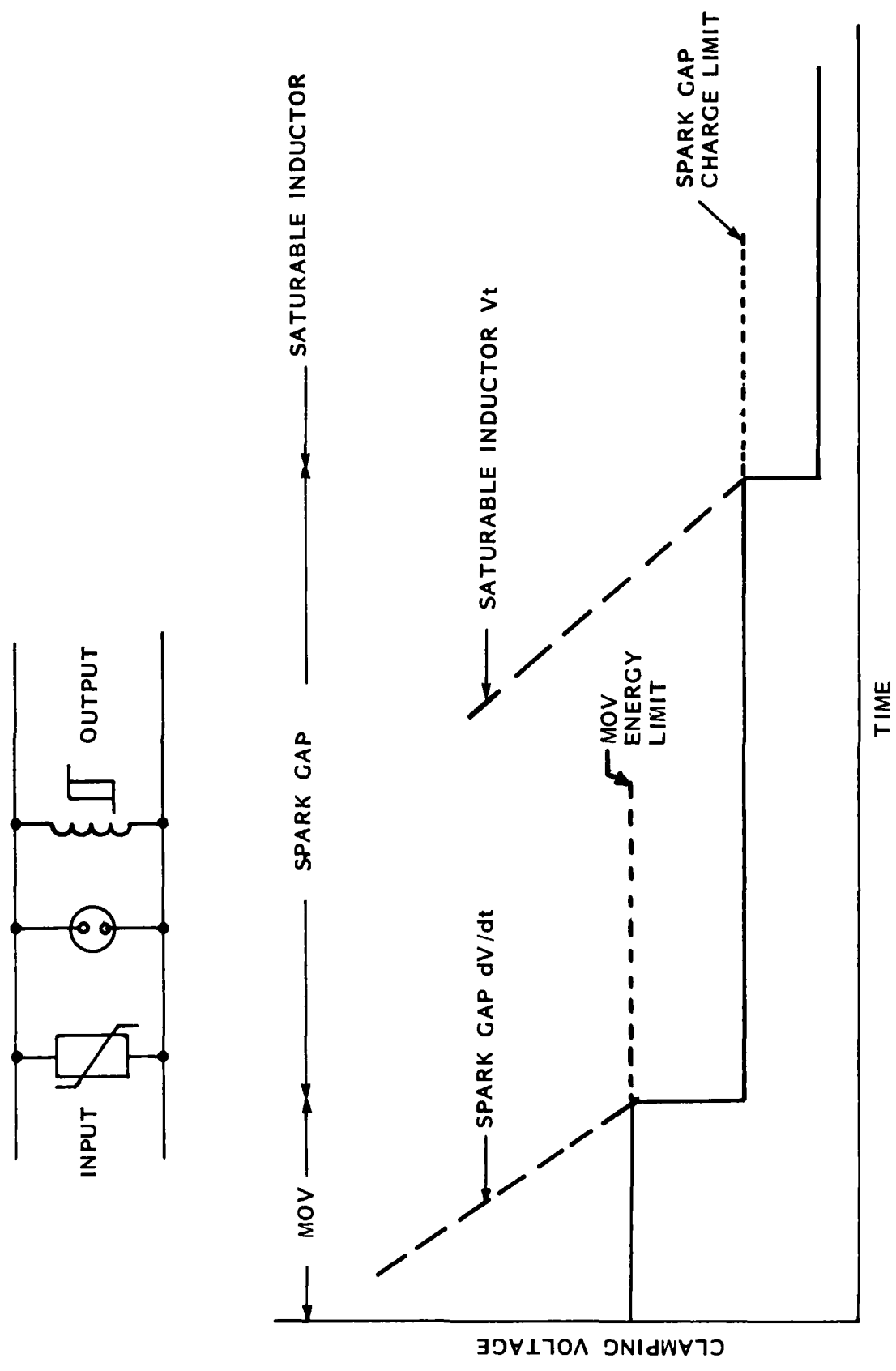


Figure 1. Generalized RF/C³ HESA concept.

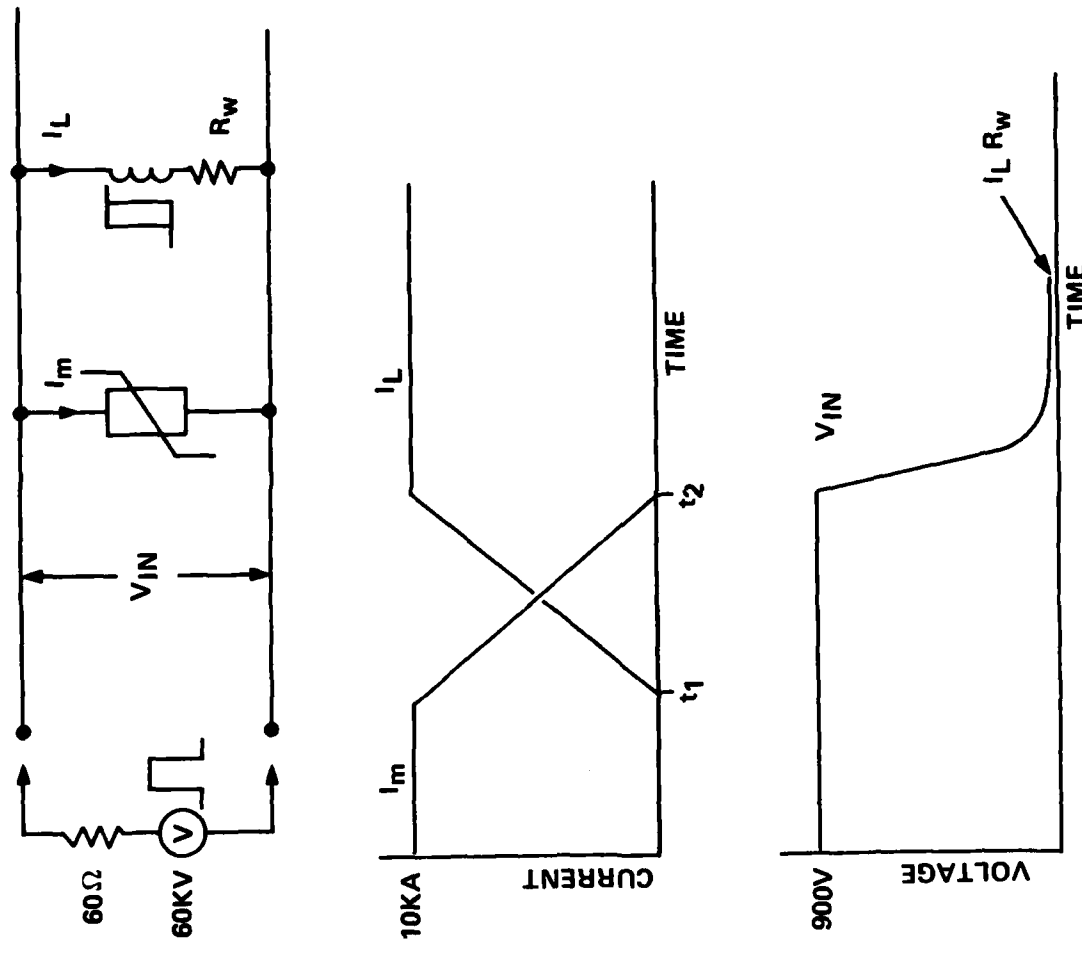


Figure 2. "Metal oxide varistor - saturable magnetics" solid state HESA switching characteristics.

At time "t₂" when all high current is removed from the MOV, its voltage drop falls below its clamping voltage value and continues to fall as current is continually decreased below milliamperes/cm² current densities until the level corresponding to the "IR" drop across the inductor wiring is reached.

The all state concept, using metal oxide varistor and saturable magnetics, was the design approach selected for the HESA prototype development in the program. The analytical design equations and experimental material characteristics which were developed for each of the two major elements in the HESA are described in detail in the following sections together with the specific design details of the two prototype units which were fabricated.

SECTION 3

METAL OXIDE VARISTOR ELEMENT

The General Electric metal oxide varistor (GE-MOV®) is a ceramic material which offers a unique property of highly non-linear resistance (varistor) and large energy absorbing capability. The varistor, when connected in an electrical circuit, exhibits, over a wide current range, a power law relationship between the current (I) flowing through the material and the voltage (V) across the terminals. This relationship is in the form: " $I = (V/C)^N$ " where C and N are constants, reflecting composition and geometry parameters, and are primarily a bulk property of the material. The exponent N will typically have values from 25 to 50 or more, leading to a characteristic very similar to that of a Zener diode. Older varistor materials by comparison have exponents on the order of 5. Over a wide current range, the voltage remains within a very narrow band for a specific device, and is referred to as the "varistor voltage" for that device. The value of this varistor (or clamping) voltage for a particular device is linearly dependent upon the thickness of the conduction path through the device; the thicker the material, the higher the varistor voltage. The material is bipolar in that the nonlinear resistance characteristic holds for both positive and negative polarity current. Also, the bulk properties of the material provide an inherent high energy absorbing capability, because energy dissipation is evenly distributed throughout the bulk.

The varistor possesses very fast current switching characteristics, being able to switch high current, subnanosecond rise time transients without any measurable time delay. Further, its electrical characteristics are a function of material properties and geometrical shape. As noted previously, the clamping voltage is a direct linear function of thickness of the material between the conduction electrodes. Because of this geometrical dependence, the application of this material as a transient protection device is quite flexible in achieving optimum configurations.

The material can be readily pressed, sliced, machined, etc., into a variety of shapes; such as cylinders, disks, doughnuts, squares, and so forth, and still maintain desirable electrical characteristics.

The varistor characteristics presented below consist of a detailed description of the analytical and singular experimental data obtained under this program together with a brief summary of the detailed measurements previously obtained under government contract together with the results of internal General Electric Company measurements. The information is presented in terms of geometry independent material parameters rather than absolute values related to specific geometrical configurations. In this way, one can perform a parametric analysis to select the optimum geometrical configuration to satisfy a specific application from the definition of such items as the quiescent bias, clamping voltage, pulse energy threat and insertion loss requirements. For brevity, the data summary is presented in terms of the characteristics associated with the standard medium voltage type material fabricated by the General Electric Company, Semiconductor Products Department, since it was the only material type considered in the present study.

3.1 AC EQUIVALENT CIRCUIT.

A suitable equivalent circuit which describes the electrical operation of the varistor material for AC conditions is shown in Figure 3. The circuit consists of the parallel combination of a capacitance (due to the very thin dielectric of the intergranular phase), a high resistance leakage resistor (attributable to the high resistivity of the bismuth oxide in the intergranular phase), and a nonlinear conduction element-varistor element- (associated with the intergranular phase) in series with a low resistance resistor (due to the low resistivity of the zinc oxide grains). Any application of wire leads, etc., to the material would, of course, result in the addition of a series inductance to the equivalent circuit in a manner similar to that associated with other electronic devices.

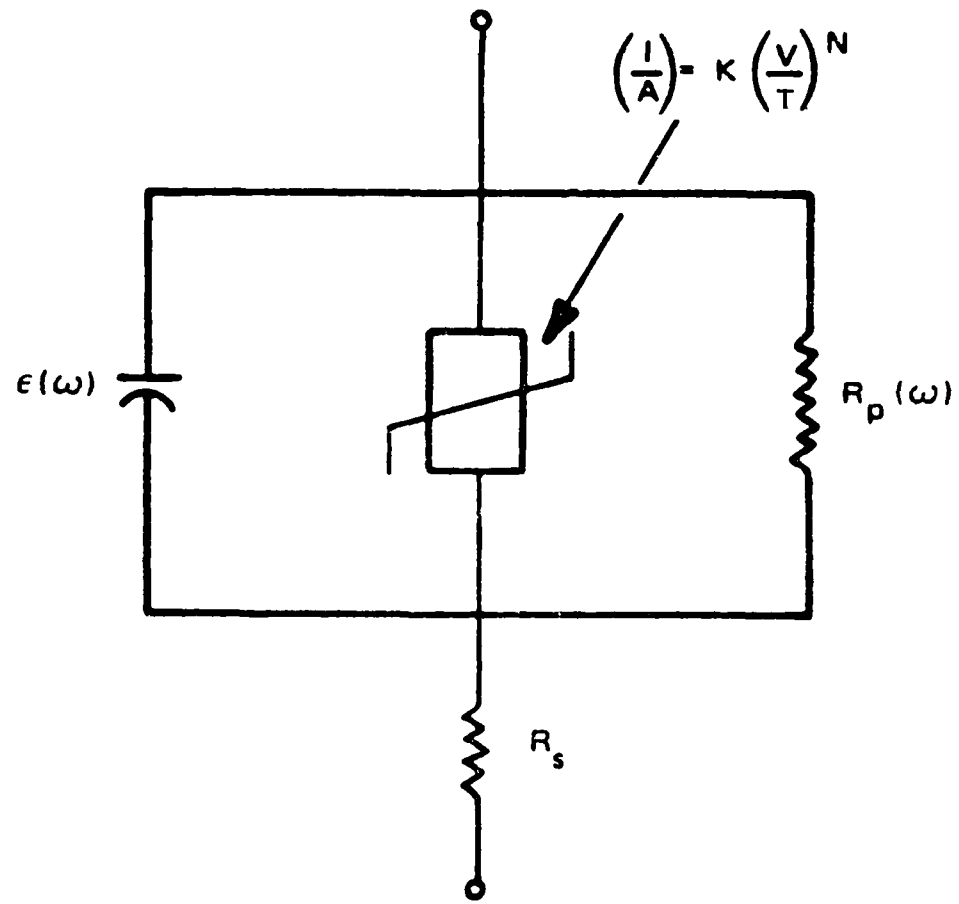


Figure 3. AC equivalent circuit of the medium voltage type GE MOV^R varistor material.

The bulk conduction properties of the varistor material are manifested in the V-I relationship for the varistor element as shown in Figure 3. As indicated, the voltage drop across the element is linearly related to the thickness, "T", of varistor material between conducting electrodes and the current density (current "I" and cross-sectional area "A") through the material. The coefficient of non-linearity, "N", typically has values on the order of 25 to 50. The parallel resistance and capacitance are frequency dependent and is further discussed in Section 3.3. The series resistivity is relatively small (being between 0.1 and 1 ohm-cm, dependent on material type) and, for the frequencies of concern in the present study, independent of frequency.

3.2 VOLTAGE-CURRENT CHARACTERISTICS.

The idealized voltage-current characteristics of a typical medium voltage varistor material is shown in Figure 4 (Reference 3.1). The varistor characteristics are given for a range of over eleven orders of magnitude in operating current density. Shown here is the relationship of the voltage drop per millimeter of material thickness to the amperes per square centimeter current density operating level for the varistor material. DC measurements are normally used to obtain the varistor characteristics for current densities less than 10 milliamperes/cm². Higher current density characteristics are obtained from pulse measurements.

Below about 10⁻⁸ amperes/cm², the conduction characteristics are controlled by the leakage characteristics of the high resistivity bismuth oxide insulator. Above 10⁻⁸ amperes/cm², the conduction characteristics are controlled by the high non-linearity of the intergranular phase. In the region beyond 10³ amperes/cm², the departure from high non-linear conduction is due to the voltage drop across the low resistivity zinc oxide grains.

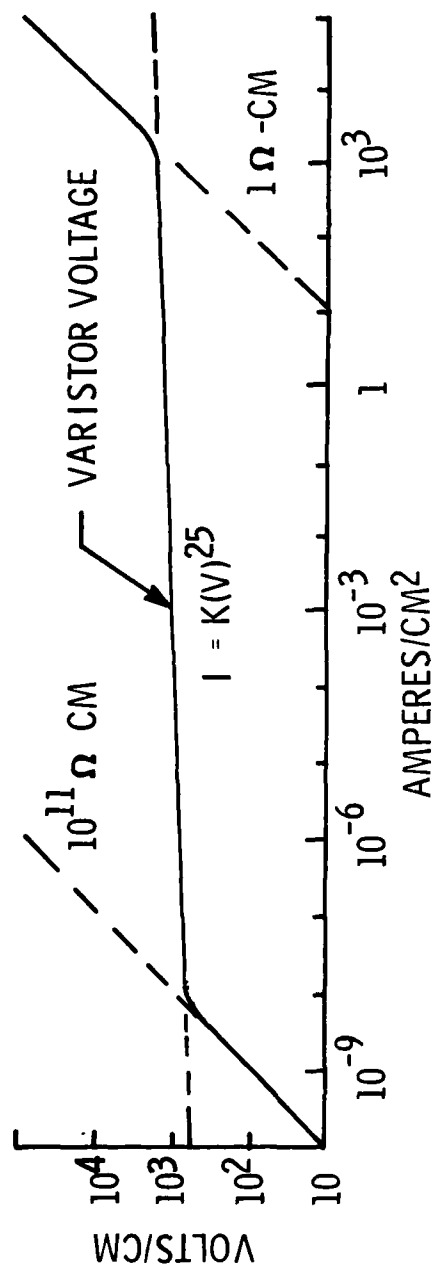


Figure 4. Idealized voltage current characteristics for a 1Ω -cm medium voltage varistor.

Two different types of medium voltage varistor materials were evaluated in the present program for use in the HESA prototype. These consisted of 140 and 210 volt/mm materials which are contained in specific units such as the X531 and X532 GE-MOV® devices respectively. Figure 5 shows the pulse response voltage clamping characteristics which were obtained for the X531 device when subjected to kiloampere level currents of less than 10 nanoseconds rise time. Figure 6 shows the similar characteristics obtained for the X532 device. The V-I characteristics which are derived from this type of data are shown in Figure 7 for the X531 device. Here, one can determine that the X531 device exhibits a coefficient of non-linearity "N" in the high current region of about 20 and a series resistivity of 0.36 ohm-cm.

3.3 DIELECTRIC CHARACTERISTICS.

In the unenergized state the metal oxide varistor is essentially a ceramic material which is primarily capacitive due to the dielectric nature of the intergranular phase. Levinson and Philipp (Reference 3.2) performed a detailed evaluation of the dielectric behavior of the metal oxide varistor over a frequency range from 10 Hz to 1GHz. Their results, which are given in Figure 8 for the Type DD medium voltage material, show that the dielectric constant and parallel resistivity are both frequency dependent. At 100 MHz this varistor material has a dielectric constant of 875 and a Q of 50. The Q is somewhat constant with frequency, exhibiting a minimum of 10 at 250 KHz.

It should be noted that, in evaluating the dielectric constant of a material, a common procedure is to perform impedance or reflection coefficient measurements on standard geometrical shapes such as parallel plate or coaxial configurations. These measurements are then related back to the sample geometry to define the dielectric constant of the material. Measurements such as these when applied to the GE-MOV® varistor yield an "effective" or "observed" value of dielectric constant when related to the overall varistor geometry rather than to the intergranular phase which is the source of the dielectric nature of the material. This is due to the fact that the overall geometry is composed primarily of

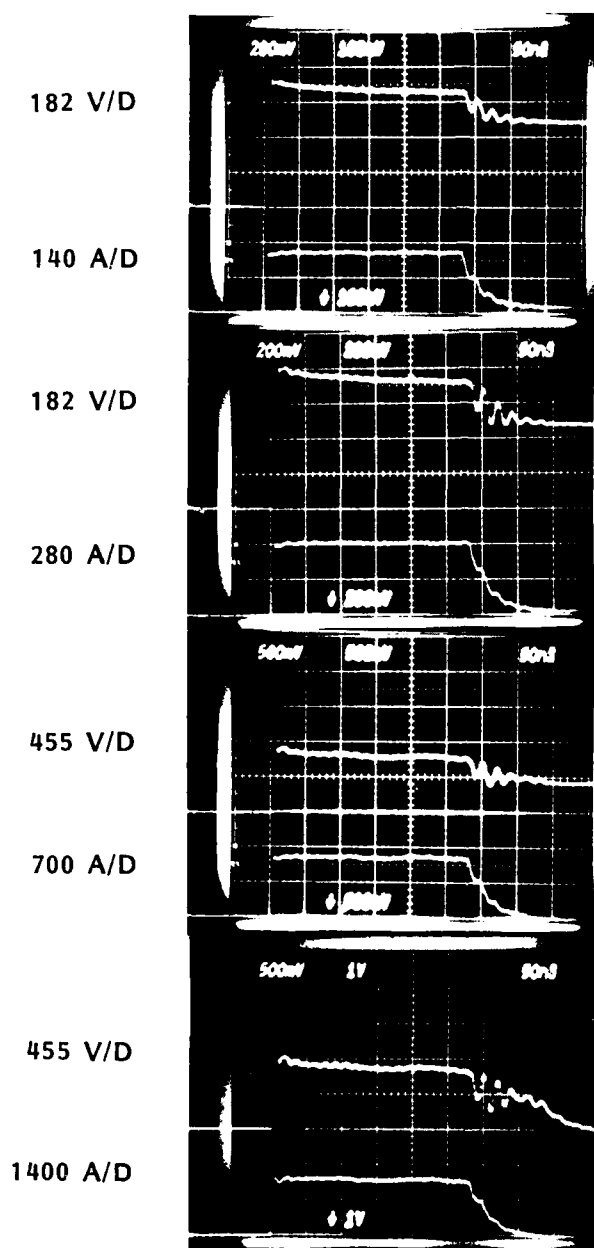


Figure 5. Pulse response characteristics of the X531 GE-MOV^R varistor
(2.54 mm thick and 1.14 cm contact diameter - V @ 1 mA DC
= 350 volts).

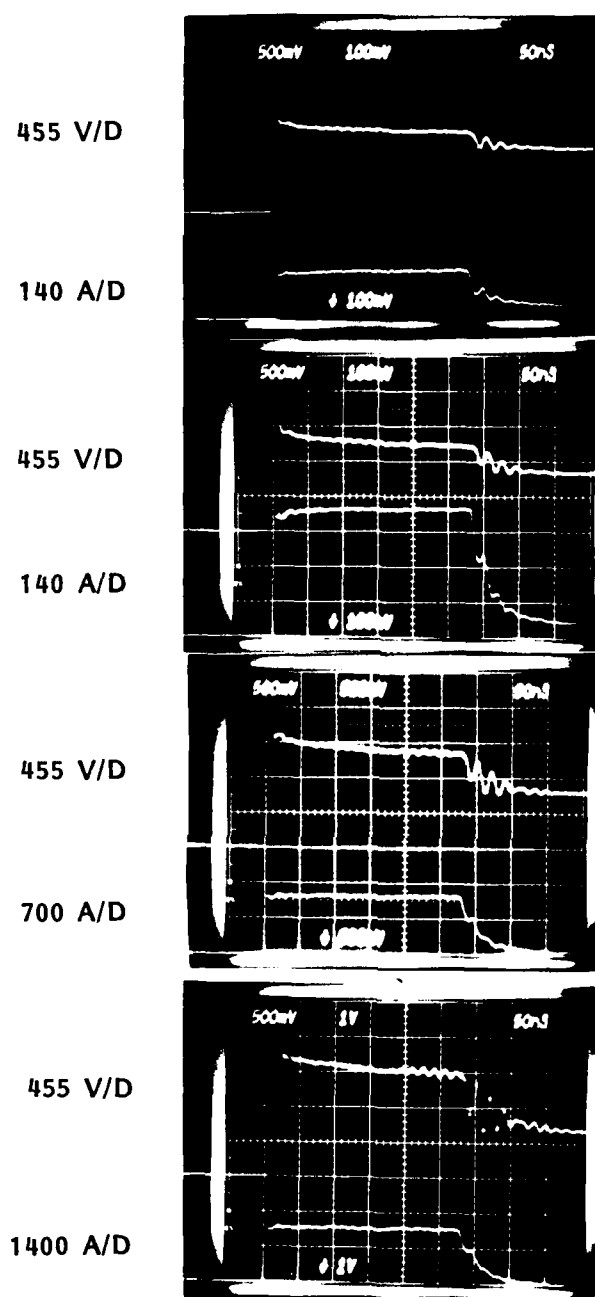


Figure 6. Pulse response characteristics of the X532 GE-MOV^R varistor (2.92 mm thick and 1.14 cm contact diameter - V @ 1 mA DC = 600 volts).

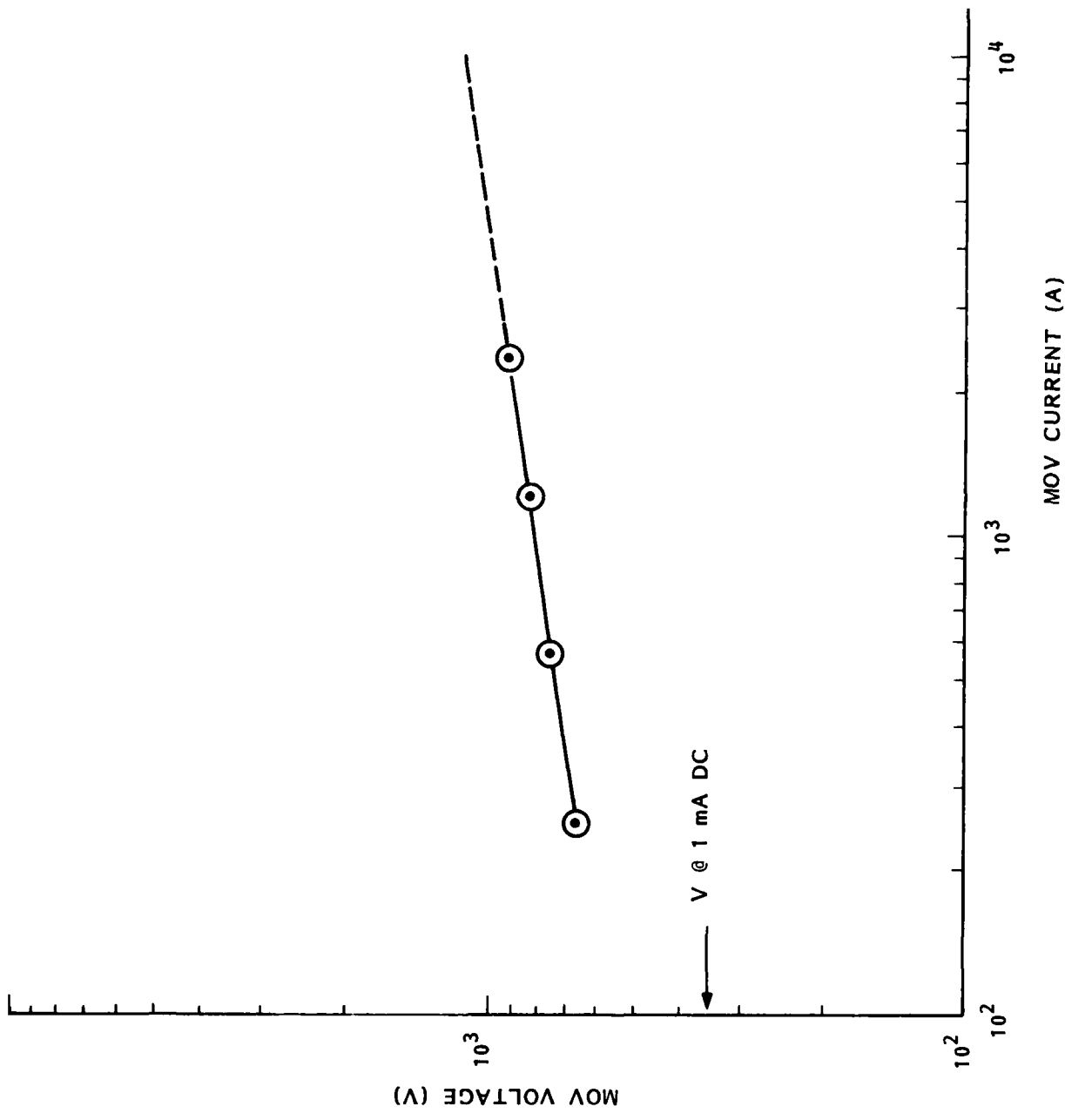


Figure 7. Pulse V-I characteristics of the X531 GE-MOV varistor.

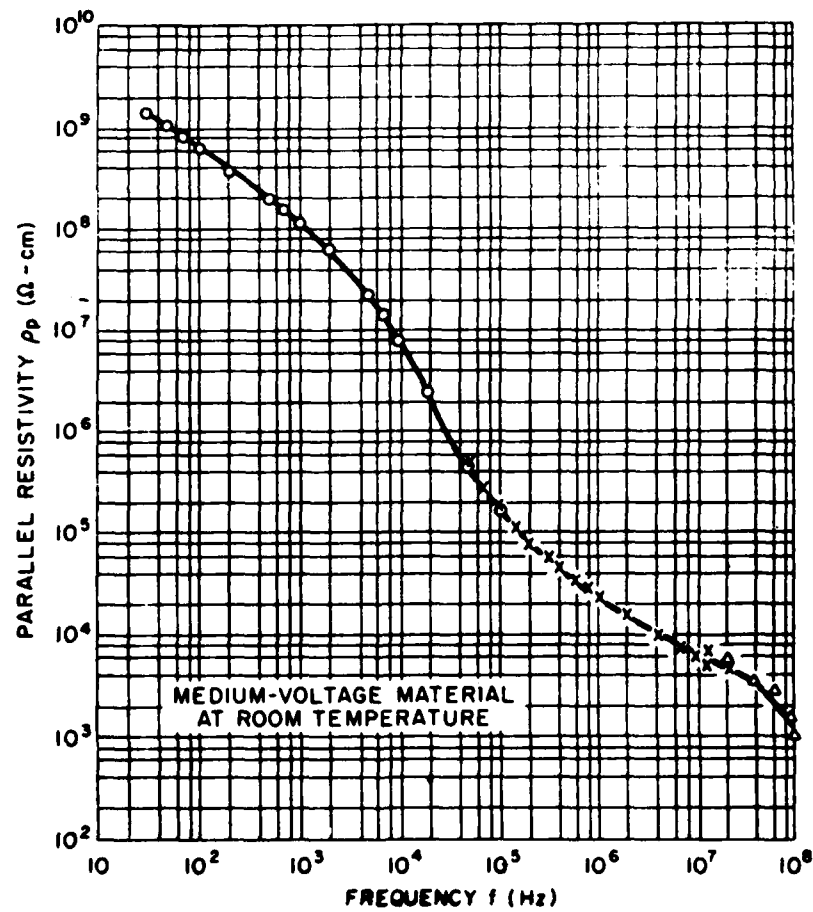
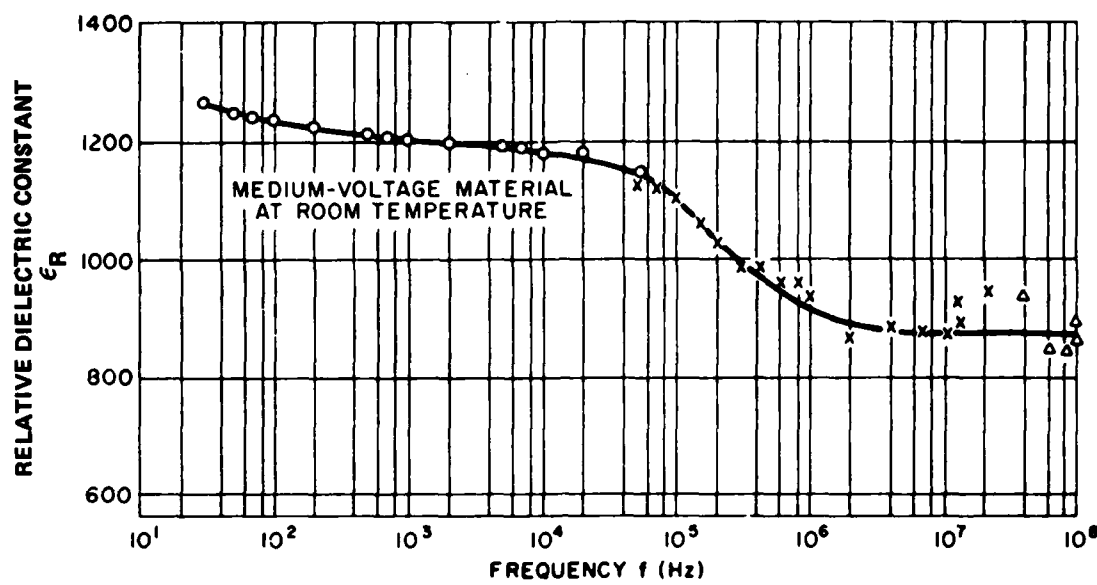


Figure 8. AC dielectric characteristics of type DD medium voltage GE-MOV^R varistors.

conducting zinc oxide grains of approximately 10 microns diameter, whereas typical sizes of the intergranular phase in medium voltage material is estimated at 1000 Angstroms thickness, resulting in an actual value for the dielectric constant of the intergranular phase at about two orders of magnitude less than that shown (Reference 3.3). However, the effective dielectric characteristics such as that given in Figure 8 are those values which, when used with the total material geometry, yield the appropriate value for the material capacitance and loss.

Figure 9 shows the dielectric characteristics of two types of GE-MOV® varistor devices evaluated in the present program - the X531 and X532 devices. The data shown is given in terms of the specific reactance of each device versus frequency "f". Here, for a device of area "A", thickness "T" and capacitive reactance X_C , the specific reactance is given as

$$\frac{X_C A}{T} = \frac{1}{2\pi\epsilon_0 \epsilon_R f} \quad (3.1)$$

The data indicates effective values of ϵ_R in the range of 1 to 10 MHz of 454 for the X531 device and 233 for the X532 device.

3.4 RF LOSS CHARACTERISTICS.

The RF loss characteristics of the GE-MOV® varistor are those losses associated with the device when operated at voltages below the high current conduction region (i.e. standby). These losses arise from three sources: the reactive and resistive losses of the dielectric of the intergranular phase and the resistive loss of the zinc oxide grains. The losses are manifested as insertion losses between a circuit's source and load, and self heating in the varistor material itself.

In the simplest case, neglecting fringing effects, the metal oxide varistor can be considered as a parallel plate capacitor, whose capacitance is proportional to the area-to-thickness ratio and whose loss is proportional to its thickness-to-area ratio. As such, the capacitance and

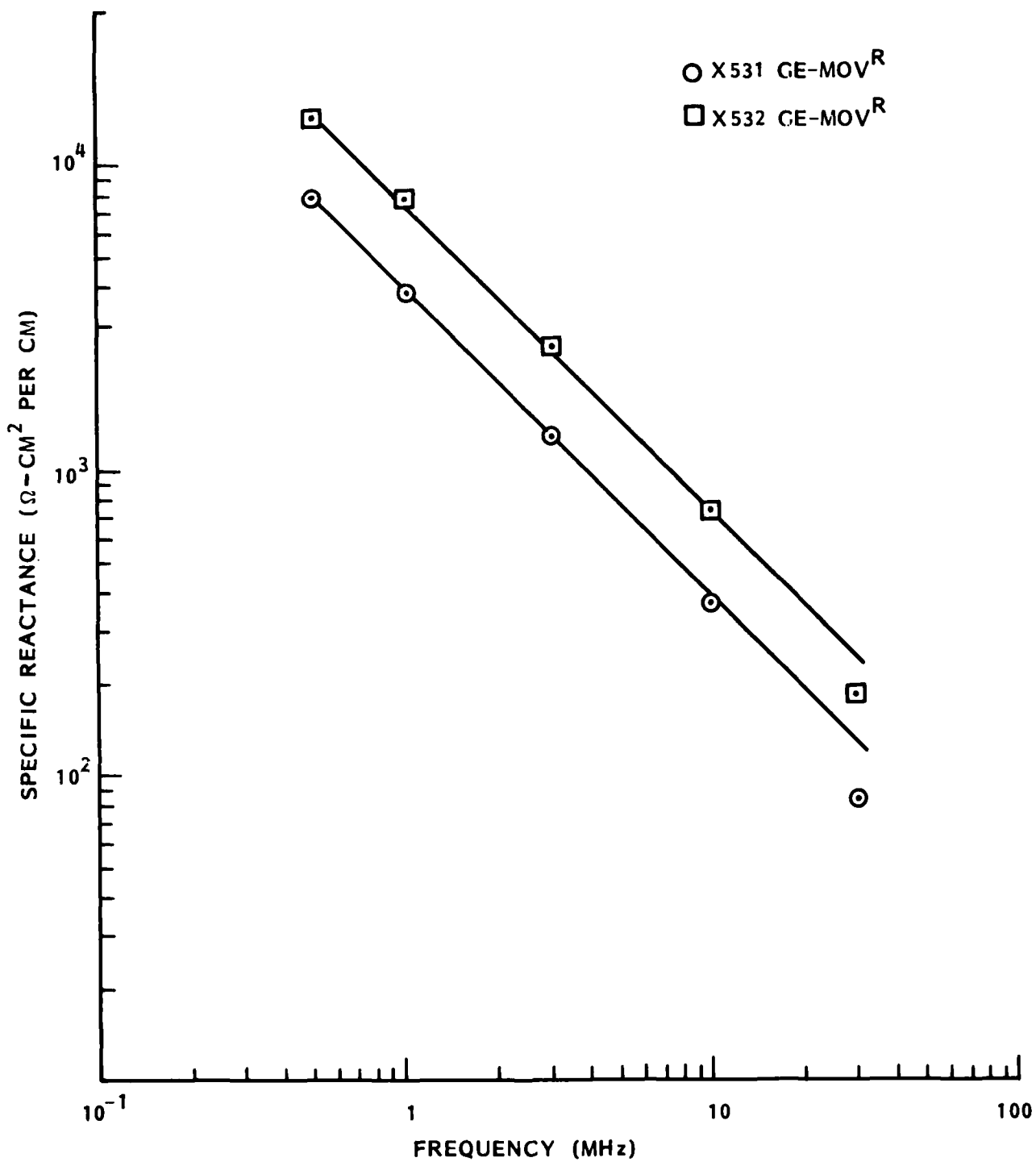


Figure 9. Specific reactance of various medium voltage GE-MOV^R varistors.

resistive loss can be defined in terms of geometry independent quantities, and the loss characteristics for a particular impedance system can be determined. Considering the total equivalent circuit of Figure 3, a simplified equivalent circuit for the RF losses at voltages below high current conduction would be that as shown in Figure 10.

The maximum insertion loss results from applying the varistor material directly across a circuit at a single node without any frequency compensation. Referring to Figure 10, previous studies (Reference 3.2) have shown that

$$X_C \ll R_p \quad (3.2)$$

Hence, varistor insertion loss in a circuit is controlled by reactive losses at low frequencies and grain resistance at the higher frequencies. The losses at these higher frequencies, however, are greatly in excess of those considered acceptable for practical applications (i.e., 1 - 10 db). As such, restricting the analyses to practical applications, we can consider that

$$X_C \gg R_s \quad (3.3)$$

In this case, the equivalent circuit for insertion loss in a Z_0 impedance system is as shown in Figure 11.

Here, insertion loss in db is given by

$$db = 20 \log_{10} \left(\sqrt{\frac{1 + Z_0^2 C^2 \omega^2}{4}} \right) \quad (3.4)$$

or, rearranging

$$\omega C = 2\pi f C = \frac{1}{X_C} = \frac{2}{Z_0} \sqrt{10^{db/10} - 1} \quad (3.5)$$

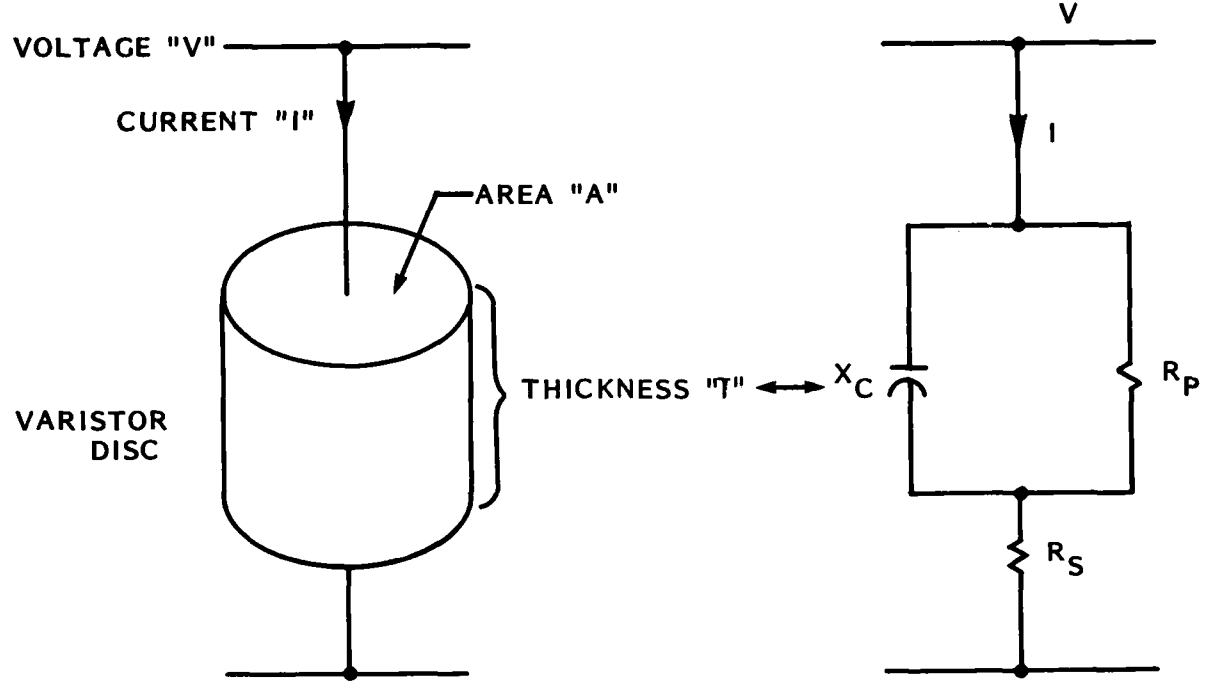


Figure 10. Varistor geometry and equivalent circuit for RF loss analyses.

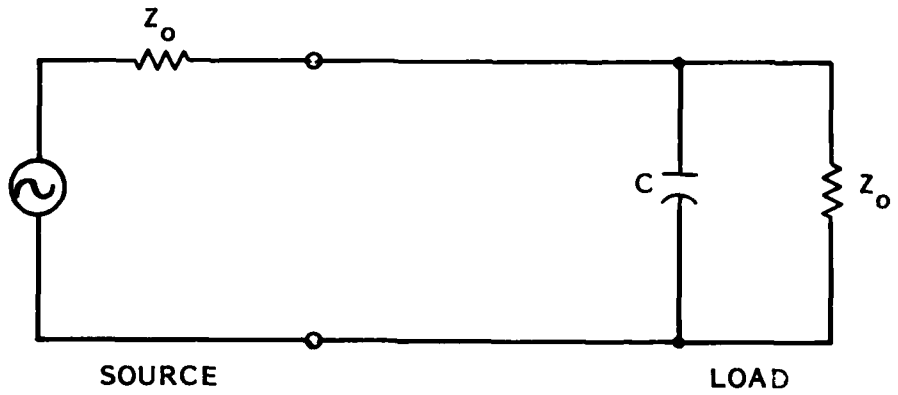


Figure 11. GE-MOV® varistor insertion loss equivalent circuit.

The self heating losses in the varistor material can be found by similar considerations for

$$R_s \ll X_c \ll R_p \quad (3.6)$$

Here

$$IR_s \ll V \quad (3.7)$$

and the power dissipated in the grains (P_s) and the oxide (P_p) is given by

$$P_s = I^2 R_s \quad (3.8)$$

$$P_p = \frac{V^2}{R_p} \quad (3.9)$$

For the disc geometry R_s is given in terms of the grain resistivity " ρ_g " by

$$R_s = \frac{\rho_g T}{A} \quad (3.10)$$

Similarly, R_p is given in terms of the oxide resistivity " ρ_o " by

$$R_p = \frac{\rho_o T}{A} \quad (3.11)$$

Examining Figure 8 yields

$$\rho_o \sim \frac{a}{f} = \frac{10^{11}}{f} \quad (3.12)$$

Considering Figure 10 and Equation 3.6 yields

$$I \sim \frac{V}{X_c} \quad (3.13)$$

For the ideal disc geometry where fringing effects are neglected

$$C = \frac{\epsilon_0 \epsilon_R A}{T} \quad (3.14)$$

Since

$$x_C = -\frac{1}{2\pi f C} \quad (3.15)$$

Equation (3.13) can be written as

$$I \sim \frac{2\pi f \epsilon_0 \epsilon_R A V}{T} \quad (3.16)$$

and, considering equations 3.16 and 3.10, equation 3.8 can be written as

$$P_s = \left(\frac{2\pi f \epsilon_0 \epsilon_R A V}{T} \right)^2 \left(\frac{\rho_g T}{A} \right) \quad (3.17)$$

and, considering equations 3.11 and 3.12, allows equation 3.9 to be written as

$$P_p = \frac{V^2 A f}{10^{11} T} \quad (3.18)$$

Comparing the grain losses to the oxide losses yields

$$\frac{P_s}{P_p} = (2\pi \epsilon_0 \epsilon_R)^2 f \rho_g 10^{11} \quad (3.19)$$

From Sections 3.2 and 3.3 we find that for the X531 device

$$\epsilon_R \sim 450$$

$$\rho_g \sim 0.36 \text{ ohm-cm}$$

and since

$$\epsilon_0 = 9 \times 10^{-14} \text{ farads/cm}$$

and, considering (3.12) to be approximately valid for the X531 device, we can write

$$\frac{P_s}{P_p} \sim 2.4 \times 10^{-9} f \quad (3.20)$$

Equation 3.20 indicates that for frequencies less than about 100 MHz the varistor self heating losses are associated primarily with the oxide rather than the grains. As such, considering (3.9), (3.10), and (3.11) we can express the power per unit volume dissipated within a varistor device of volume "AT" as

$$\text{Peak Power Per Unit Volume} = \frac{V^2 f}{T^2 a} \quad (3.21)$$

and

$$\text{RMS Power Per Unit Volume} = \frac{V^2 f}{2T^2 a} \quad (3.22)$$

For a surge arrester application where the varistor is placed across an RF port of a Z_0 impedance system operating at an RMS power level of P_o , then (3.22) can be expressed as

$$\text{RMS Power Per Unit Volume} = \frac{P_o Z_0 f}{2T^2 a} \quad (3.23)$$

Since the RMS power dissipated per unit volume is related to the maximum power level capability of the varistor device from thermal considerations, equation 3.23 can be considered to be proportionately related to its maximum RF application capability. Here, for example, equation 3.23 shows that the maximum RF transmitter power that a particular varistor device can be used to protect will decrease linearly with frequency.

Since metal oxide varistors have not generally been used in RF applications, the specific power-frequency limitations of the materials were not available. In view of this, the present program was required to perform extensive unique characterizations of the candidate devices considered for use in the HESA prototype. These studies, though, were limited to application oriented studies where specific GE MOV® devices were placed across the output of a 50 ohm transmitter which was driving a 50 ohm power load. At any one particular frequency, the RF transmitter power level was slowly increased until device failure occurred. A new device was then selected, the frequency changed and the procedure repeated again. Experiments were performed on both X531 and X532 unencapsulated devices operated in ambient conditions as well as under ice water immersion.

The essential result of these experiments are shown in Figures 12 and 13. The linear decrease in RF standby power capability with frequency can readily be seen for both varistor devices. Heat sinking, via an ice water bath, was only found to provide a factor of 3 increase in power handling capability for the unencapsulated devices. At first glance the X532 device (210 volts per mm) appears to be about a factor of 3 better than the X531 device (140 volts per mm). However, since the X532 device has a higher volts-per-thickness rating it would have to be 1.5 times thinner than an X531 device to be used for the same voltage rating application. Here, though, equation 3.23 indicates that the RF power capability would then be decreased by a factor of 2.25 for this thinner X532 device, thus only providing about a factor of 1.3 higher RF power capability compared to the X531 device.

3.5 RF SELF HEATING LOSS REDUCTION METHODS.

The data presented in Figures 12 and 13 indicate that the varistor can not be indiscriminately used in high power, high frequency applications without regard for the RF self heating effects. Since the present application called for devices on the order of the thickness size of the X531 and X532 to be used to protect Kilowatt transmitters operating up to 100 MHz, techniques had to be developed to reduce the varistor losses. A somewhat ingenious approach was developed to utilize the varistor for these severe applications. This approach utilizes a configuration of back-to-back strings of a diode in series with the varistor, as shown

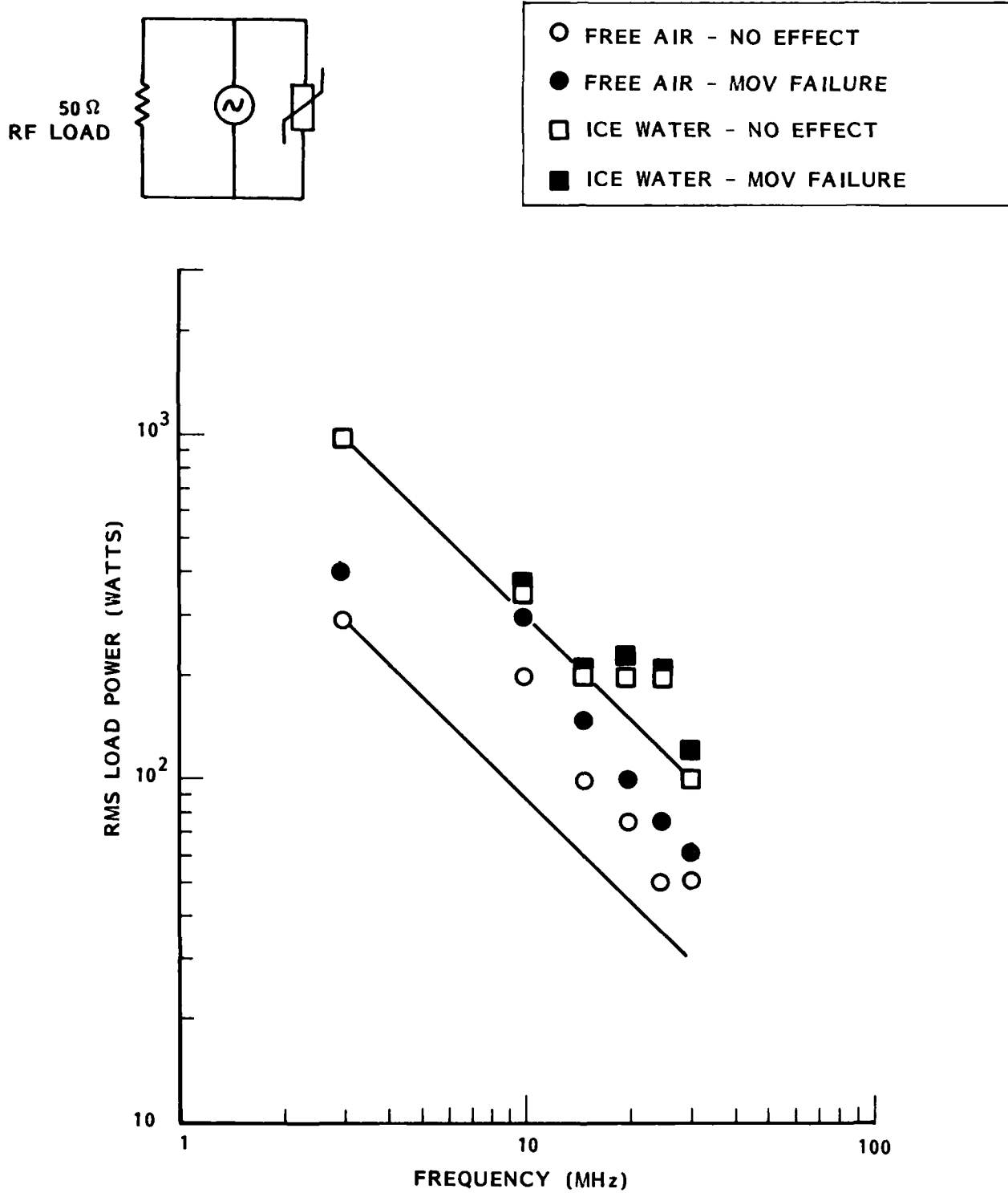


Figure 12. Maximum RF standby power capability of X531 GE-MOV(R) varistors.

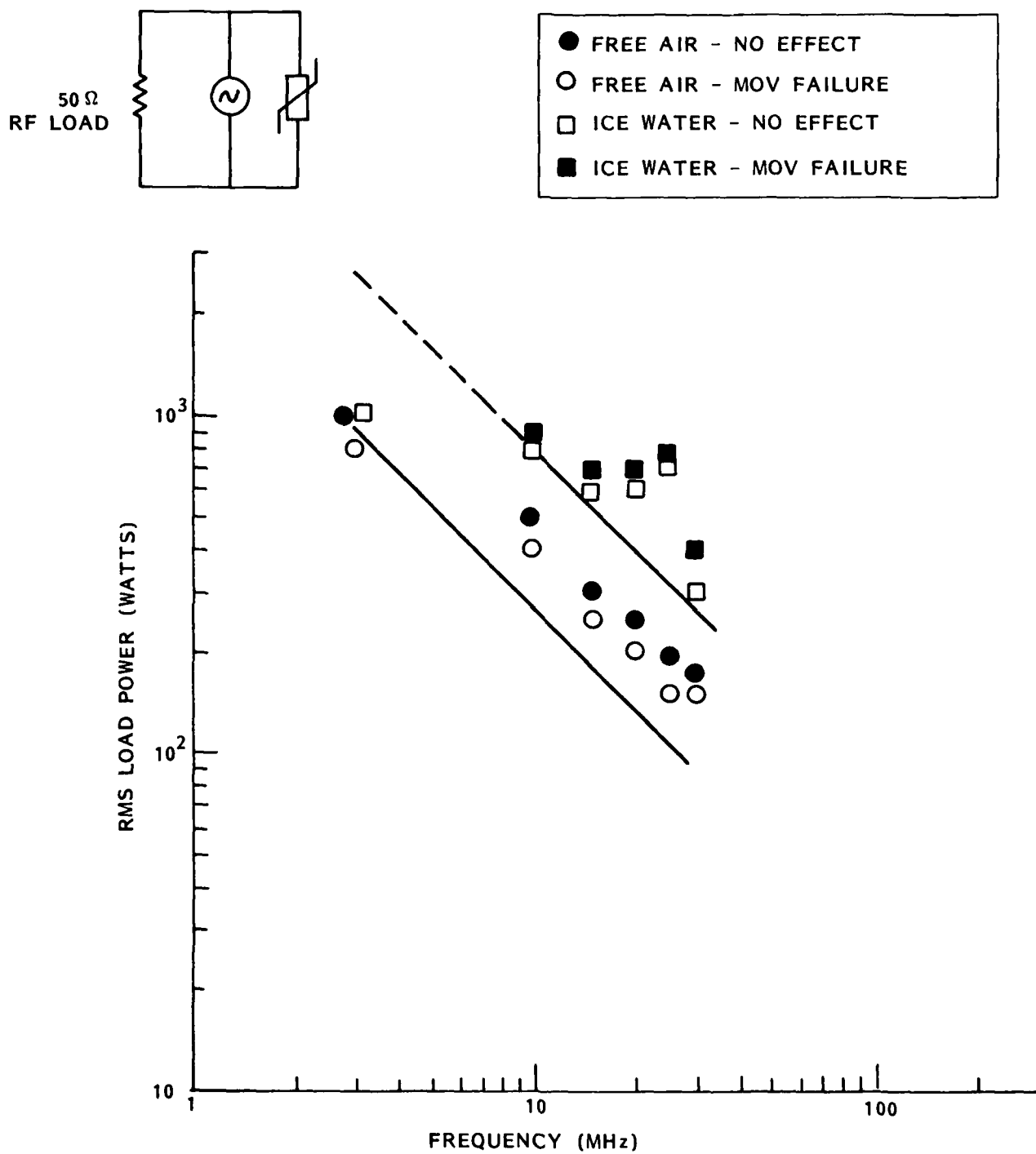


Figure 13. Maximum RF standby power capability of X532 GE-MOV^R varistors.

schematically in Figure 14 and equivalently in Figure 15. Referring to Figure 15, the concept is based on using the diode to incrementally charge up the varistor capacitance on each half cycle and shut off on the opposite half cycle, thus preventing varistor discharge. The current through the varistor progressively decreases with time until steady state is reached, at which time the current through the varistor is a constant, low level "trickle charge" determined by the diode capacitance. The critical diode parameters required for this application are as follows:

- 1) $X_D \gg X_M$ and $X_D \gg R_m$: This insures that the steady state varistor current will be much less than that when the varistor is connected directly across the RF source. Note that this also allows the use of an extremely large area varistor since now varistor current is not controlled by varistor geometry.
- 2) $V_R > 2 V_p$: At steady state the reverse voltage applied across the junction during the opposite half cycle is the voltage across the charged varistor capacitance " V_p " plus the peak line voltage, also of value " V_p ".
- 3) $V_F \ll V_M$: The whole advantage of the varistor is that, unlike many diodes, it can sink large transient currents while clamping at large voltages. For the transient energy dissipated in the diode to be small, then the diode voltage drop should be much smaller than the varistor voltage drop at the same common current level. Obviously, the diode must be capable of passing the forward pulse current for the time duration required.
- 4) $t_R < T_p/2$: This insures that the diode will shut off during the opposite half cycle and prevent significant discharging of the varistor capacitance.
- 5) $V_m > V_p$: This is required to prevent the fully charged varistor capacitance from turning on the varistor in a "quasi-steady state" mode.

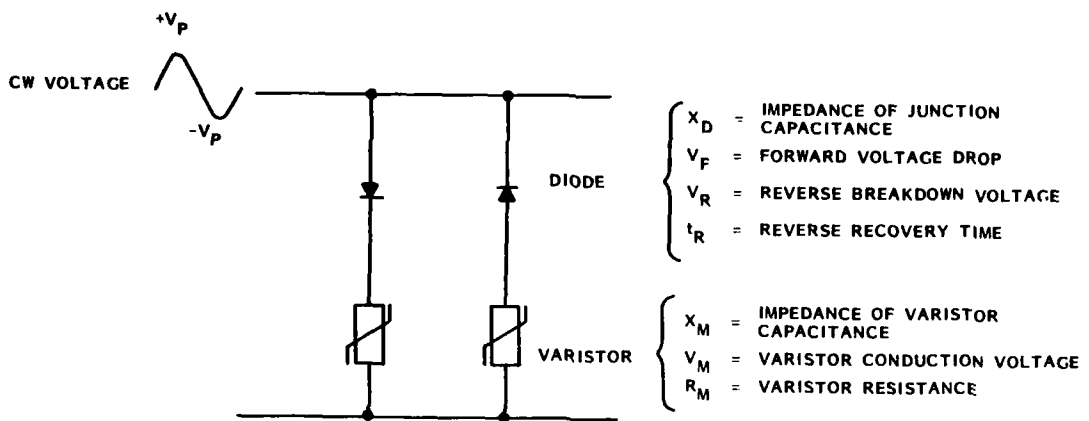


Figure 14. "RF Self Heating" loss reduction technique for high power, high frequency varistor applications.

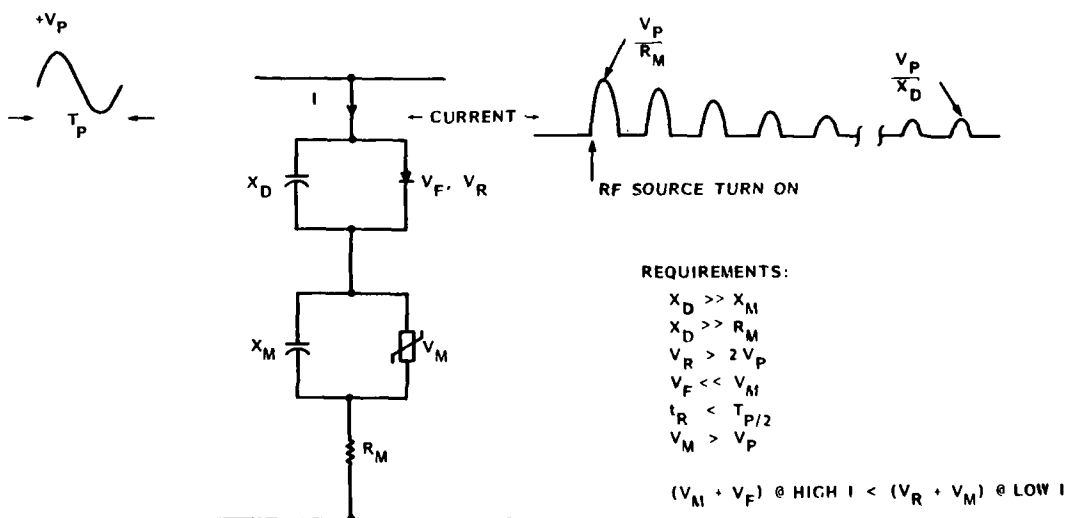


Figure 15. Equivalent circuit for the varistor "RF Self Heating" loss reduction technique.

- 6) $(V_M + V_F)$ at High I < $(V_R + V_M)$ at Low I: Since diodes are much more sensitive to pulse burnout in the reverse direction than in the forward direction, this requirement insures that the non-conducting string will not be turned on in the "reverse" direction due to high pulse currents in the conducting string, thus burning out the diode in the non-conducting string.

The above requirements represent a non-trivial set of diode parameter requirements to be met by a real device. Since the objective of the present program was to demonstrate proof-of-concept the optimization of diode selection, as well as varistor selection, was beyond the scope of the program. However, an extensive evaluation of commercially available diodes revealed that Unitrode makes a series of high efficiency, high current diodes which were a more than adequate, cost effective demonstration approach for the present program objectives. The only drawback was that the devices have a 30 ns reverse recovery time which would affect their utility, to some degree, for 100 MHz applications. Here, the most desirable device from this series would be the 1N5816. This device, however, is only available in standard form in a stud mounted package. Since this configuration would be unacceptable from a package inductance standpoint, and since procuring the device in chip form and repackaging in a custom carrier was well beyond program scope, the next highest rated series device in axial lead configuration, the 1N5811, was chosen for use.

The 1N5811 device has a peak inverse voltage of 150 volts and has a forward pulse current rating of 5000 amps at 100 ns with a pulse width dependency of $t^{-1/3}$. Our experiments showed that these devices have a reverse polarity burnout level of about 200 amps at 300 ns and can safely pass 2270 amps at 300 ns in the forward direction. The forward V-I characteristics of the device which were obtained through these tests are shown in Figure 16. Notice that the diodes exhibited a voltage drop of less than 12 volts at a forward current of 2250 amps. The data in Figure 17 shows the relatively low capacitance of the diodes over the frequency range of interest. Finally, the proof of approach is demonstrated by the data shown in Table 1. Here various series/parallel combinations of 1N5811 diodes and GE-MOV® varistors were placed across the same high power, RF transmitter configuration used to obtain the data of Figures 12 and 13 in order to determine the increased capability of our design

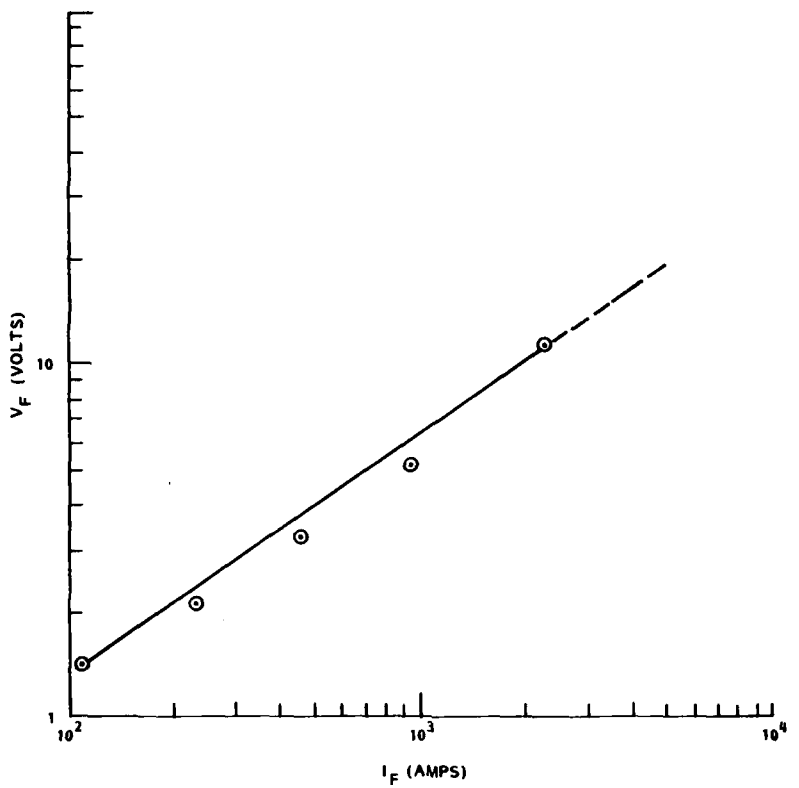


Figure 16. Pulse forward V-I characteristics of the Unitrode 1N5811 diode.

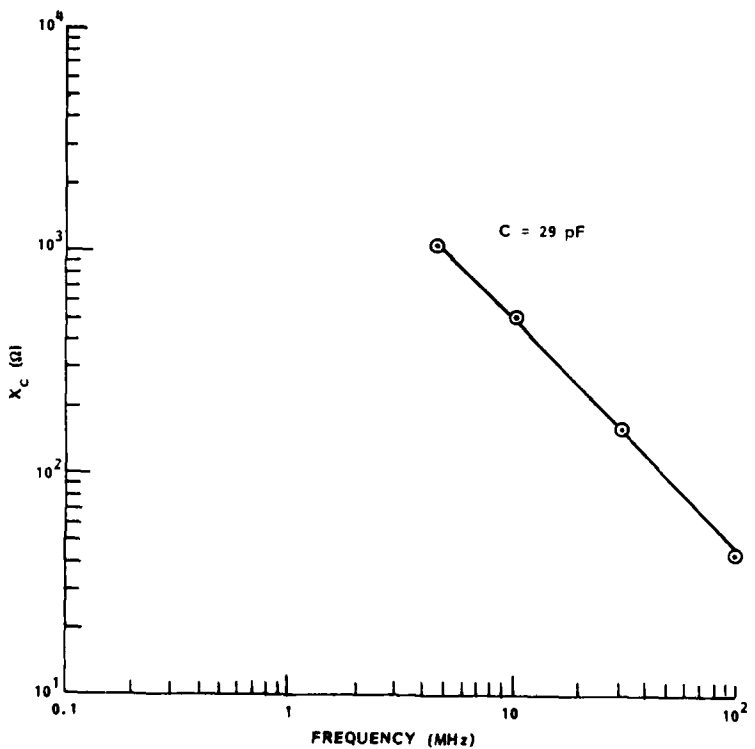


Figure 17. Capacitive reactance of the Unitrode 1N5811 diode.

approach at ambient conditions. A minimum of 4 diodes in series were needed to meet the $V_R > 2 V_p$ requirement. Note that now at 30 MHz greater than 1KW applications are possible, where before only 30 watts was achievable for the X531 device. The effects of the 30 ns reverse recovery time on limiting transmitter power applications at 100 MHz can also be readily seen from the data.

Table 1. Maximum RF standby power capability of Unitrode IN5811 diodes combined with GE-MOV® varistors.

GE-MOV® TYPE	1N5811 UNITRODE		SAFE CW LEVEL	
	# IN SERIES	# IN PARALLEL	FREQ (MHz)	RMS P LOAD POWER LEVEL
X531	4	1	4.5	>1 KW
			10	>1 KW
			30	>1 KW
	4	2	100	>625 W
			4.5	>1 KW
			10	>1 KW
	6	1	30	>1 KW
			100*	>625 W & <1 KW
			30	>1 KW
			100*	<1 KW
X532	4	2	100*	>600 & <1 KW

*DIODE SOLDER CONNECTION AT MID STRING MELTS

3.6 HIGH ENERGY ABSORPTION CAPABILITY.

A critical parameter of a protection device is its ability to absorb, or bypass, the unwanted transient energy without suffering significant degradation or damage. The bulk properties of the material provide an inherent high energy absorbing capability, because energy dissipation is evenly distributed throughout the bulk. Also, the GE-MOV® varistor does not exhibit a catastrophic failure threshold as does, say a semiconductor device due to junction burnout. Instead, the varistor will experience a gradual degradation in its low current conduction characteristics for increasing levels of input energy pulses whose deposited energy is sufficient to cause a significant temperature rise in the varistor material.

Published varistor specifications include the "pulse ratings," a family of curves that define, for each varistor type, the number of isolated pulses that a varistor can absorb until its "rating" is reached. The curves show lines relating amplitude, duration, and total number of pulses. Figure 18 shows the family of curves applicable for a typical medium voltage GE-MOV® varistor material (Reference 3.4). It should be noted that the pulse rating does not mean catastrophic failure of the varistor at the end of this rating, but only a 10% change in the varistor nominal voltage. Although some change is indicated, the varistor is quite capable of staying on line voltage and of clamping surges.

A careful examination of the pulse rating curves will show that the duration of the pulses has a strong influence on the number of permissible pulses. Furthermore, the relationship between the increased duration of the pulses and the decreased number of permissible pulses is not proportional. For instance, consider pulses of about 30 ampere/cm² and 100 μ sec duration. The curves show about 3000 pulses allowed. Now increase the duration of the pulses to 1000 μ sec (a ten-fold increase), while keeping the amplitude the same: The curves show the permissible number as one pulse only. Thus, the ten-fold increase in duration does not result in a ten-fold decrease in the number of permissible pulses; the reduction in that number is much greater than the inverse of the increase in duration.

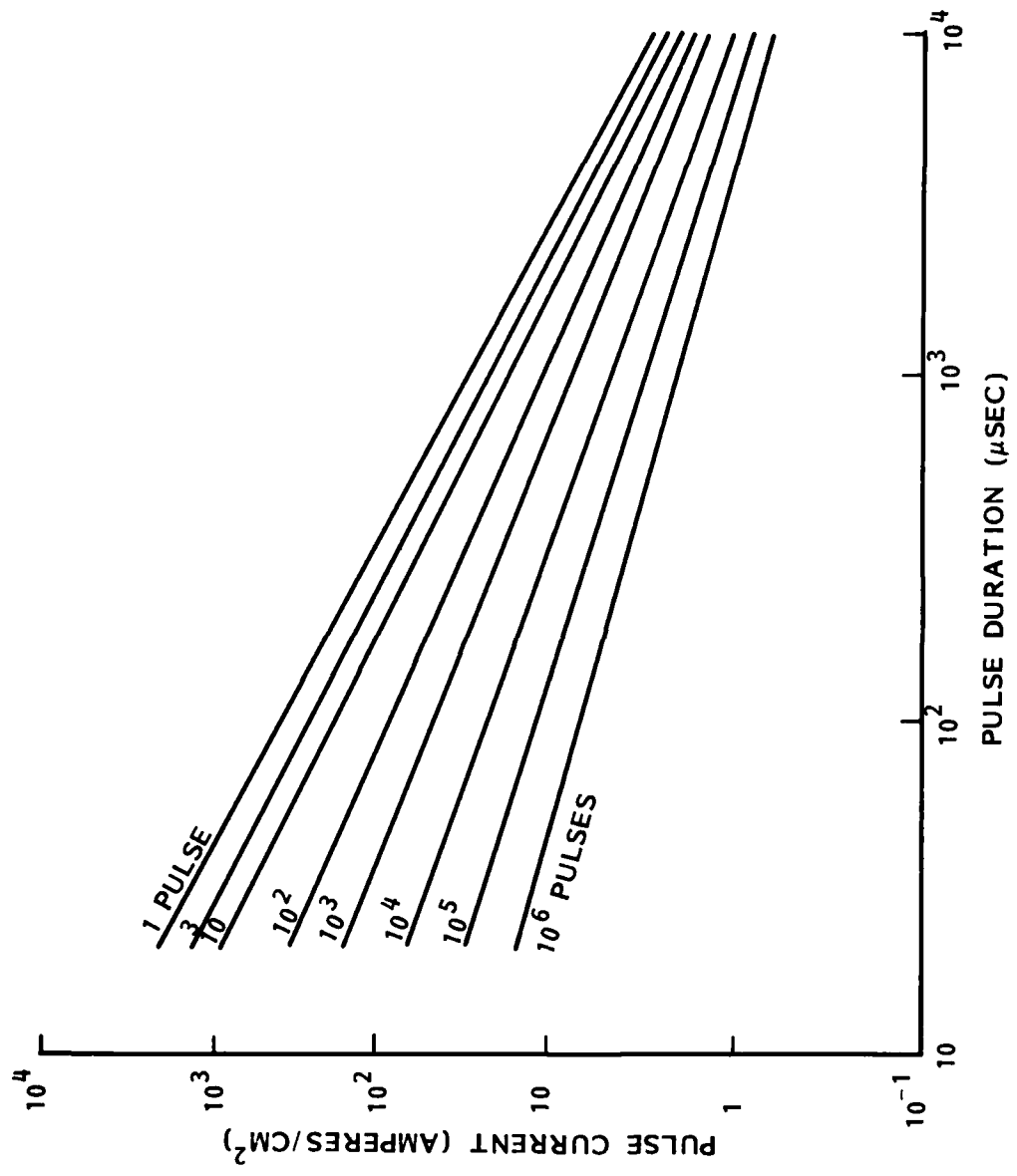


Figure 18. Pulse ratings of typical medium voltage GE-MOV® varistors.

SECTION 4

SATURABLE MAGNETICS ELEMENT

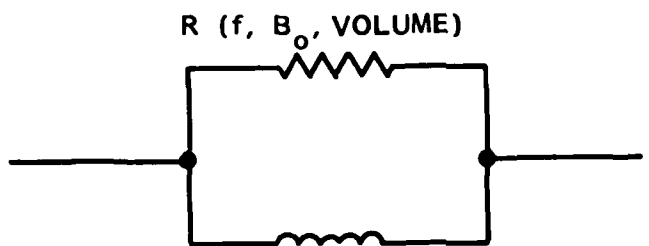
4.1 AC EQUIVALENT CIRCUIT.

A simplified equivalent circuit which qualitatively describes the generic AC operation of a saturable magnetic device is shown in Figure 19. The circuit consists of the parallel combination of an inductor and a resistor. Below saturation the inductance is controlled by a frequency dependent permeability " μ unsaturated." Once saturation is reached the permeability " μ saturated" becomes unity. The electrical excitation required to cause saturation is quantified in terms of a volt-second product "(Vt)sat" which is dependent on the number of turns "N", the material cross sectional area " A_c " and the saturation flux density " B_{sat} " of the material. The wire resistance of the inductor has been neglected for the present discussion. The resistance shown, which is representative of material losses, is dependent on frequency "f", operating flux density " B_0 ," and material volume. The characteristics of each of these elements is discussed in detail in the following subsections. These discussions are also augmented by extensive experimental data which was obtained under this program on a variety of ferrite core materials which were supplied to us through the courtesy of Magnetics Incorporated (MI) and Ceramic Magnetics Incorporated (CMI). The various ferrite toroidal geometrical configurations which were examined here are listed in Table 2.

4.2 SWITCHING CHARACTERISTICS.

Consider "N" turns on a toroidal core of magnetic material which is shown in Figure 20. The operating flux density " B_0 " and unsaturated inductance " L_u " is given by Kraus (Reference 4.1) in MKS units as

$$B_0 = \frac{10^4 \mu_0 \mu_R N I}{l_c} \quad (4.1)$$



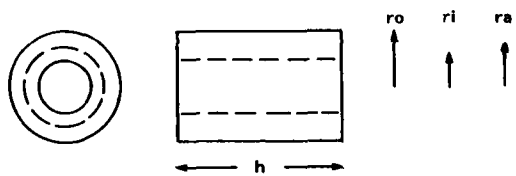
μ UNSATURATED (f)

μ SATURATED = 1

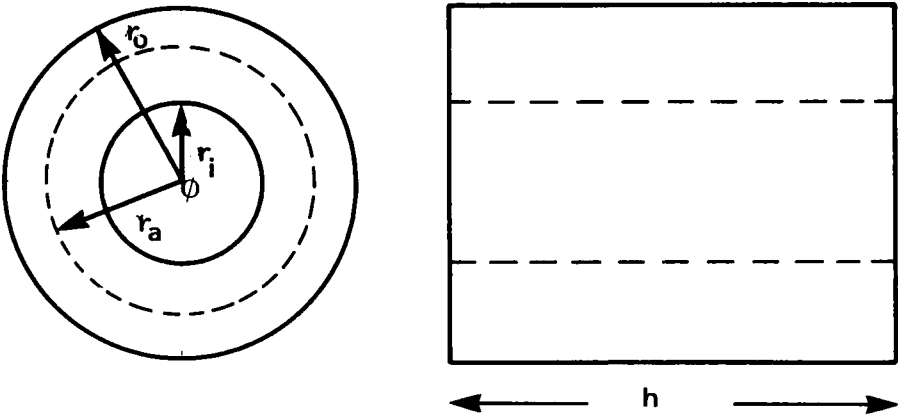
SATURATION VOLT - SECONDS $\propto N, B_{SAT}, A_C$

Figure 19. Simplified AC equivalent circuit of a saturable magnetic device.

Table 2. Ferrite toroidal cores evaluated for basic device response characterizations.



MATERIAL			ro CM	ri CM	ra CM	h CM	Ic CM	Ac CM ²	Vc CM ³
MFG.	TYPE	PART #							
MI	F	41306	0.635	0.397	0.516	0.635	3.124	0.149	0.465
MI	F	42206	1.11	0.686	0.898	0.635	5.419	0.261	1.414
MI	F	43813	1.91	0.953	1.43	1.27	8.30	1.11	9.213
CMI	CMD5005	-	1.27	0.635	0.953	0.762	5.99	0.484	2.896
CMI	CN20	T8550	1.10	0.686	0.893	1.27	5.61	0.525	2.95
CMI	MN60	-	1.40	0.635	1.02	0.686	6.39	0.525	3.36
CMI	MN80	T8525	1.1	0.635	0.893	0.635	5.61	0.263	1.48
CMI	CMD5005	84-17-3	1.99	0.984	1.49	1.199	9.36	1.206	11.26



- r_o = OUTER RADIUS, (METERS)
 r_i = INNER RADIUS, (METERS)
 r_a = AVERAGE RADIUS = $(r_o + r_i)/2$ (METERS)
 VOL = VOLUME = $\pi h (r_o^2 - r_i^2)$, METERS
 SA = SURFACE AREA = $2\pi r_o h + 2\pi r_i h + 2\pi (r_o^2 - r_i^2)$, (METERS²)
 A_c = CORE AREA = $(r_o - r_i) h$, (METERS)
 l_c = AVERAGE CORE PATH LENGTH = $2\pi r_a$, (METERS)
 B_o = OPERATING FLUX DENSITY, (GAUSS)
 B_{sat} = SATURATION FLUX DENSITY, (GAUSS)
 μ_o = $4\pi \times 10^{-7}$, HENRIES/METER
 μ_r = FUNCTION OF FREQUENCY
 N = NUMBER OF TURNS
 V = OPERATING VOLTAGE, (VOLTS)
 f = OPERATING FREQUENCY, (HERTZ)
 I = OPERATING CURRENT, (PEAK AMPERES)
 t_{sat} = TIME TO SATURATE, (SECONDS)
 L_u = UNSATURATED INDUCTANCE, (HENRIES)
 L_s = SATURATED INDUCTANCE, (HENRIES)
 V_{avg} = AVERAGE VOLTAGE OF WAVESHAPE, (VOLTS)
 P_V = CORE LOSS PER UNIT VOLUME (WATTS)
 L_c = MINIMUM INDUCTANCE TO MEET INSERTION LOSS SPEC

Figure 20. Toroidal core of magnetic material.

and

$$L_u = \frac{\mu_0 \mu R N^2 A_c}{l_c} \quad (4.2)$$

Considering (4.2), then (4.1) can be rearranged and rewritten as

$$IL_u = 10^{-4} N A_c B_0 \quad (4.3)$$

Consider now the case of a constant voltage "V" being switched across a fixed inductor "L". The current "I" as a function of time "t" is found from

$$V = L \frac{dI}{dt} \quad (4.4)$$

Since "V" is a constant value

$$Vt = IL \quad (4.5)$$

and (4.3) can be written as

$$Vt = 10^{-4} N A_c B_0 \quad (4.6)$$

Equation 4.6 shows that as time increases the operating flux density in the core increases, and core saturation is reached when "B₀" reaches a value "B_{sat}". Hence, the volt-second value required to produce saturation is given by

$$(Vt)_{sat} = 10^{-4} N A_c B_{sat} \quad (4.7)$$

Equation 4.7 is the basic device equation which determines at which point the magnetic material will change state. However, in order for a magnetic material to be useful as a practical device for surge arrester applications it must exhibit a number of required switching features. First, it must be capable of changing states extremely fast and such characteristics must be repeatable (the later implies a low residual magnetism). Secondly, device recovery must be equally as fast in order

to negate a latchup condition caused by circuit operating voltages. Finally, the device must be capable of passing high charge levels without causing permanent changes in the basic material properties. These switching features were evaluated for low residual magnetism ferrites supplied by MI and high residual magnetism ferrites supplied by CMI.

Figure 21 shows the switching characteristics observed when using 6 turns on an MI low residual magnetism F43813 toroid. The threshold onset of saturation and device switching can be seen (i.e., $V = 2$ KV) as well as the " $(V_t)_{sat} = \text{constant}$ " characteristics as device voltage is increased. Multiple shots were taken at each device voltage level to demonstrate repeatability which, in turn, demonstrates low residual magnetism. The extremely fast switching characteristics of the device are readily observed here. Figure 22 demonstrates the fast saturation recovery characteristics observed in the same toroid. Here, a 50 ohm transmission line was charged up and subsequently discharged across a 10 ohm resistor to produce a high power, bi-polar square wave drive across the device. The turns were reduced to 4 in order to keep the required pulser charge voltage to produce saturation to within the voltage capabilities of the pulser. In all cases device saturation (increased current and decreased voltage), subsequent rapid recovery (decreased current and increased voltage) and then resaturation in the opposite polarity produced by the bi-polar pulse are observed.

The switching characteristics of the saturable magnetic device are also dependent on circuit parameters as well as magnetic material properties. Here, once the device is switched into saturation the subsequent increase of current through the device with time is controlled by the " L_s/R " time constant of the "saturated inductor - circuit resistor" network. These characteristics can be seen from the data shown in Figure 23. Here, the toroid shown in Figure 21 was driven into saturation at a fixed " V_t " level and the circuit resistance " R " varied. The increased time to reach the final voltage and current values as " R " decreases can readily be observed.

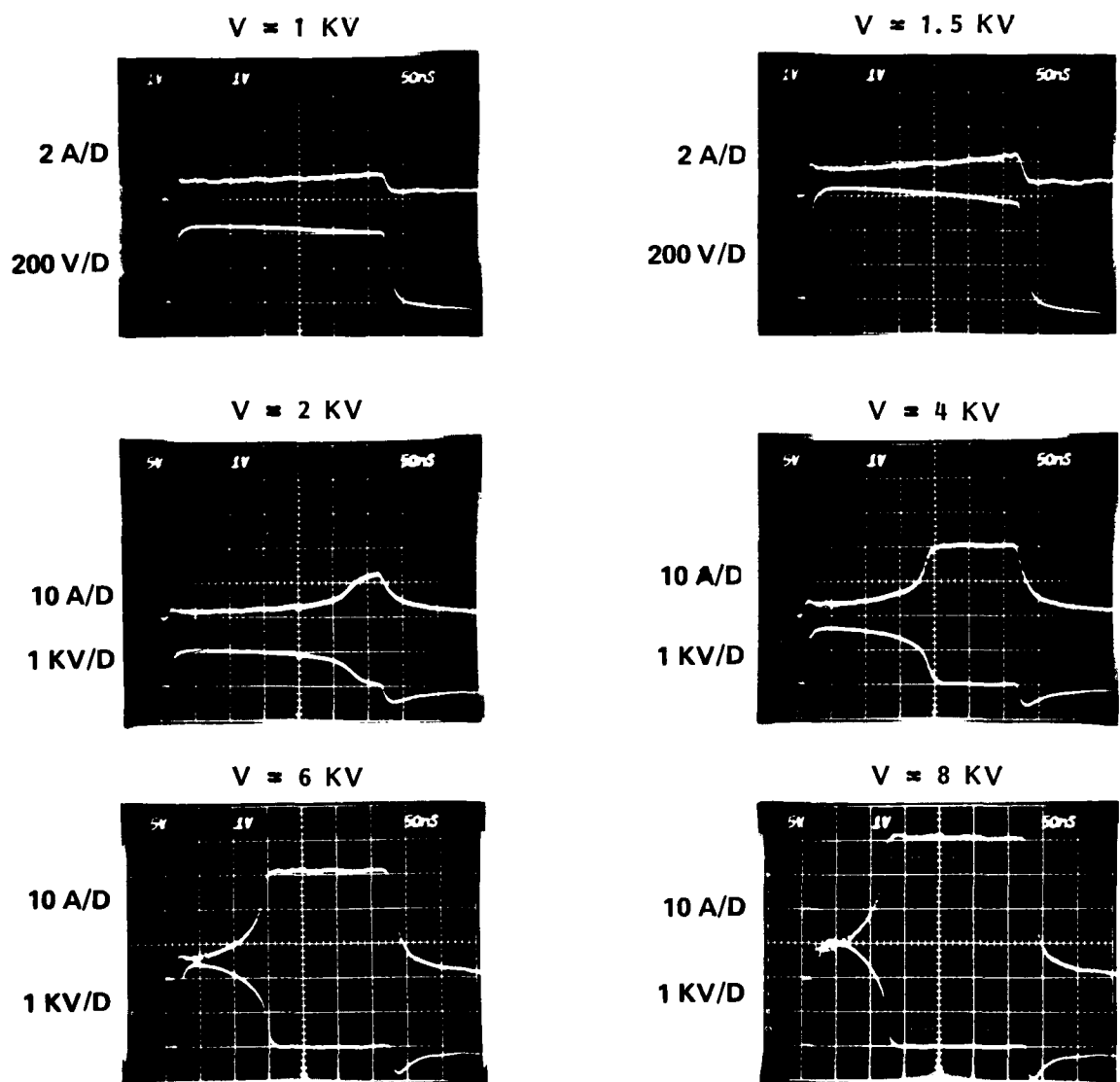
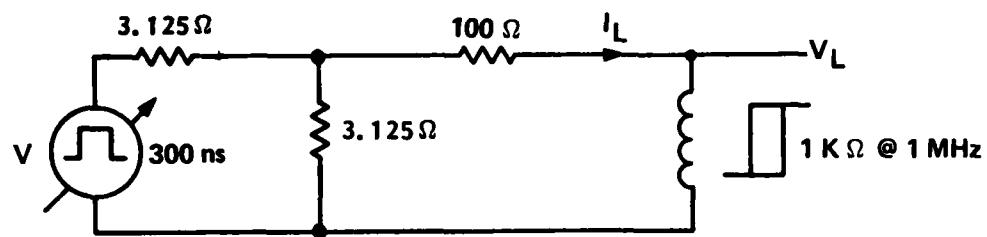


Figure 21. Device switching characteristics - 6 turns on a Magnetics Incorporated F43813 toroid.

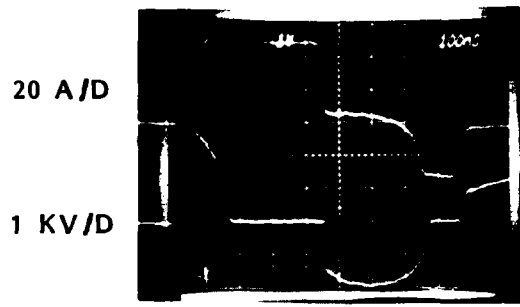
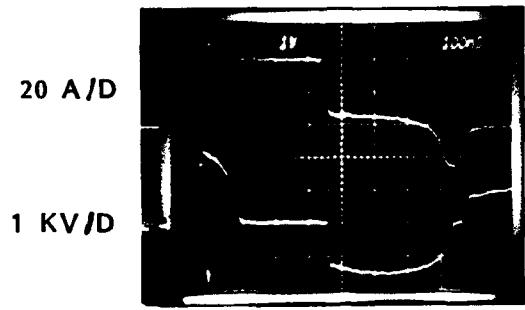
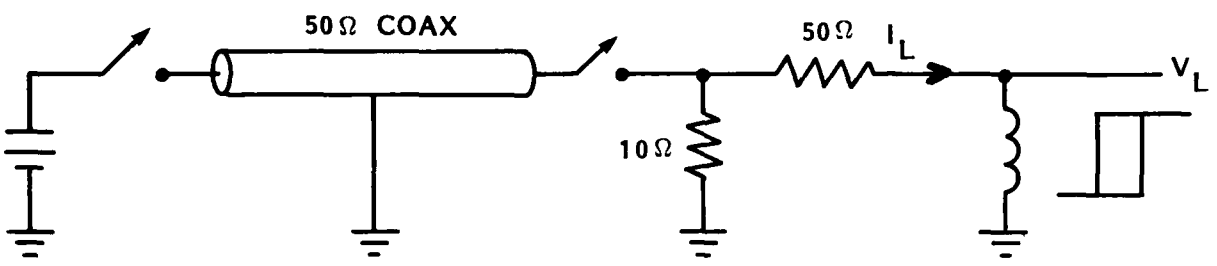


Figure 22. Device saturation recovery characteristics - 4 turns on a Magnetics Incorporated F43813 toroid.

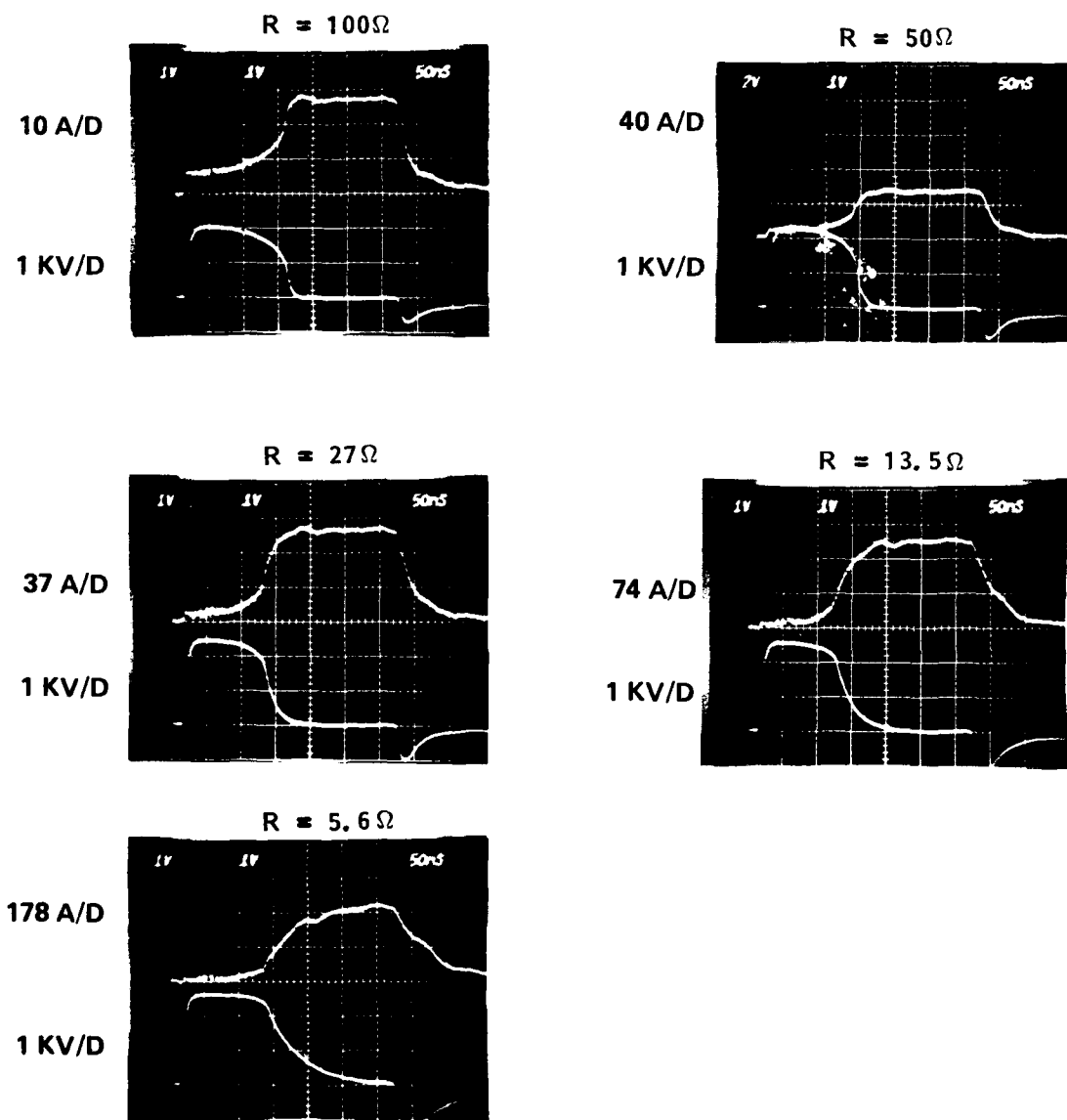
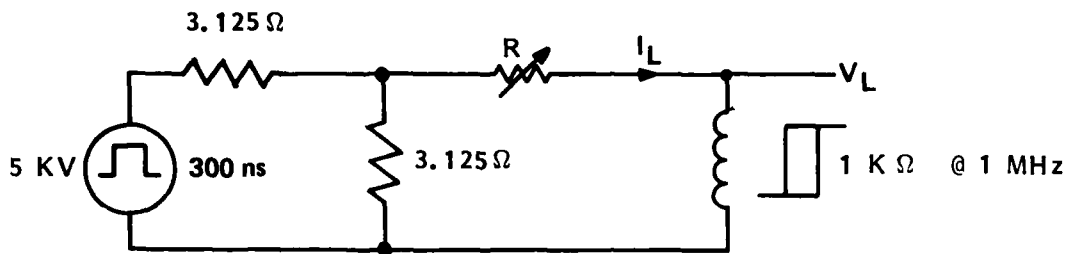


Figure 23. Device saturation charge characteristics - 6 turns on a Magnetics Incorporated F43813 toroid.

The final concern is that associated with the effects on device characteristics of high "It" levels through the saturated inductor. Figure 24 shows the data obtained on the 6 turn F43813 toroid using high "It" drives through the saturated device. Although the saturation charge was limited to 0.07 coulombs, repeated exposures produced no detectable changes in device characteristics.

The same F43813 toroid was subsequently cut to form two half toroids and then reassembled in toroid form with a 10 mil RTV gap. The device characterization was then repeated. Aside from the lower unsaturated inductance caused by the lower "effective μ " of the gapped toroid the device response, as shown in Figures 25 through 28, was characteristically the same, thus demonstrating the fact that gaps do not alter the switching capability of the magnetic devices.

Another interesting variation, that of coaxial arrangements, was investigated using MI low residual magnetism F42206 cores. Here a solid rod was inserted through 10 toroids and evaluated for switching characteristics (note that this configuration is in reality one turn on 10 toroids and corresponds to 10 turns on 1 toroid for switching considerations). Figure 29 shows that, as expected, the coaxial arrangement also provides a useful switching device.

The switching characteristics associated with high residual magnetism materials was investigated using CMI's CMD 5005 and CN20 toroids. The data shown in Figures 30 and 31 illustrate these characteristics. In both cases the pulser voltage was incrementally increased in value until the devices were just taken slightly into saturation (first photo). After this, the pulser was then kept at the same value for three shots. The decrease in "Vt" product to cause saturation due to the residual magnetization produced in the toroids after the first pulse (i.e., $[B_{sat} - Residual Magnetization] < [B_{sat} - 0]$) can be seen. The pulser polarity was then reversed while still keeping the same level. The first opposite polarity pulse demagnetizes the toroids and the characteristics revert back to that observed on virgin units. Subsequent pulsing, however, reestablishes a residual magnetism and the whole process starts over again.

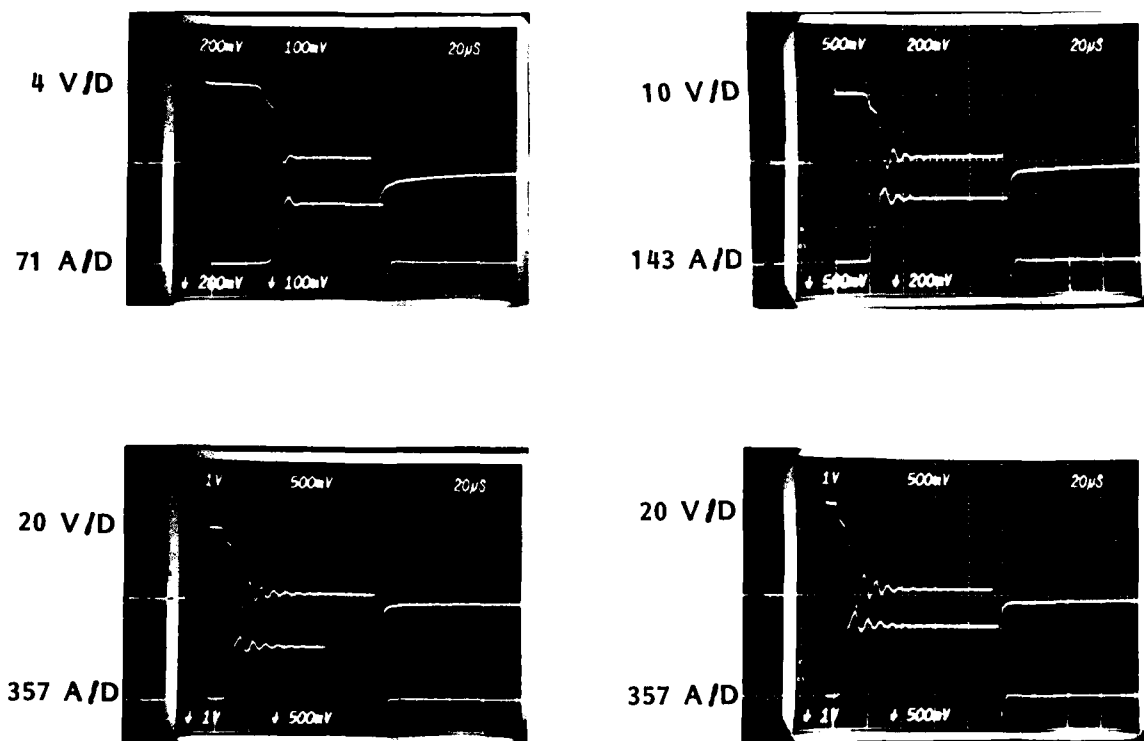
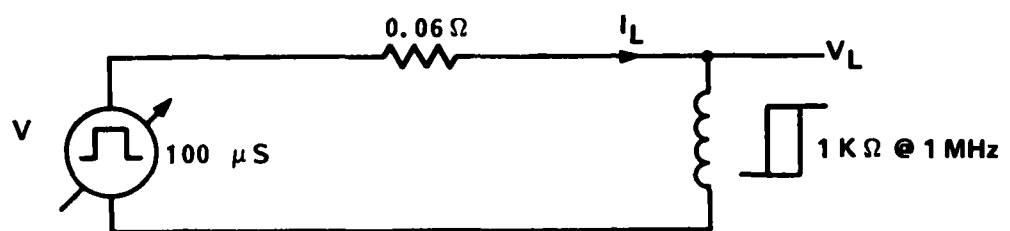


Figure 24. Device high saturation charge characteristics - 6 turns on a Magnetics Incorporated F43813 toroid.

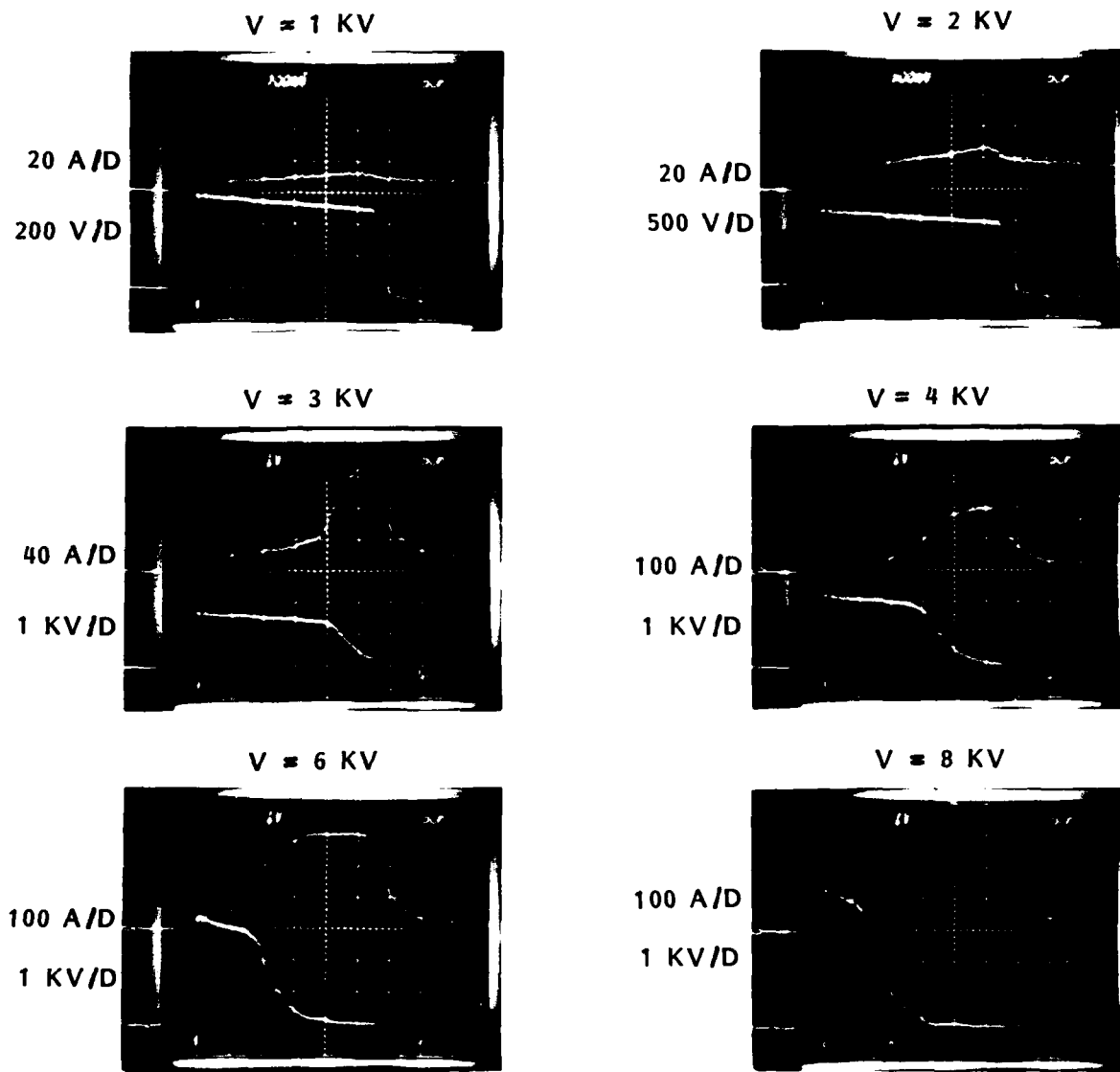
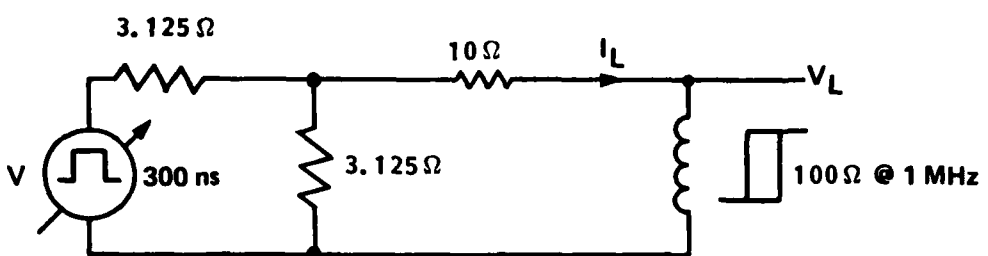


Figure 25. Device switching characteristics - 6 turns on a Magnetics Incorporated F43813 toroid with a 10 mil gap.

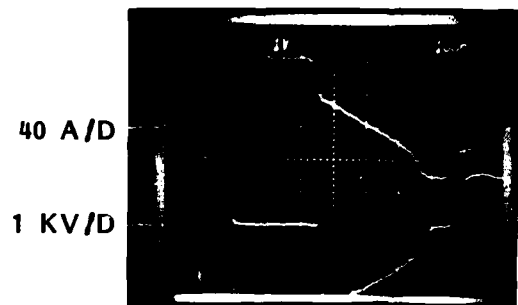
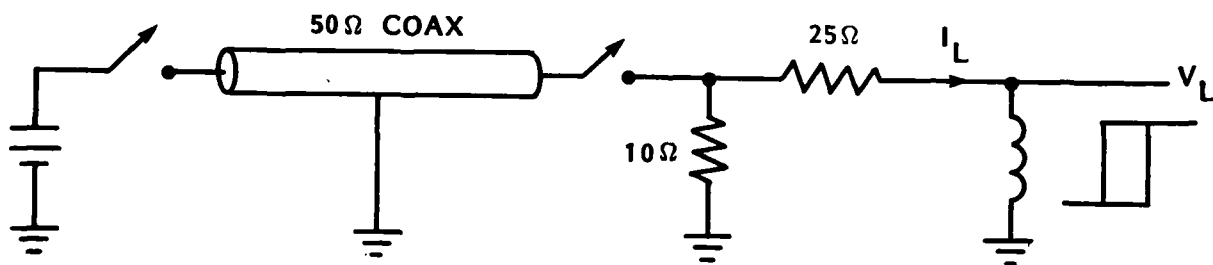


Figure 26. Device saturation recovery characteristics - 4 turns on a Magnetics Incorporated F43813 toroid with a 10 mil gap.

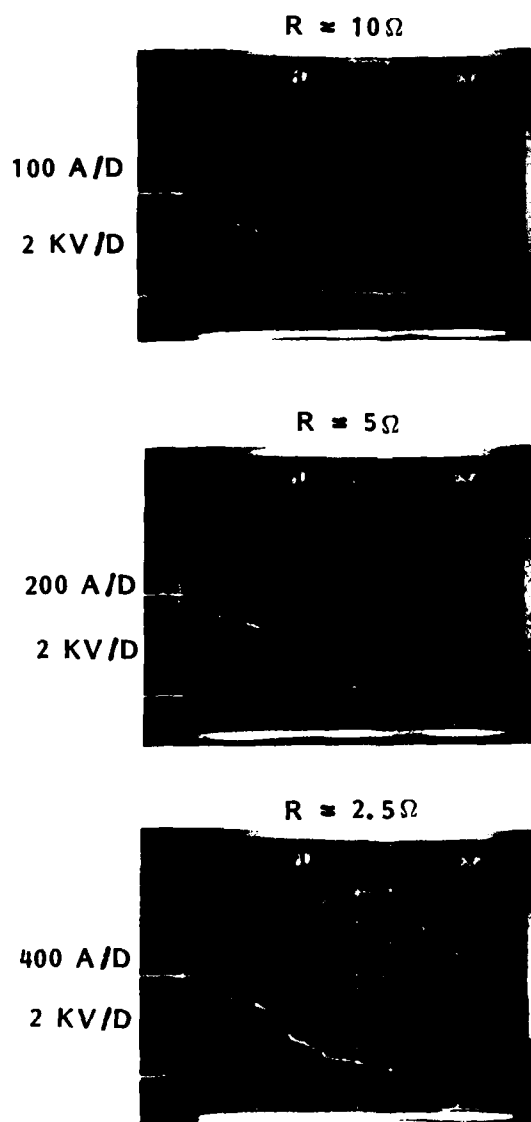
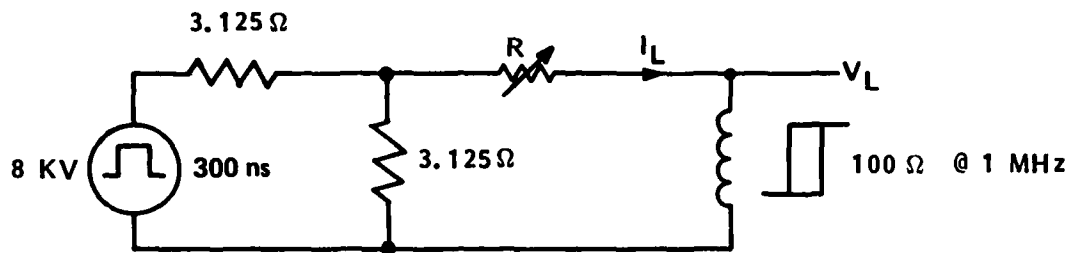


Figure 27. Device saturation charge characteristics - 6 turns on a Magnetics Incorporated F43813 toroid with a 10 mil gap.

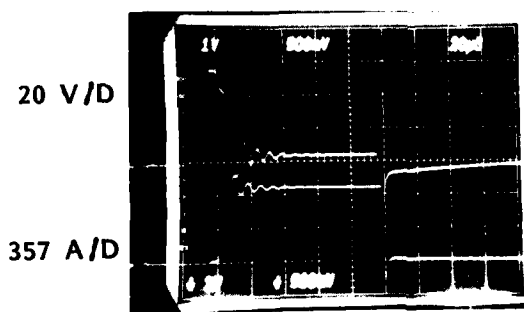
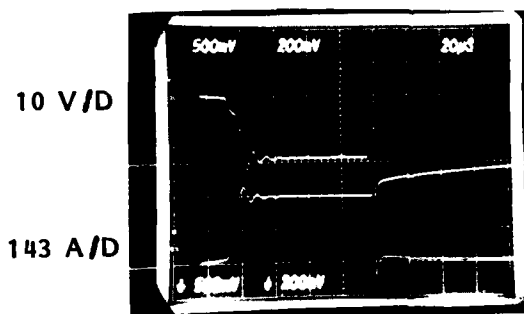
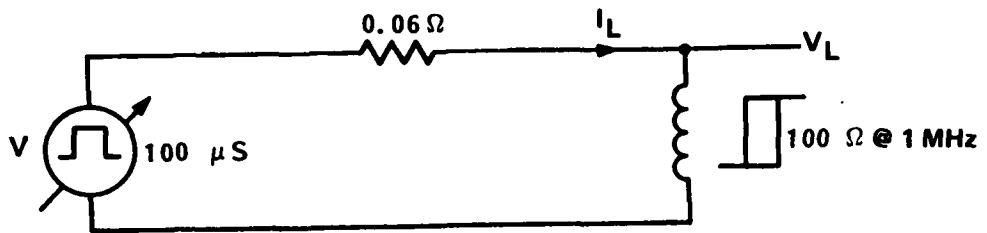


Figure 28. Device high saturation charge characteristics - 6 turns on a Magnetics Incorporated F43813 toroid with a 10 mil gap.

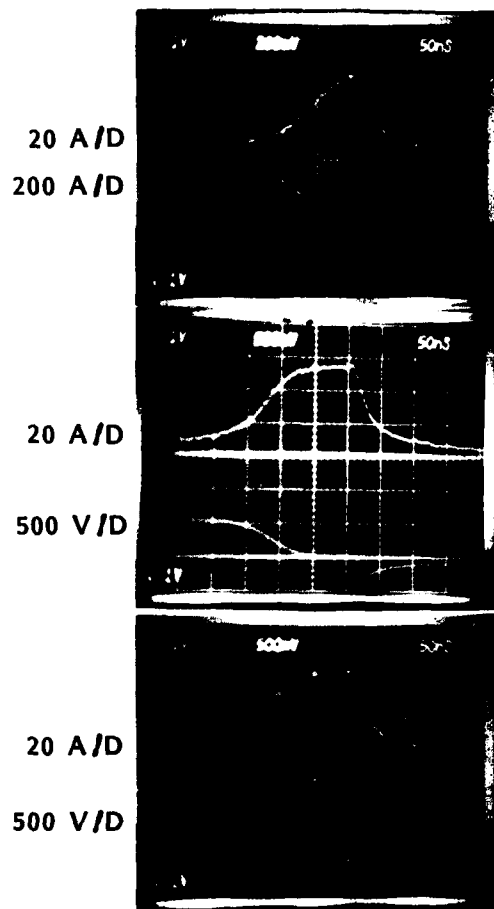
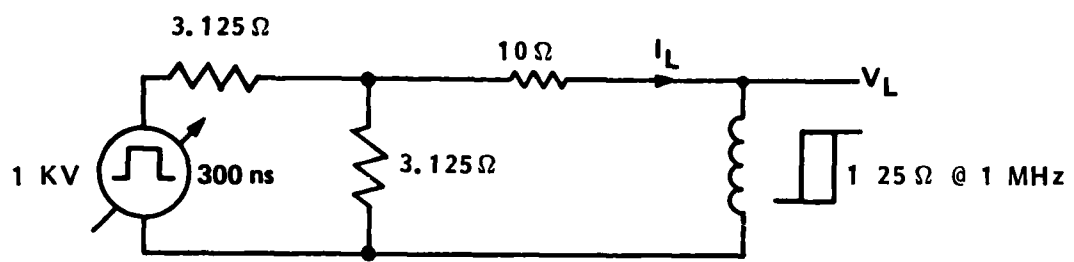


Figure 29. Device switching characteristics - solid rod through 10 Magnetics Incorporated F42206 toroids.

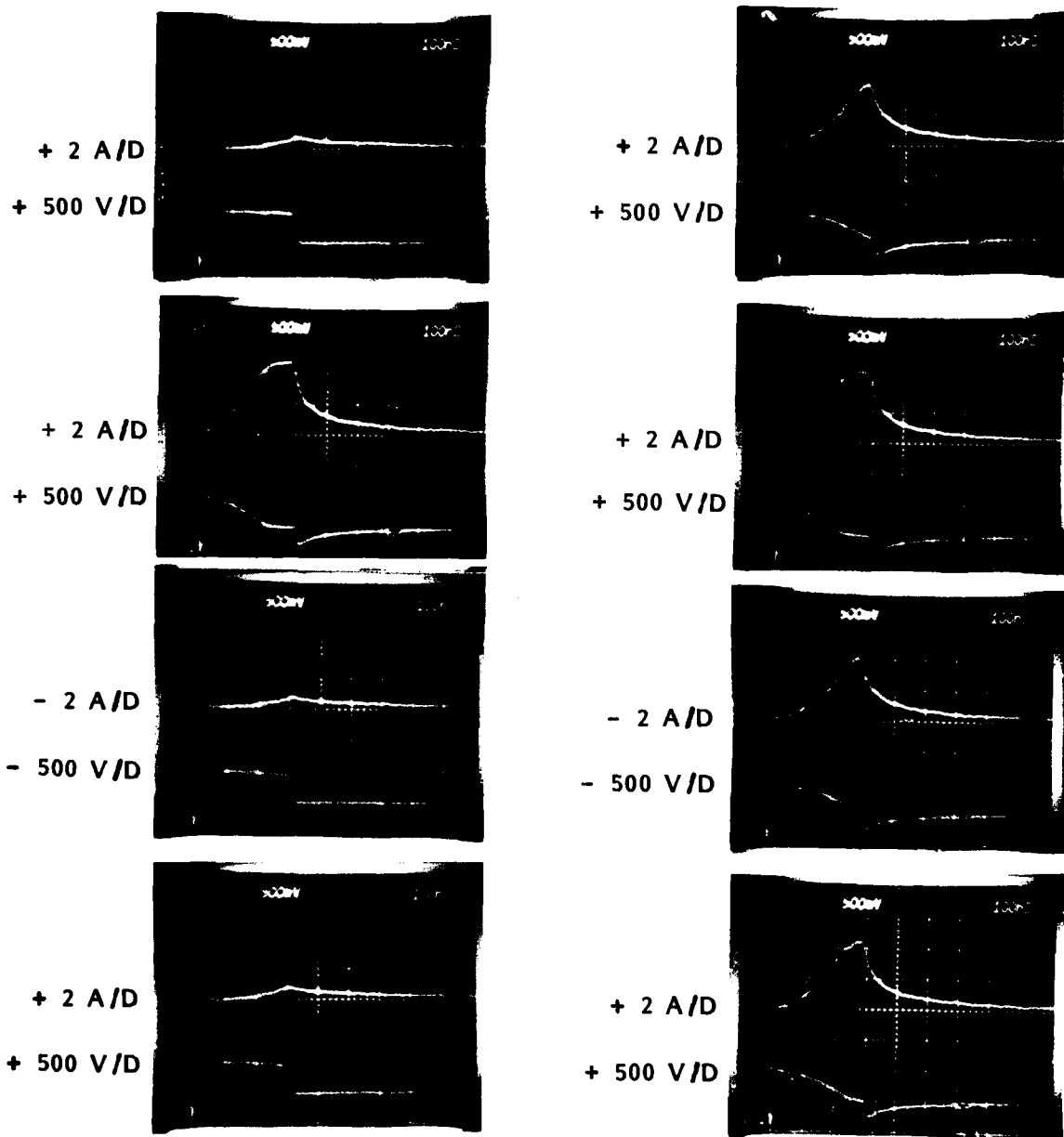
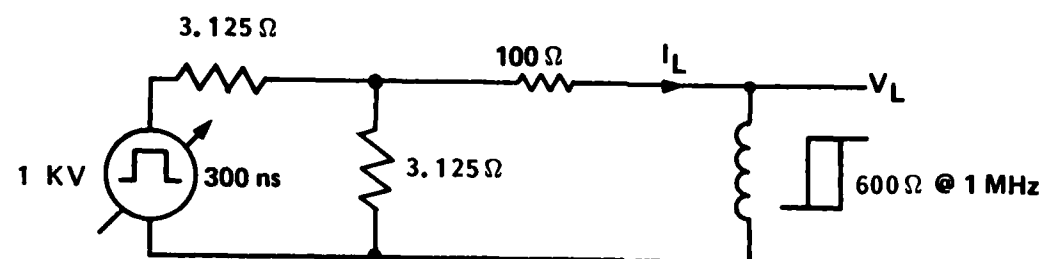


Figure 30. Device switching and residual magnetism characteristics - 6 turns on a ceramic Magnetics Incorporated CMD5005 toroid.

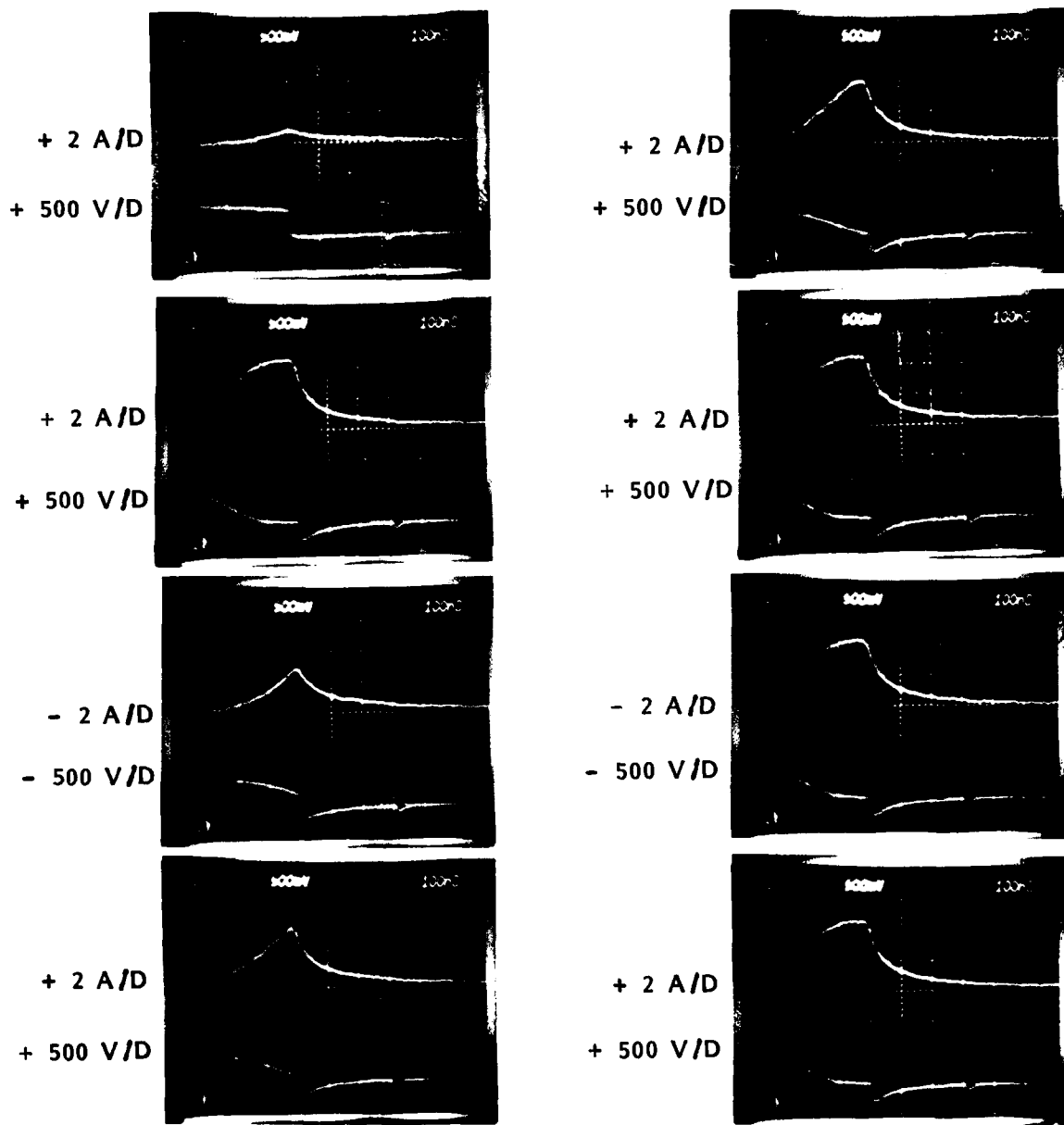
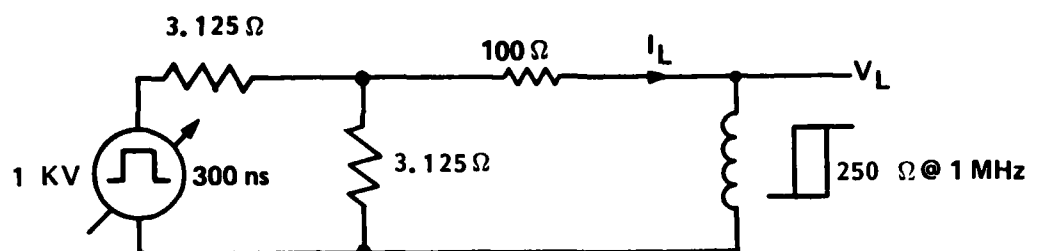


Figure 31. Device switching and residual magnetism characteristics - 6 turns on a ceramic Magnetics Incorporated CN20 toroid.

However, in spite of the high residual magnetism, the devices still exhibit fast saturation recovery characteristics as shown by the data given in Figures 32 and 33.

It has been long known that inserting a gap in a magnetic material inhibits a residual magnetism from being set up in the magnetic circuit. The effects on switching characteristics for gaps in the high residual magnetism materials were demonstrated to be of no concern via experiments using CMI 5005/84-17-3 toroids fabricated with the same 10 mil gap design previously used for the MI F43813 toroids. The data obtained on this device is shown in Figure 34. Here, multiple shots at increasing values of pulser voltage were taken on the device starting with saturation threshold onset, and then the device was taken back to saturation threshold onset. In all cases the gap proved effective in eliminating the residual magnetism effects on " $(V_t)_{sat.}$ " The final area of concern is the applicability of equation 4.7 in describing the sub-microsecond switching characteristics of the magnetic device. Figure 35 shows the comparison of the experimental and calculated values for " V_t "_{sat} for sub-microsecond pulse conditions on the gapped CMD 5005/84-17-3 toroid. As seen, excellent agreement between the model and the experimental data was obtained.

4.3 PERMEABILITY CHARACTERISTICS.

The permeability of a magnetic material is a frequency dependent quantity which has the simplified asymptotic form of

$$\mu = \frac{m}{1 + nf} \quad (4.8)$$

where "m" and "n" are constants and "f" is the frequency. The asymptotic form describes a characteristic which is relatively constant with frequency until the "break frequency" is reached, at which point the quantity decreases with increasing frequency. In general, for magnetic materials the higher the low frequency value of " μ ," the lower the "break frequency" at which point " μ " decreases.

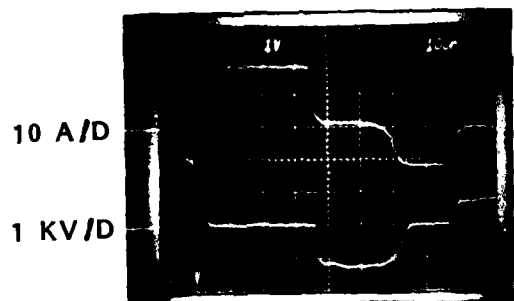
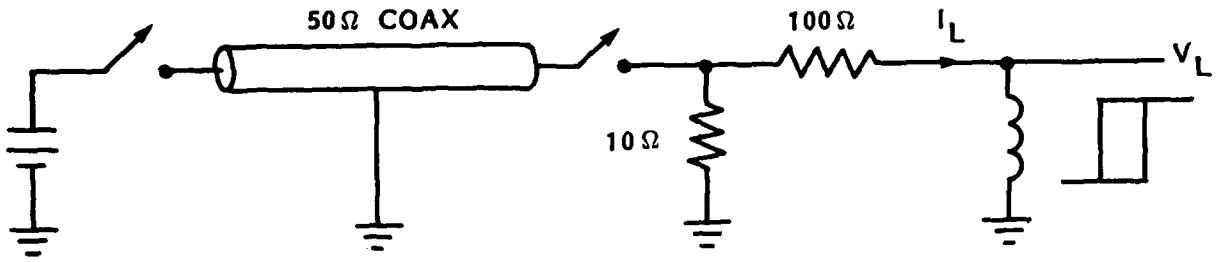


Figure 32. Device saturation recovery characteristics - 6 turns on a Ceramic Magnetics Incorporated CMD5005 toroid.

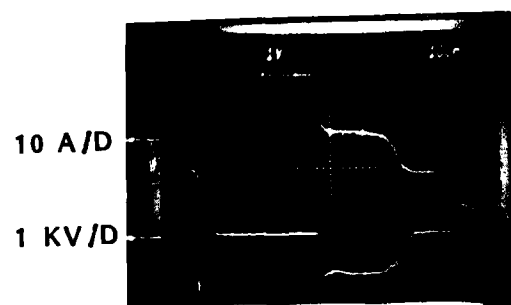
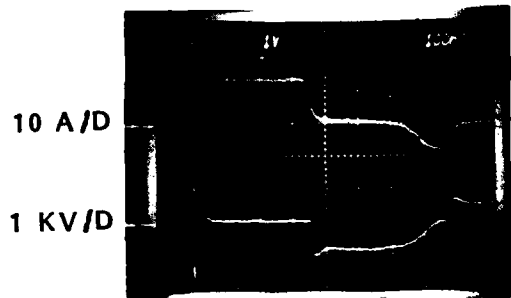
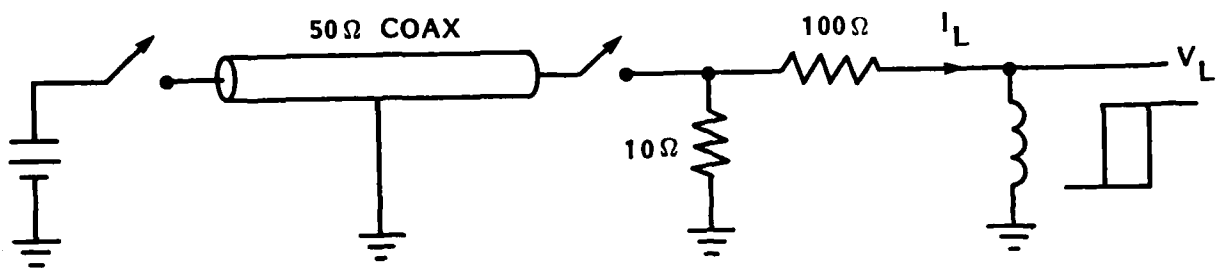


Figure 33. Device saturation recovery characteristics - 6 turns on a Ceramic Magnetics Incorporated CN20 toroid.

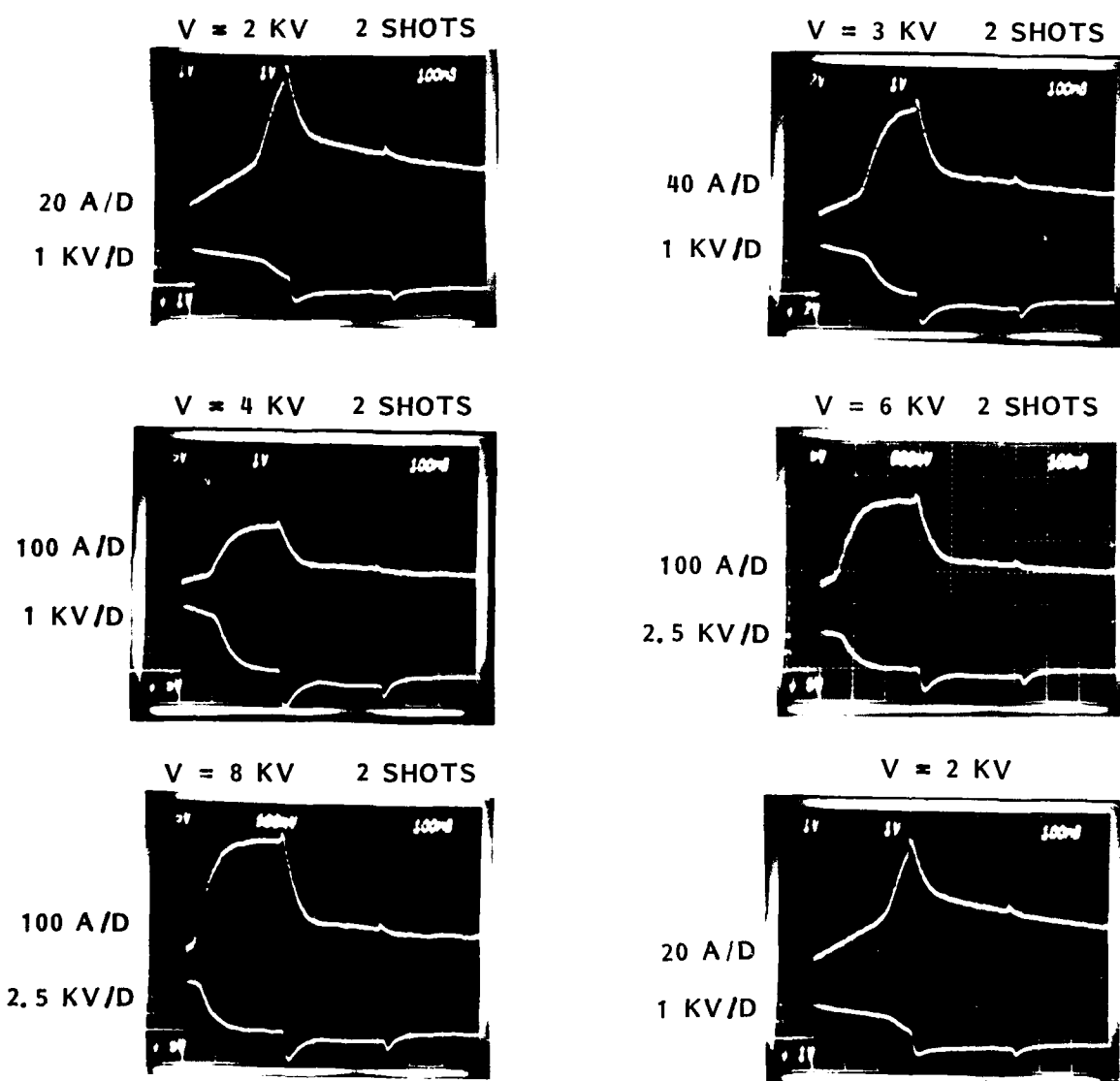
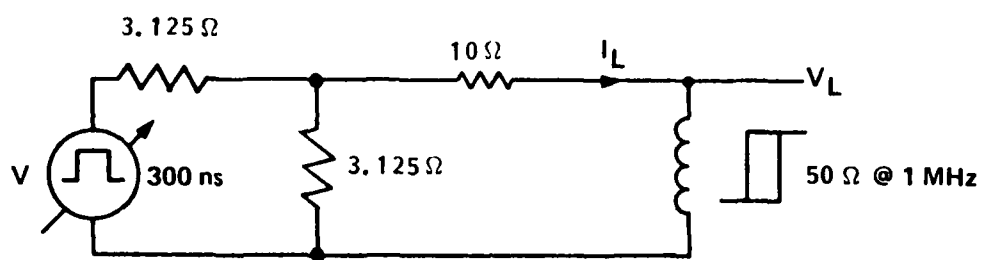
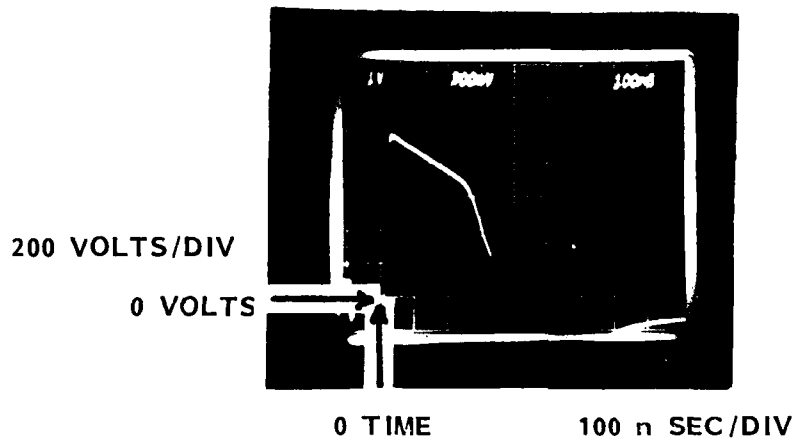


Figure 34. Device switching and residual magnetism characteristics - 6 turns on a Ceramic Magnetics Incorporated CMD5005/84-17-3 toroid with a 10 mil gap.



$$A_c = 1.2 \times 10^{-4} \text{ m}^2$$

$$B_{SAT} = 3.1 \times 10^3 \text{ GAUSS}$$

$$\text{CALCULATED } "V_t"_{SAT} = 223 \times 10^{-6} \text{ VOLT-SEC}$$

$$\text{EXPERIMENTAL } "V_t"_{SAT} = 224 \times 10^{-6} \text{ VOLT-SEC}$$

Figure 35. Comparison of experimental and calculated "V-t" saturation levels for 6 turns on a Ceramic Magnetics Incorporated CMD5005/84-17-3 toroid with a 10 mil gap.

The introduction of gaps in magnetic materials decreases the initial value of " μ " and increases the "break frequency." This can be understood by examining Figure 36. From (4.2) we can write

$$L_1 \propto \frac{\mu_1}{l_1} \quad \& \quad L_2 \propto \frac{\mu_2}{l_2} \quad (4.9)$$

and

$$L_{\text{equivalent}} = \frac{\mu_{\text{equivalent}}}{l_{\text{total}}} \quad (4.10)$$

since

$$L_{\text{equivalent}} = \frac{L_1 L_2}{L_1 + L_2} \quad (4.11)$$

we can write

$$\mu_{\text{equivalent}} = l_{\text{total}} \left(\frac{\mu_1 \mu_2}{\mu_1 l_2 + \mu_2 l_1} \right) \quad (4.12)$$

Since " $\mu_1 = 1$ " for the gap and if $l_1 \ll l_2$, then $l_{\text{total}} \sim l_2$ and

$$\mu_{\text{equivalent}} = \frac{l_2 \mu_2}{l_2 + \mu_2 l_1} \quad (4.13)$$

$$= \mu_2 \left\{ \frac{1}{1 + \mu_2 \frac{l_1}{l_2}} \right\} \quad (4.14)$$

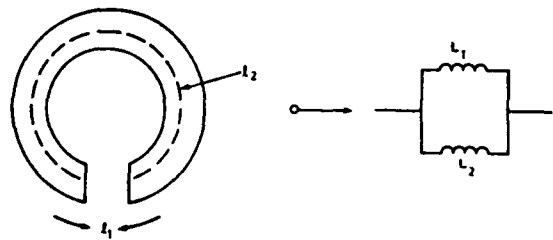


Figure 36. Equivalent circuit of a magnetic toroid containing a gap.

now if while $l_1 \ll l_2$, $\mu_2 l_1 > l_2$, then

$$\mu_{\text{equivalent}} \sim \frac{l_2}{l_1} \quad (4.15)$$

which is independent of frequency as long as $\mu_2 l_1 > l_2$

A number of gapped toroids of CMI's CMD 5005 material were fabricated with controlled gaps using bond paper saturated with Eastman 910 adhesive. The toroids were special request perfect halves pre-cut and supplied through the courtesy of CMI. Gaps of 6, 20 and 30 mil total length were fabricated along with a so called "minimal gap" which was formed by joining the toroids together with just a thin coating of Eastman 910. Inductors with 3 turns were then formed and device impedances measured as a function of frequency using a Hewlett-Packard Vector Impedance Meter. Equation (4.2) was used to calculate the relative permeability of the gapped cores from the impedance-frequency data. The experimentally based results are shown in Figure 37. A comparison of the data at 1 MHz to that calculated using equation (4.14) and the manufacturers value of 1200 for the solid material at 1 MHz yields the following good agreement:

GAP	μ_R EXPERIMENTAL	μ_R CALCULATED
6 mil	300	487
20 mil	170	204
30 mil	132	144

4.4 RF LOSS CHARACTERISTICS.

The RF loss characteristics of the magnetic device are manifested as insertion losses between a circuit and load due to the device impedance, and self heating losses in the magnetic material itself.

For insertion loss considerations in the simplest case, neglecting core losses and interwire capacitance, the magnetic device can be considered as an ideal inductor. Here, maximum insertion loss results from applying

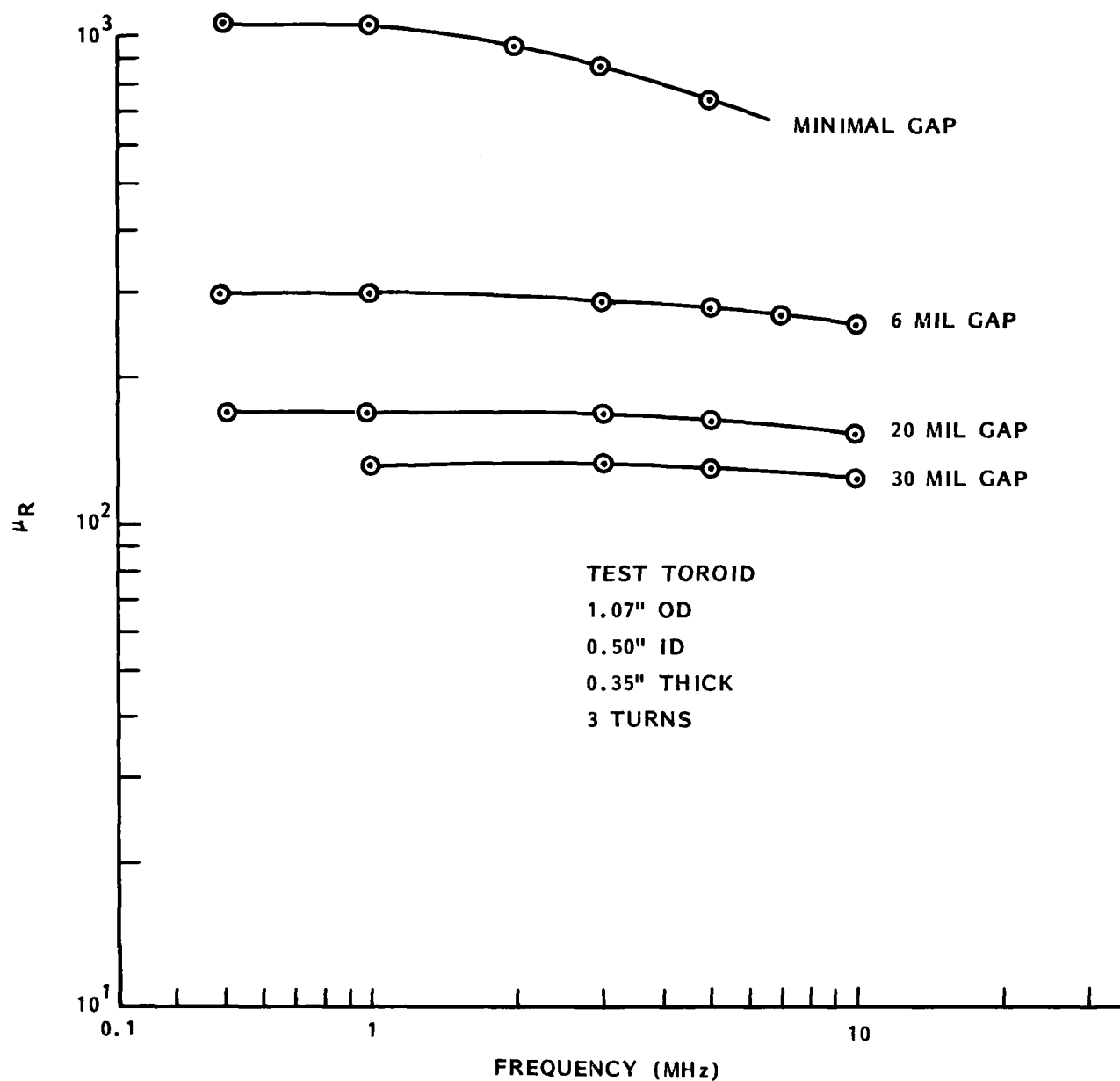


Figure 37. Relative permeability of Ceramic Magnetics Incorporated CMD5005 ferrite material.

the magnetic device directly across a circuit at a single node without any frequency compensation. In this case, the equivalent circuit for insertion loss in a Z_0 impedance system is as shown in Figure 38. Here insertion loss in db is given by

$$db = 20 \log_{10} \left(\sqrt{1 + \frac{Z_0^2}{4\omega^2 L_u^2}} \right) \quad (4.16)$$

or, rearranging

$$\frac{1}{\omega L_u} = \frac{1}{2\pi f L_u} = \frac{1}{X_{L_u}} = \frac{2}{Z_0} \sqrt{10 \text{db}/10 - 1} \quad (4.17)$$

The self heating losses in a magnetic material, in terms of the dissipated power per unit volume of material, are given by an empirically simplified version of Legg's equation as

$$P_V = a B_0^b \quad (4.18)$$

where: "a" and "b" are frequency dependent, such that P_V increases with frequency.

At any particular frequency the current through the unsaturated inductor is related to the voltage across the device by

$$I = \frac{V}{2\pi f L_u} \quad (4.19)$$

Substituting (4.19) into (4.1) and then (4.2) into this result yields

$$B_0 = \frac{10^4 V}{2\pi f N A_c} \quad (4.20)$$

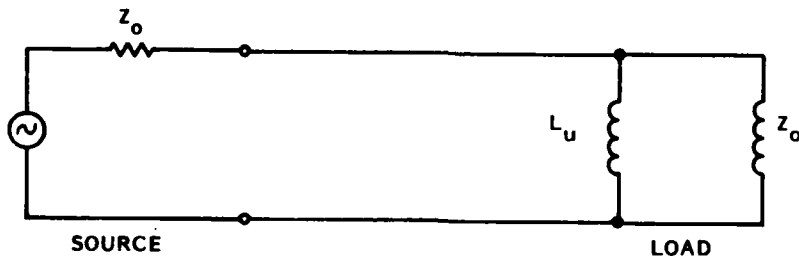


Figure 38. Saturable magnetic device insertion loss equivalent circuit.

Substituting (4.20) now into (4.18) yields

$$P_V = a \left\{ \frac{10^4 V}{2\pi f N A_C} \right\}^b \quad (4.21)$$

Recalling equation (4.18), the self heating losses are such that "P_V" increases with frequency and with operating flux density. The ultimate effect of these losses is as follows: as a minimum they could heat the device beyond the Curie temperature (which is reversible upon cooling for the ferrite materials) and drive the device into saturation; while at worst case they could produce severe thermal stresses and fracture the material.

Unfortunately very little data was available concerning the ultimate power-frequency limitations of these types of materials at severe RF applications. In view of this, the present program was required to perform an extensive characterization of the candidate magnetic materials considered for use in the HESA prototype, similar to that required for the GE-MOV® varistors. Again, these studies were limited to application oriented studies where specific toroid inductor/material configurations were placed across the output of a 50 ohm RF transmitter which was driving a 50 ohm load. At any one particular frequency, RF transmitter power level was slowly increased until the Curie temperature was reached and the device was switched into saturation. At this point, the transmitter was turned off, the device allowed to cool, the frequency changed and the procedure repeated again. Experiments were performed at both ambient and ice water immersion conditions. In the severest cases, the thermal stresses resulted in toroid fractures.

Equation (4.21) indicates that for a fixed frequency and voltage level, the core losses induced in the magnetic material will be inversely proportional to "(N)^b". The MI type F ferrite, for example, has a value of "b ~ 2" at high frequencies (1 MHz is the highest frequency for which manufacturer's data is available). Hence, for these materials the core losses should be inversely proportional to "N²" for a fixed voltage and frequency. Now another way of looking at this is that at a fixed frequency the voltage level that will be required to produce the same thermal

effects in the material should increase as the square of the turns. However, in considering the RF transmitter applications test we can restate the last premise for the MI type F material as "the RF transmitter power level to produce the same thermal effects should increase linearly with the toroid turns at a fixed frequency." A number of experiments were performed using 3-to-40 turns in two different toroid geometries of the MI type F material at 30 MHz to evaluate this premise. These results, which are given in Figure 39, show that the RF transmitter power which drives the toroids beyond the Curie point does indeed vary linearly with toroid turns for this material type.

Additional MI data up to 1 MHz on the type F material indicates that "a" in (4.21) varies as " f^2 ". Since "b" \propto f^2 then we would expect that the maximum RF transmitter power level that these devices can withstand should be somewhat independent of frequency and should increase with turns and toroid cross sectional area. The data shown in Figures 40 through 44 bears this out. This data also shows the dramatic increase in RF transmitter power capability achievable with an ice water immersion of the toroids. An interesting approximate equivalency between 10 turns on a single toroid and 1 turn on 10 toroids can be observed by comparing the data given in Figures 41 and 45. More will be said about this aspect in Section 4.6.

The data shown in Figures 46 through 51 for various turns and toroid configurations for four different CMI material types demonstrate qualitatively similar results as that obtained on the MI materials.

4.5 RF SELF HEATING LOSS AND THERMAL STRESS REDUCTION METHODS.

The material response data given in Figures 40 through 42 and 45 through 47 clearly shows the advantage of ambient temperature reductions on the ultimate RF transmitter power capability of the magnetic devices. Although approaches such as this which involve active cooling methods were observed to be comparatively more effective when applied to the magnetic devices as compared to the varistor devices, they still, however, introduce an added complexity to the HESA which is generally undesirable.

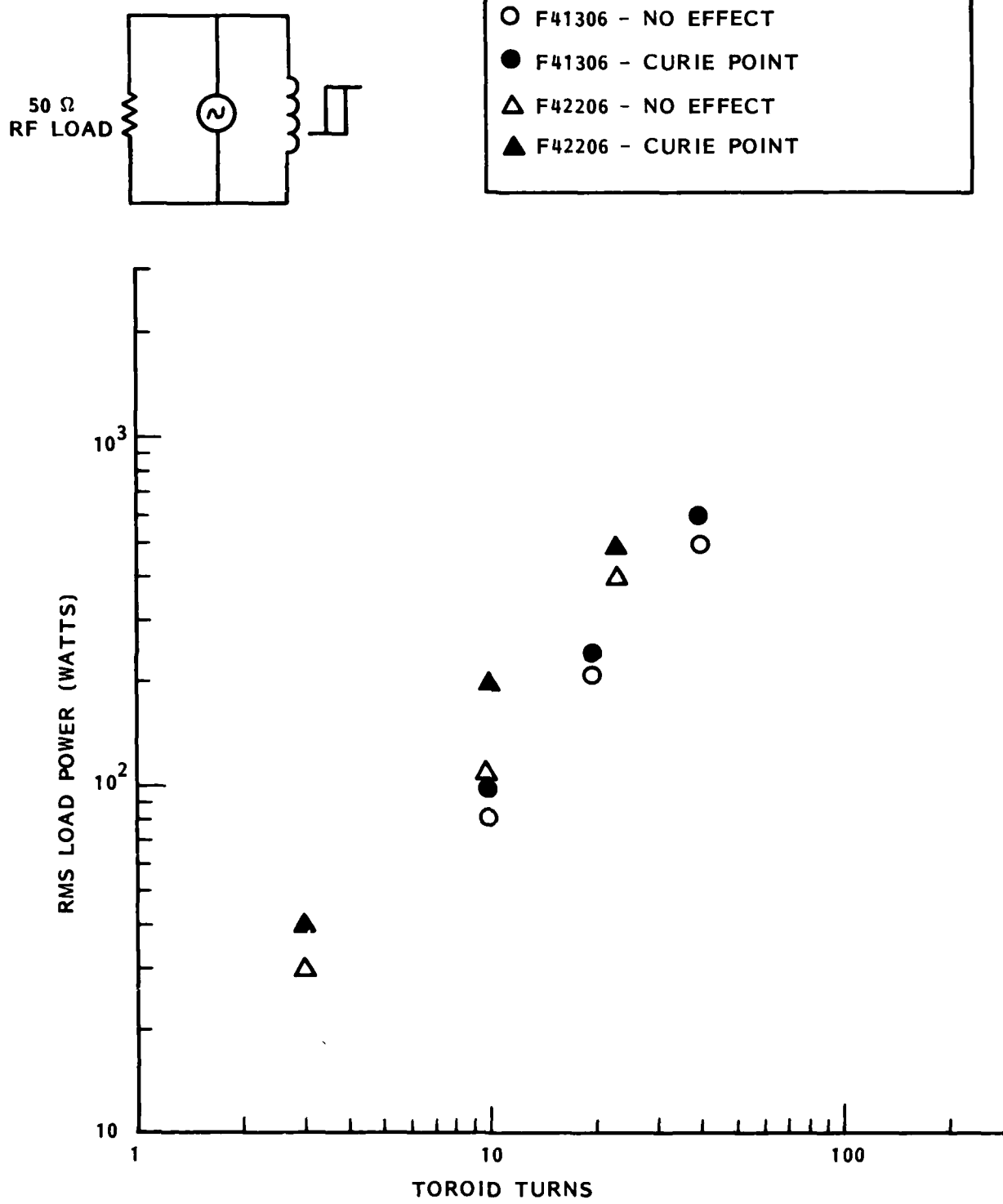
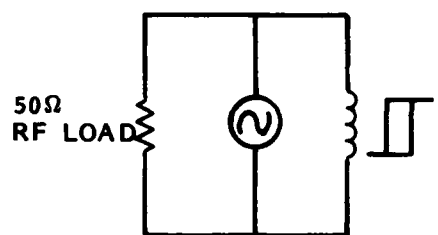


Figure 39. Free air core loss characteristics of Magnetics Incorporated Type F material at 30 MHz as a function of toroid turns.



- FREE AIR - NO EFFECT
- FREE AIR - CURIE POINT
- △ ICE WATER - NO EFFECT
- △ ICE WATER - CURIE POINT

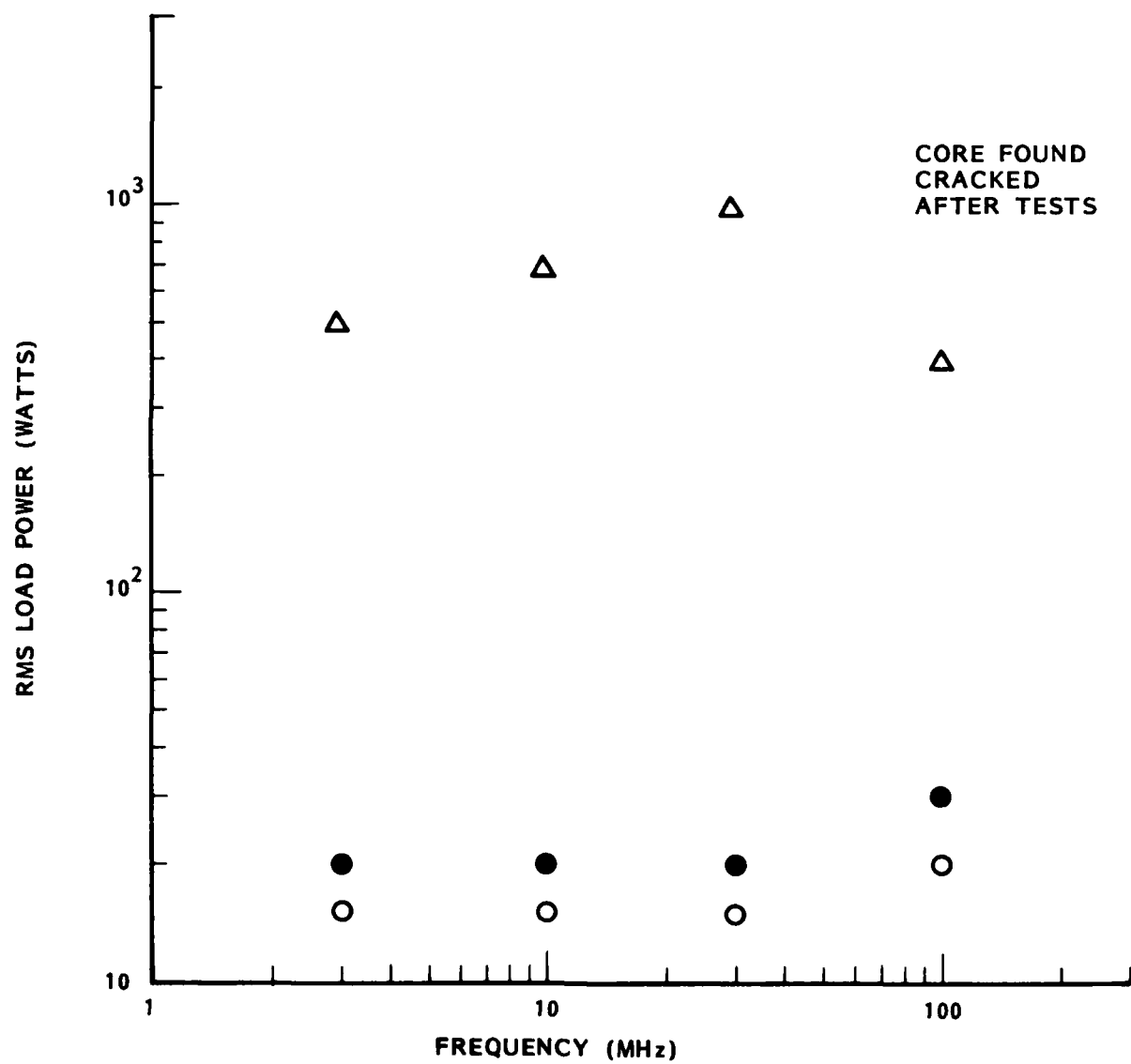
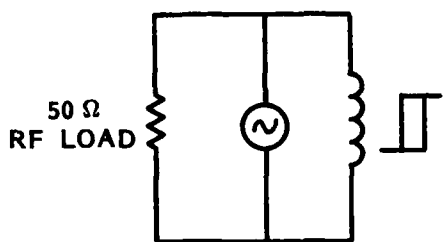


Figure 40. Core loss characteristics - 3 turns on a Magnetics Incorporated F41306 toroid.



- FREE AIR - NO EFFECT
- FREE AIR - CURIE POINT
- △ ICE WATER - NO EFFECT
- ▲ ICE WATER - CURIE POINT

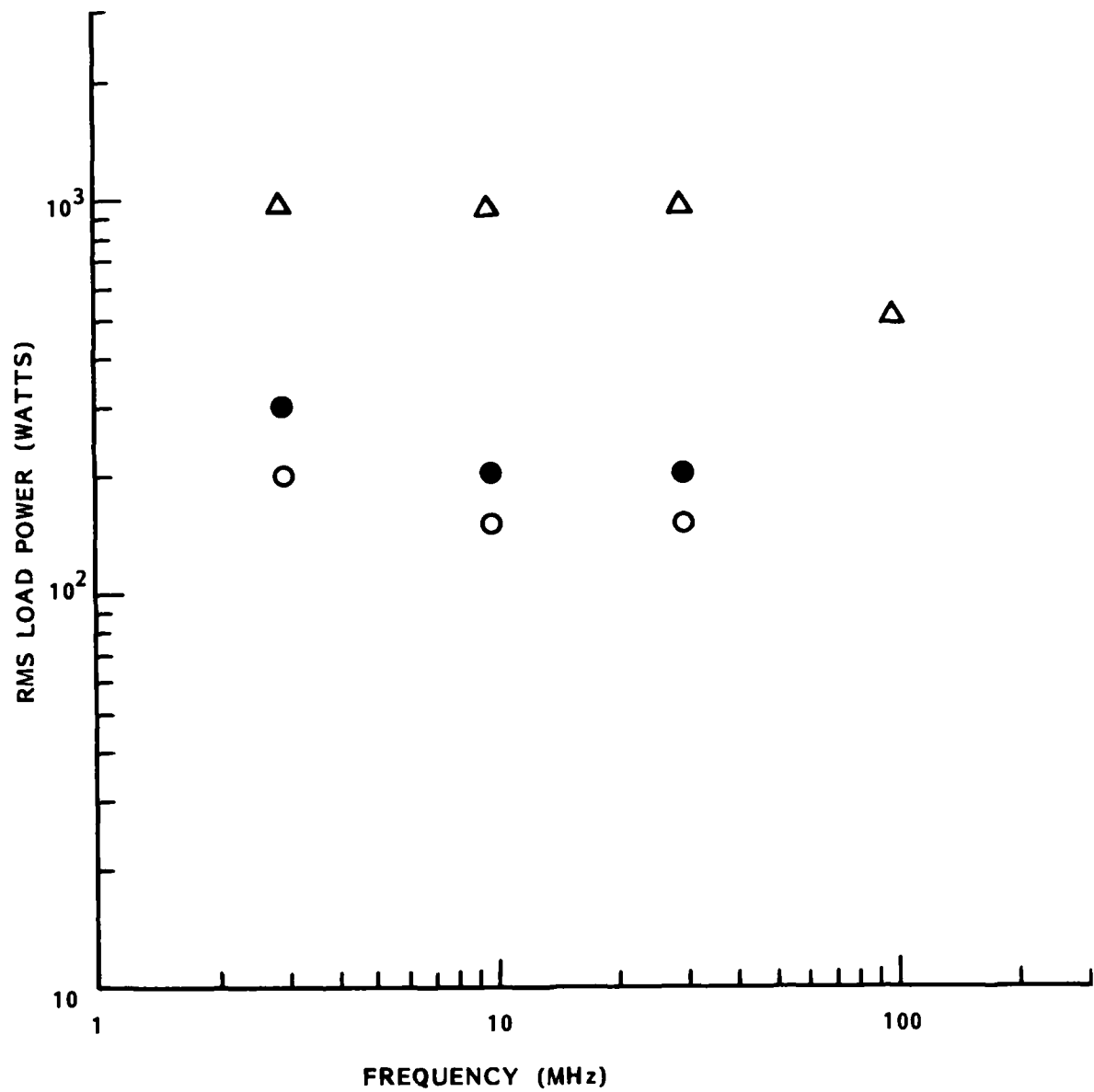
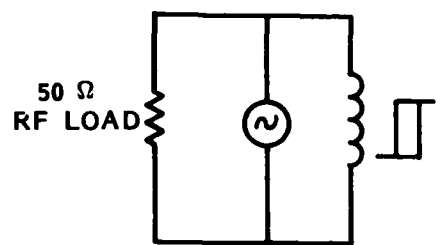


Figure 41. Core loss characteristics - 10 turns on a Magnetics Incorporated F41306 toroid.



- FREE AIR - NO EFFECT
- FREE AIR - CURIE POINT
- △ ICE WATER - NO EFFECT
- ▲ ICE WATER - CURIE POINT

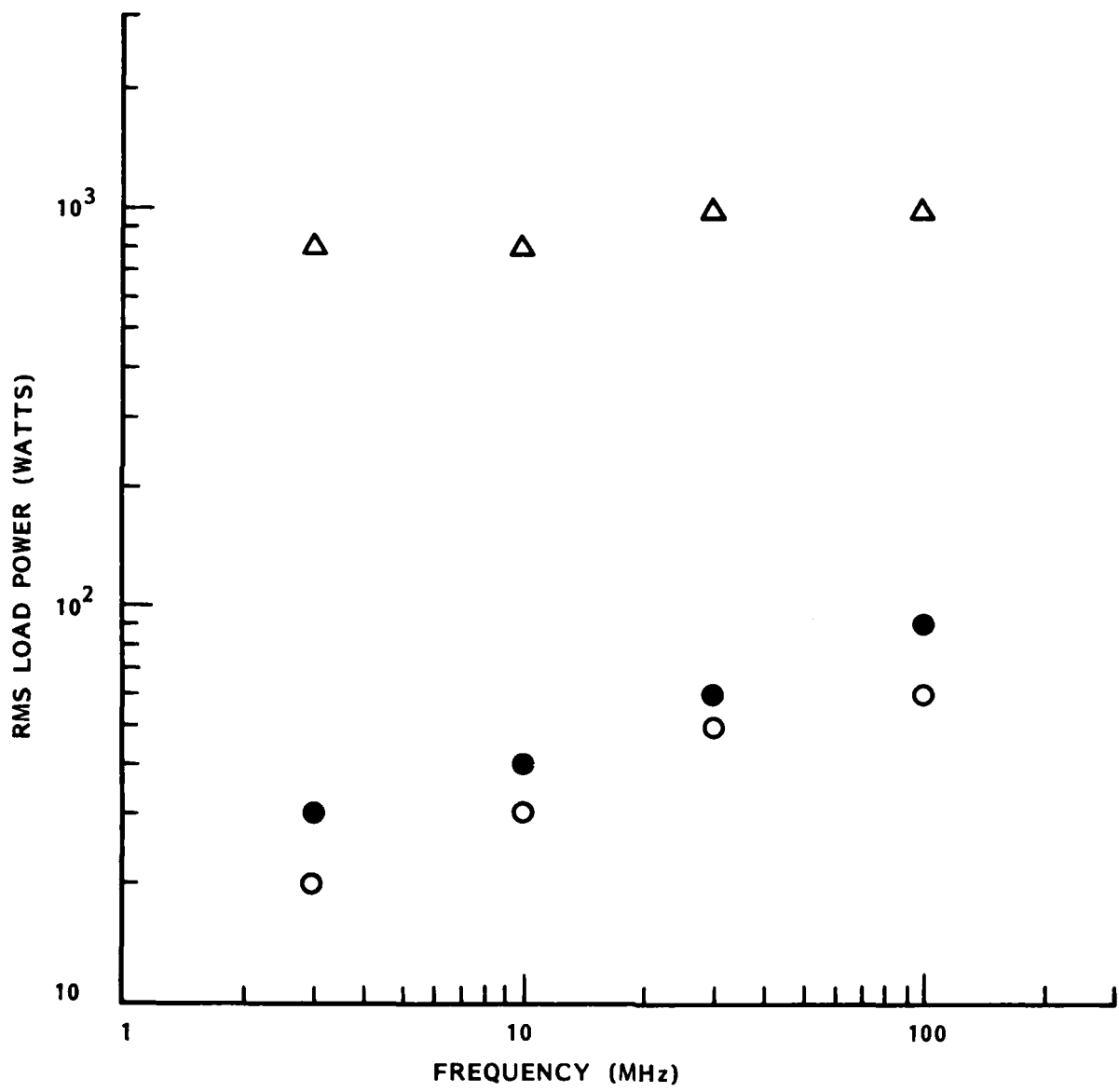


Figure 42. Core loss characteristics - 3 turns on a Magnetics Incorporated F42206 toroid.

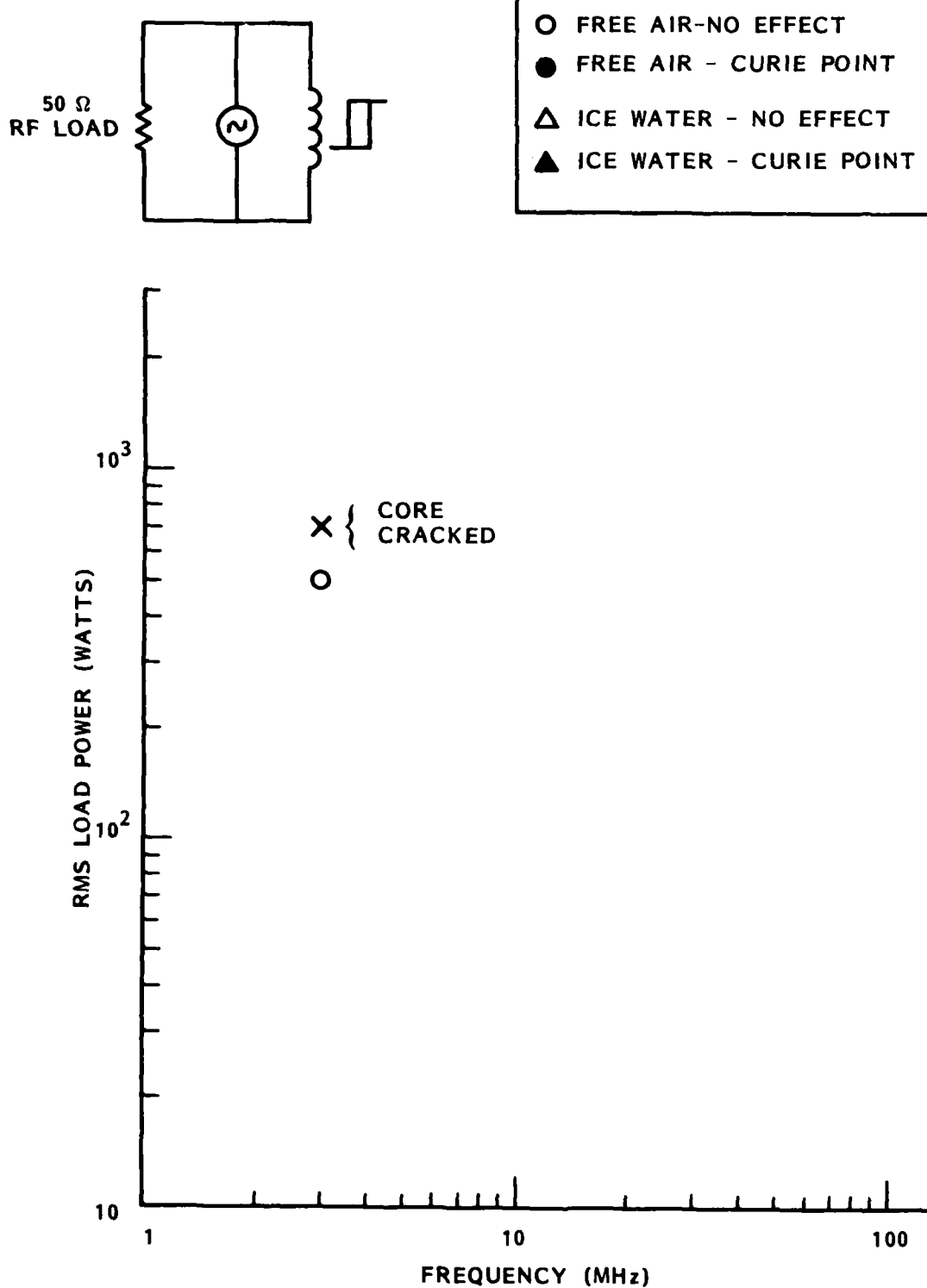
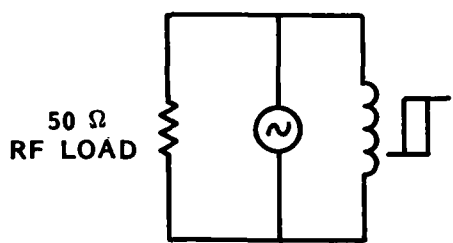


Figure 43. Core loss characteristics - 3 turns on a Magnetics Incorporated F43813 toroid.



- FREE AIR - NO EFFECT
- FREE AIR - CURIE POINT
- △ ICE WATER - NO EFFECT
- ▲ ICE WATER - CURIE POINT

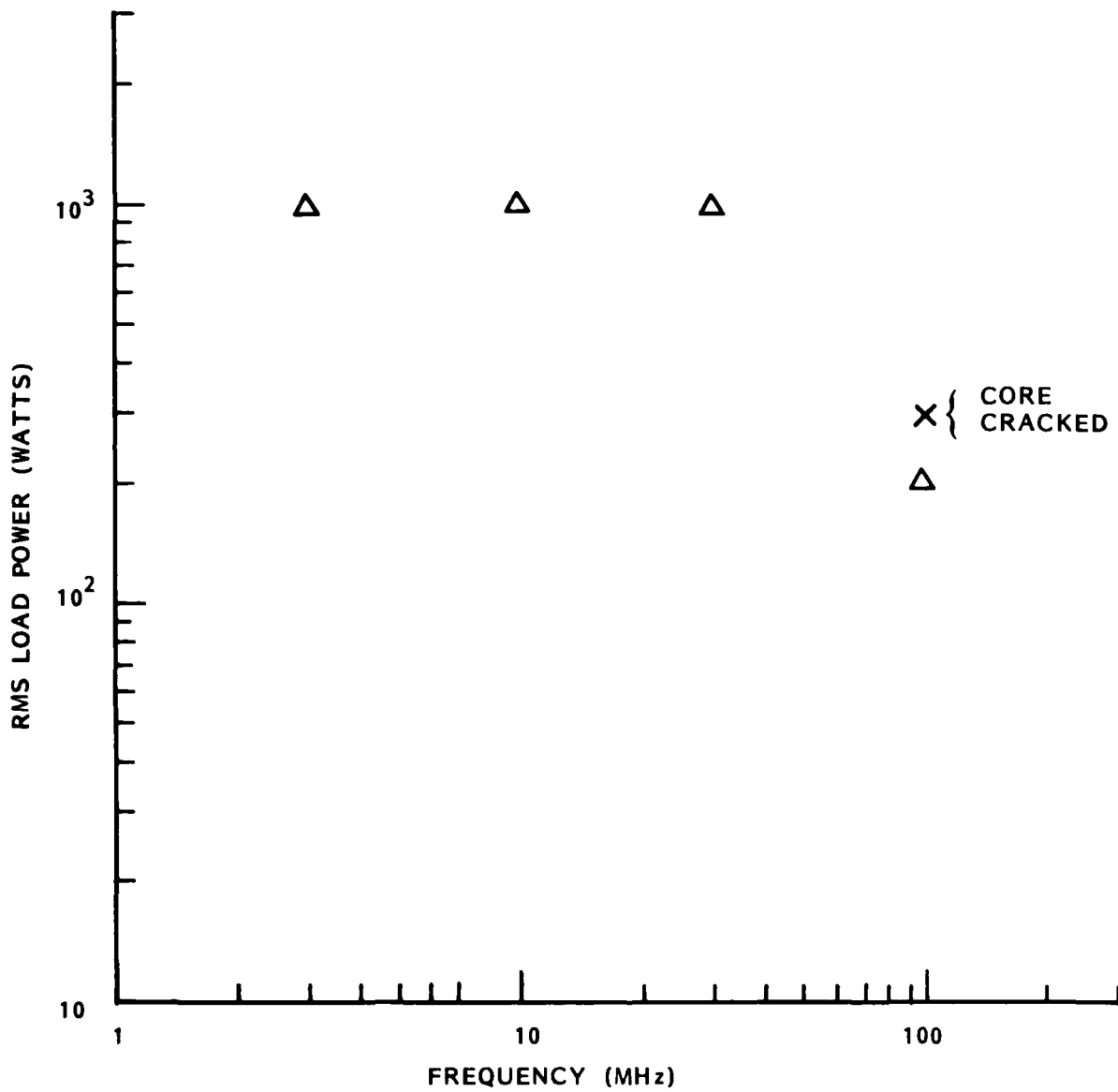


Figure 44. Core loss characteristics - 6 turns on a Magnetics Incorporated F43813 toroid.

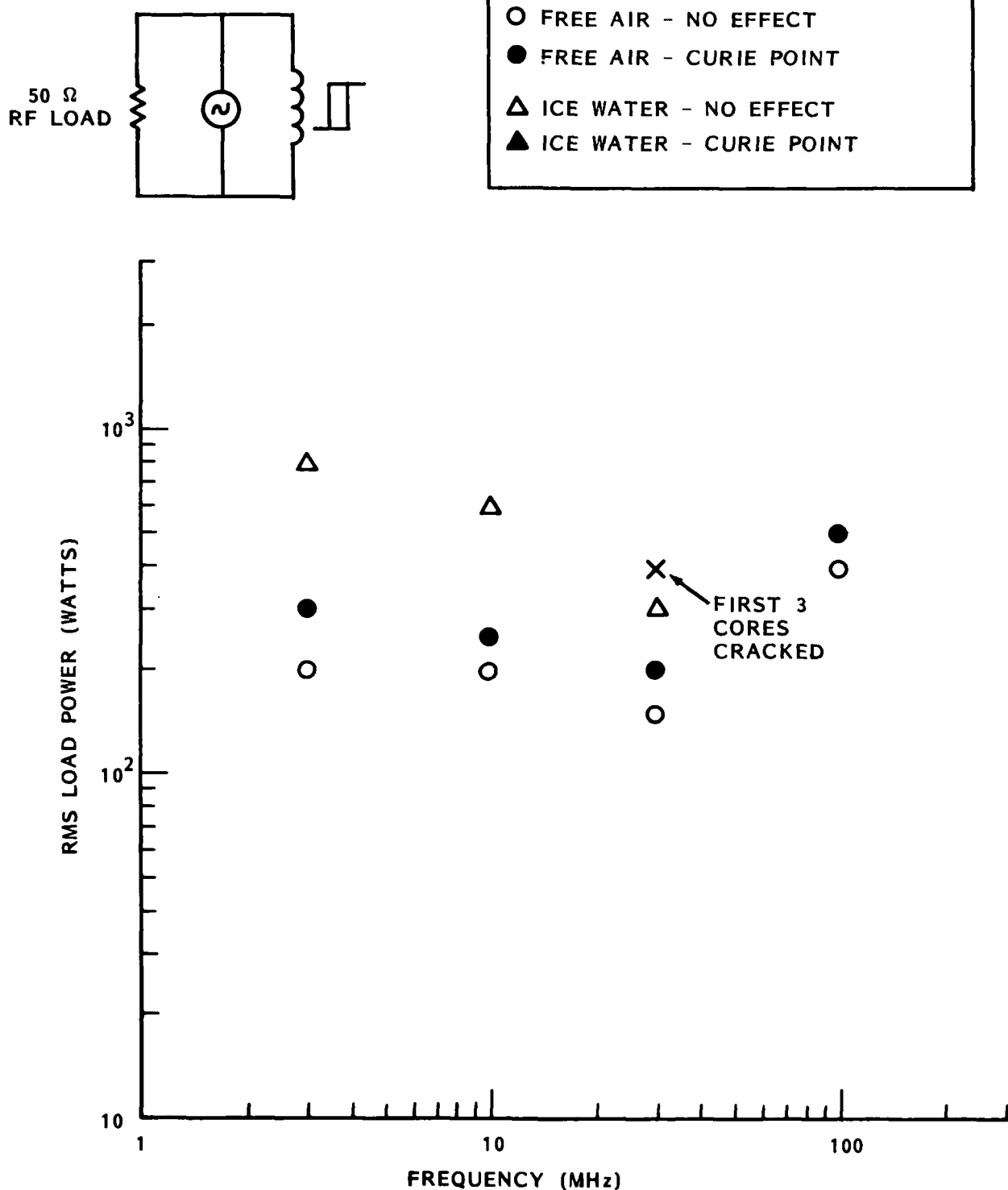


Figure 45. Core loss characteristics - solid rod through 10 Magnetics Incorporated F41306 toroids.

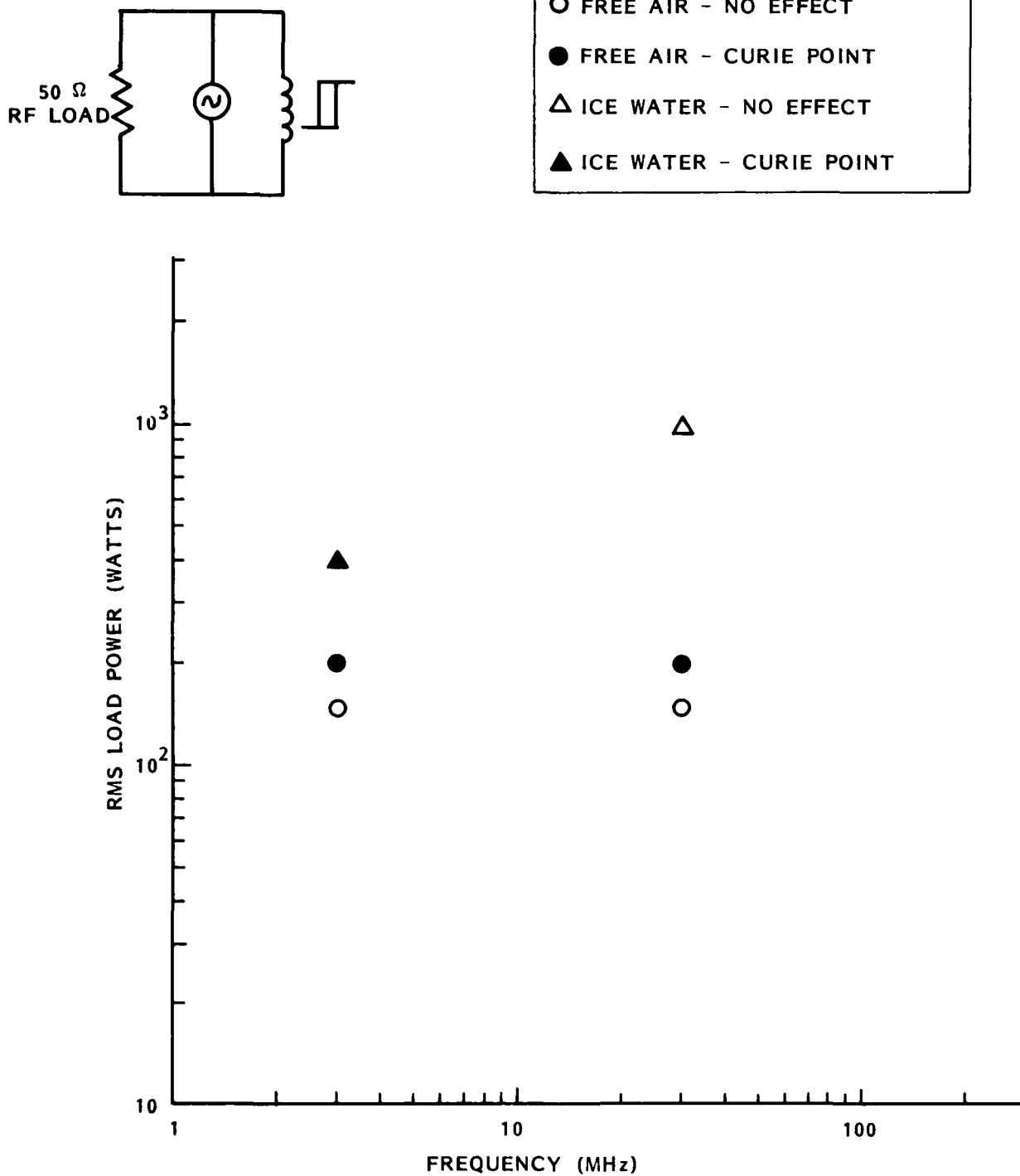


Figure 46. Core loss characteristics - 3 turns on a Ceramic Magnetics Incorporated CN20 toroid.

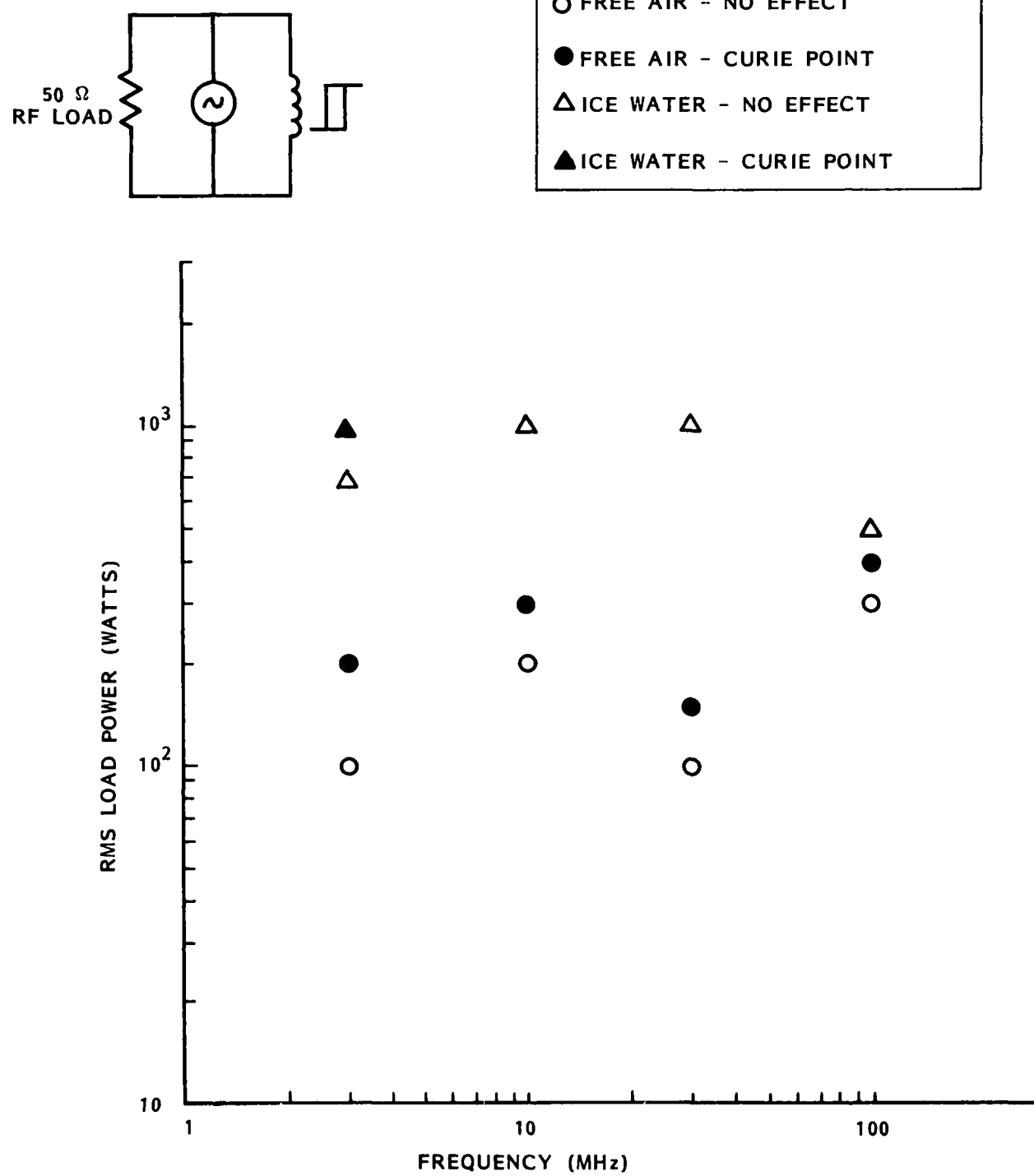


Figure 47. Core loss characteristics - 3 turns on a Ceramic Magnetics Incorporated CMD5005 toroid.

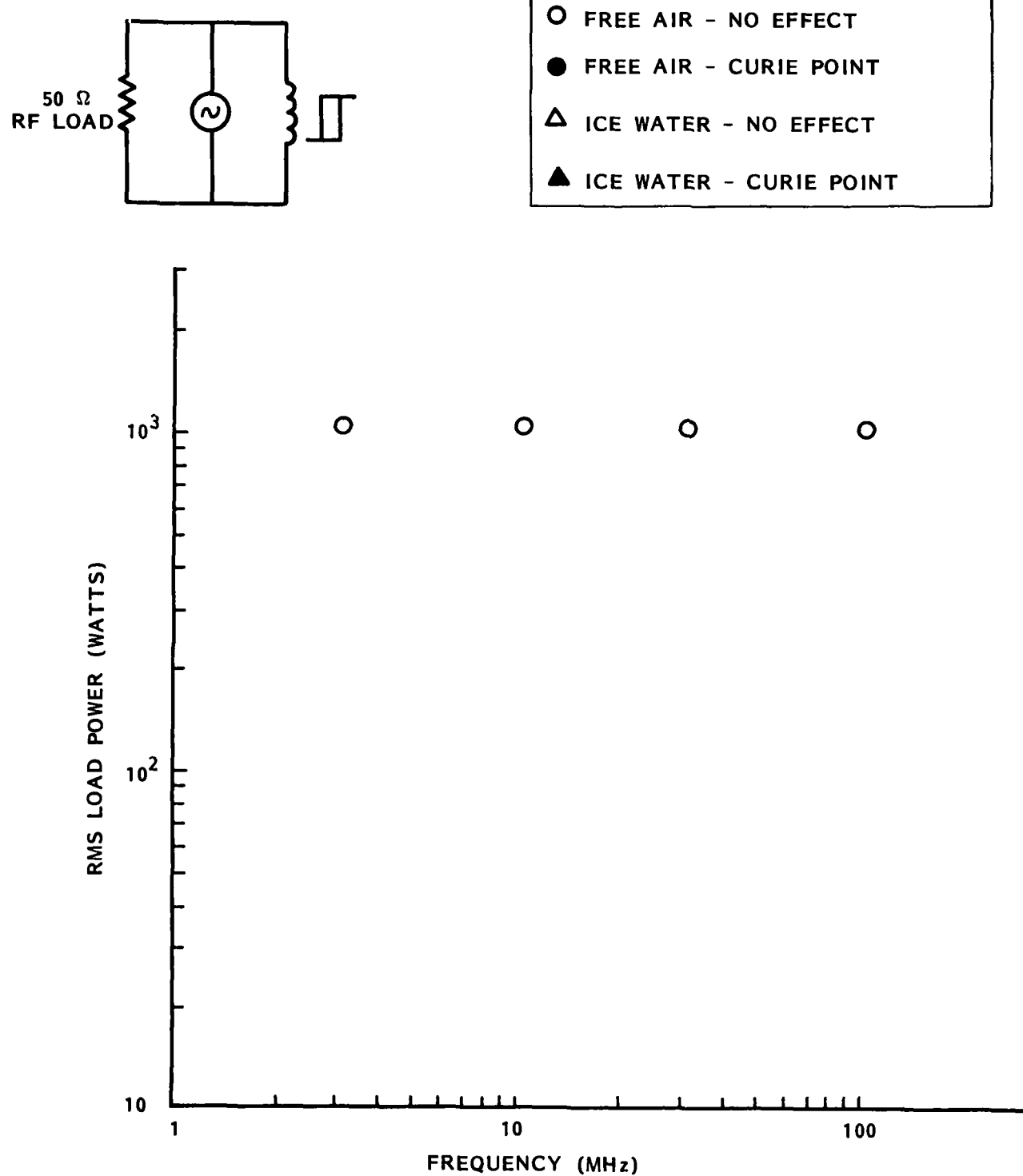
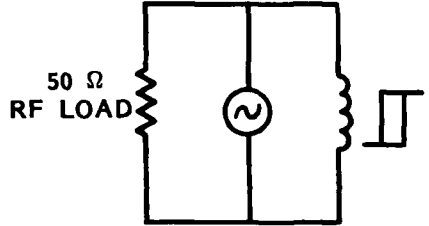


Figure 48. Core loss characteristics - 10 turns on a Ceramic Magnetics Incorporated CMD5005 toroid.



- FREE AIR - NO EFFECT
- FREE AIR - CURIE POINT
- △ ICE WATER - NO EFFECT
- ▲ ICE WATER - CURIE POINT

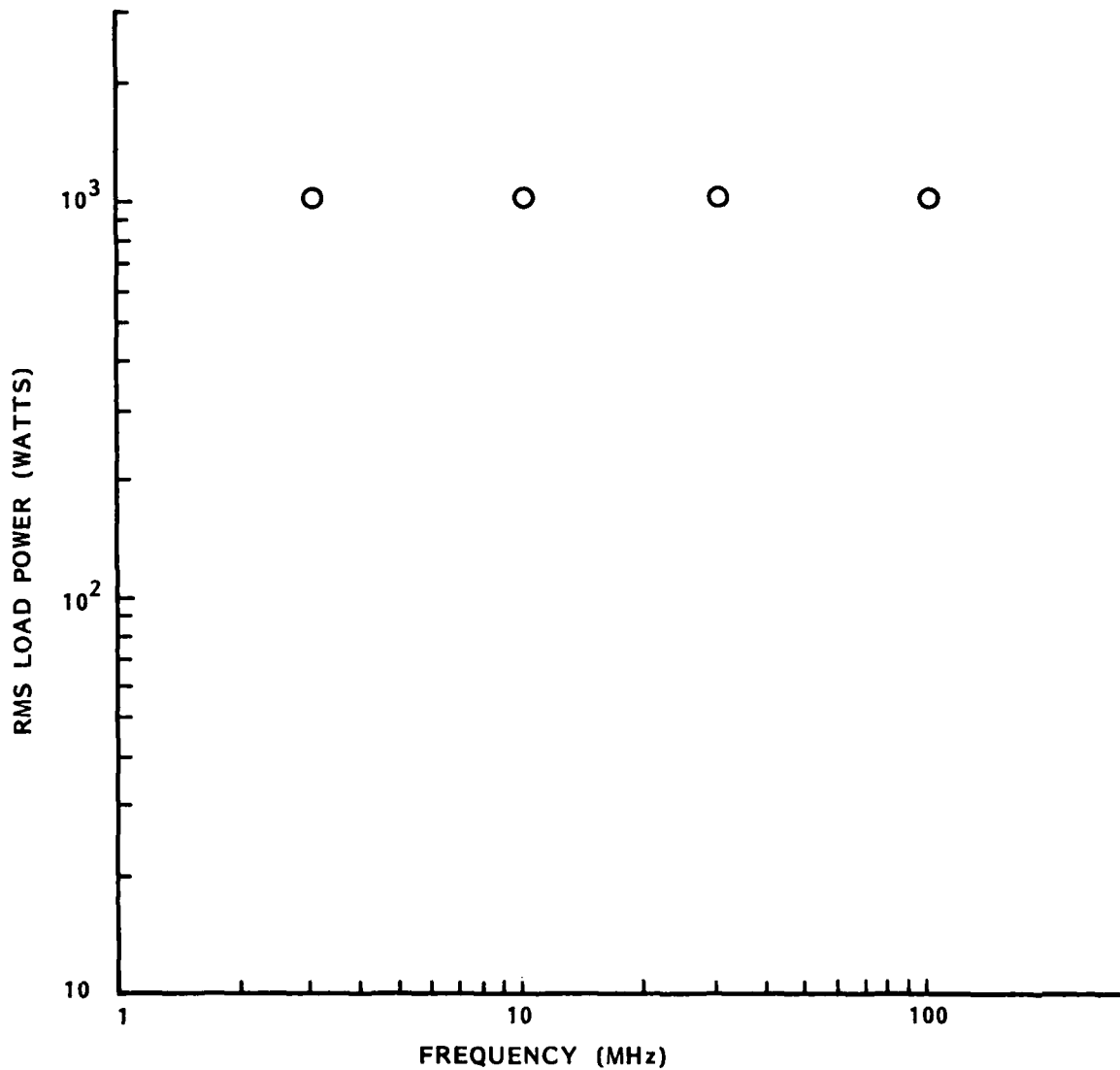
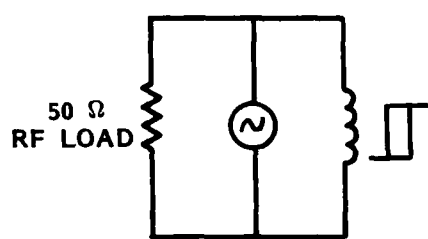


Figure 49. Core loss characteristics - 30 turns on a Ceramic Magnetics Incorporated CMD5005 toroid.



- FREE AIR - NO EFFECT
- FREE AIR - CURIE POINT
- △ ICE WATER - NO EFFECT
- ▲ ICE WATER - CURIE POINT

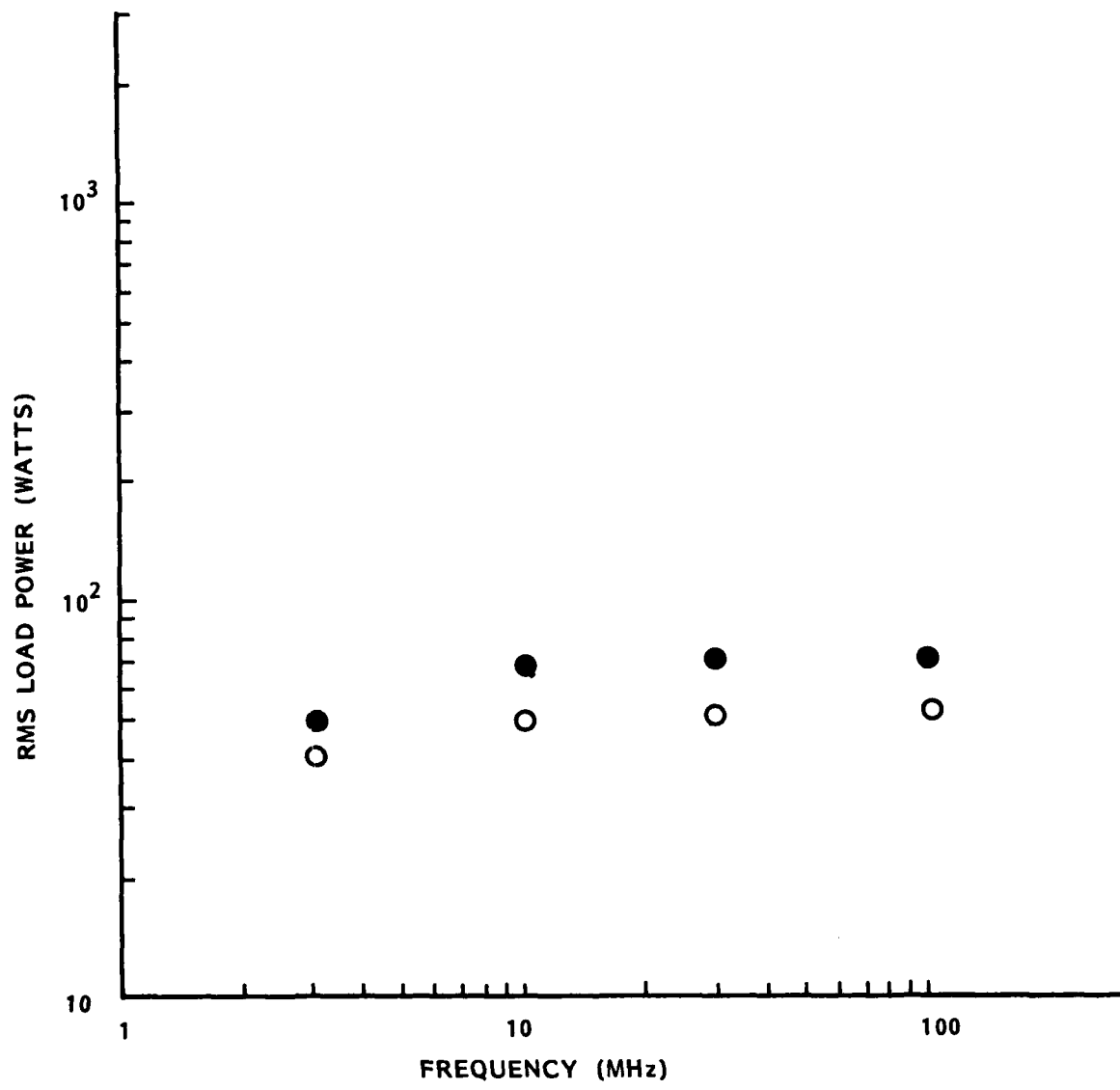


Figure 50. Core loss characteristics - 3 turns on a Ceramic Magnetics Incorporated MN60 toroid.

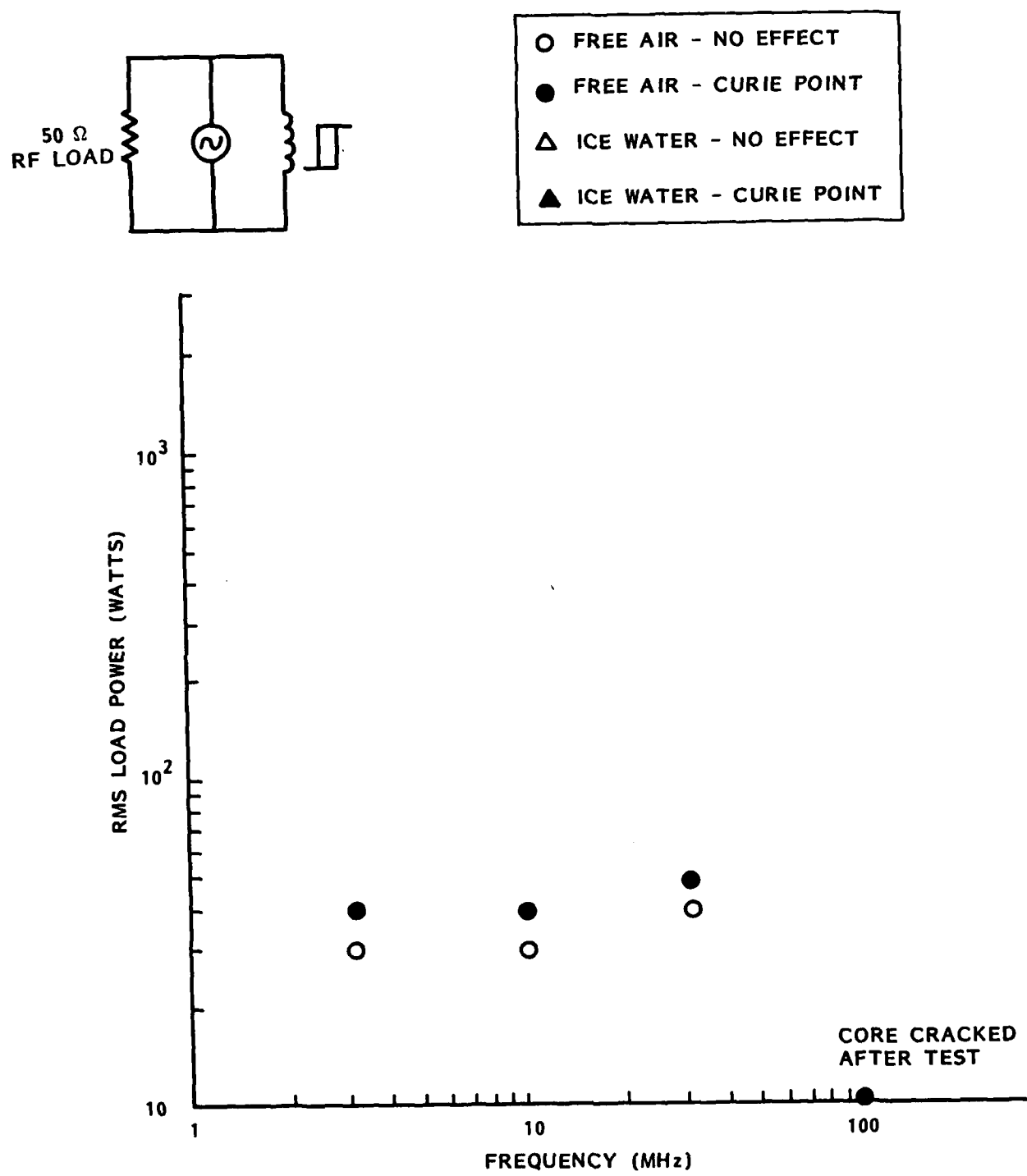


Figure 51. Core loss characteristics - 3 turns on a Ceramic Magnetics Incorporated MN80 toroid.

The approach taken for the present program was to control material self heating by an increase in the device's "NA_C" product, as implied by (4.21), with the full realization that a corresponding increase in "(Vt)_{sat}" would be incurred, as shown by (4.7).

A more serious concern was the minimization of the thermal stresses produced in the toroid structures. Here, it was felt that splitting the toroid structures into half toroid configurations and then reconfiguring them back into toroids using a high temperature, resilient adhesive (i.e., dielectric gapped cores) could be an effective stress reduction design approach. This idea was evaluated by using the same toroid which was cleaved approximately in half during the tests shown in Figure 43. This toroid was reconfigured using RTV, rewound with the same number of turns (3) and retested. These results, which are given in Figure 52, show that the dielectrically gapped unit did not re-incur a thermal fracture and that the advantages of active cooling were still maintained. Figures 53 and 54 show the core loss characteristics obtained using an RTV gapped CMI toroid with three and then eight turns.

4.6 OPTIMIZATION OF THE SATURABLE MAGNETIC DEVICE CONFIGURATION.

For a HESA application "V_{tsat}" is a fixed design point and we may write

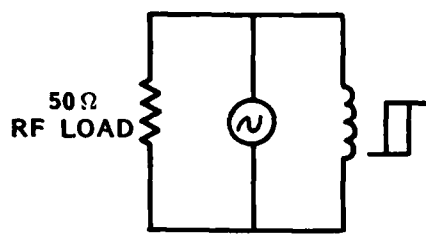
$$(Vt)_{sat} = K_1 \quad (4.22)$$

For a given material type "B_{sat}" is also fixed and, hence, can be written as

$$B_{sat} = K_2 \quad (4.23)$$

As such, (4.7) can be rewritten as

$$N A_C = \frac{10^4 K_1}{K_2} = K_3 \quad (4.24)$$



○	FREE AIR-NO EFFECT
●	FREE AIR-CURIE POINT
△	ICE WATER-NO EFFECT
▲	ICE WATER-CURIE POINT

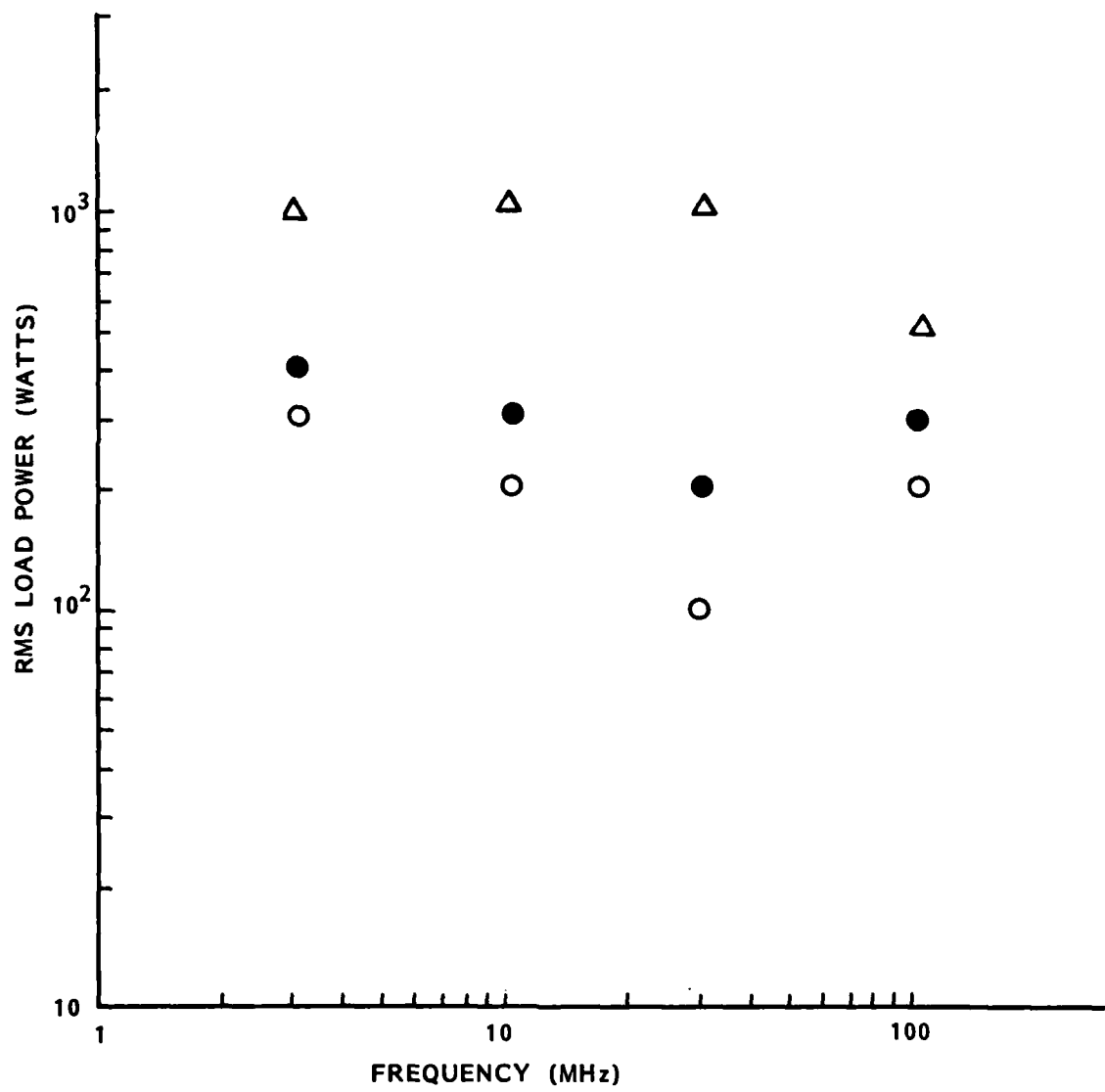


Figure 52. Core loss characteristics of the Figure 43 device after reconfiguring back to toroid form with a 10 mil total RTV gap.

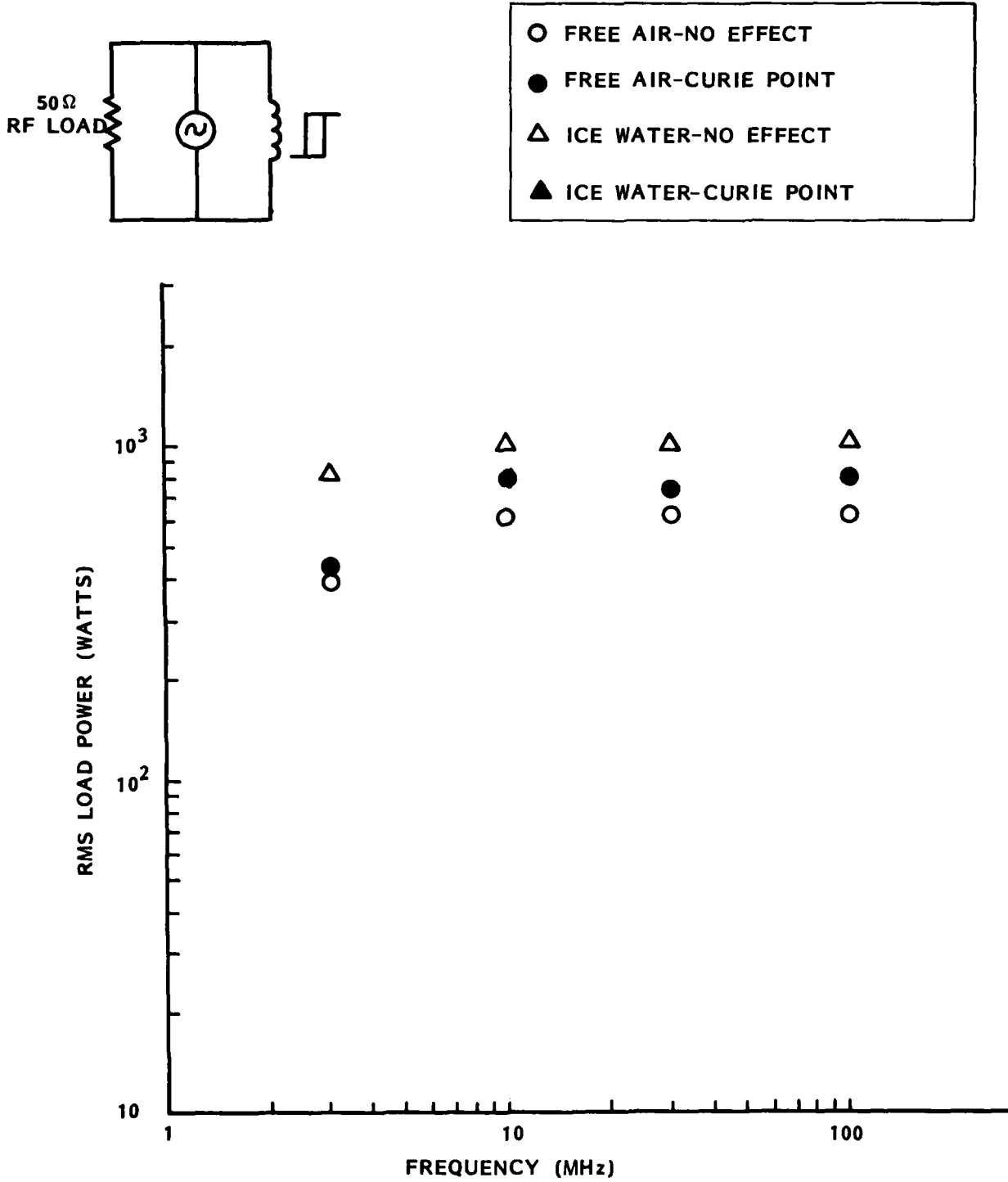
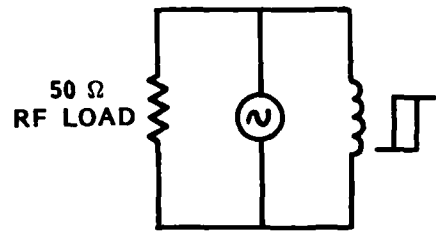


Figure 53. Core loss characteristics - 3 turns on a Ceramic Magnetics Incorporated CMD5005/84-17-3 toroid with a 10 mil RTV gap.



- FREE AIR-NO EFFECT
- FREE AIR-CURIE POINT
- △ ICE WATER-NO EFFECT
- ▲ ICE WATER-CURIE POINT

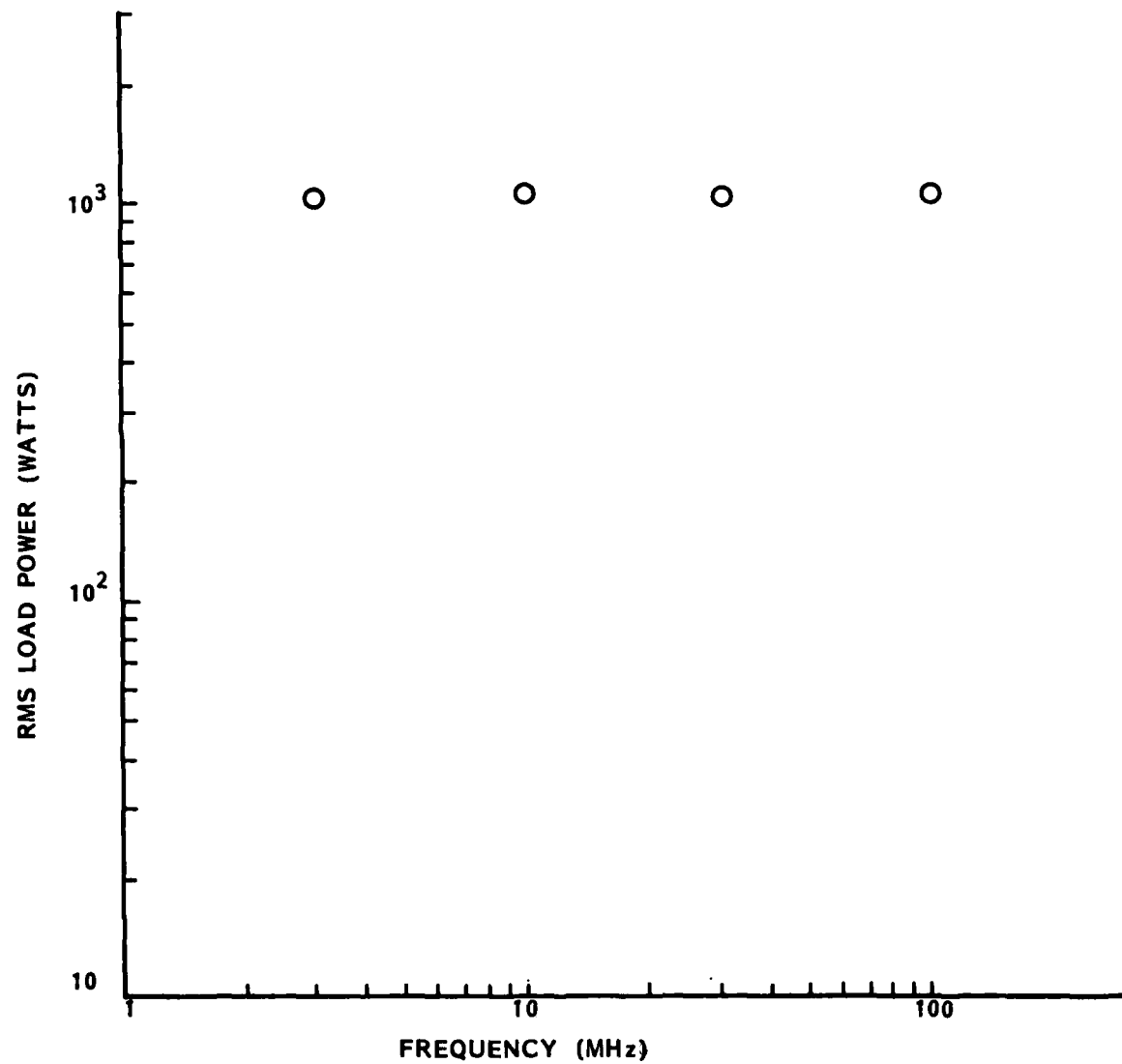


Figure 54. Core loss characteristics - 8 turns on a Ceramic Magnetics Incorporated CMD5005/84-17-3 toroid with a 10 mil RTV gap.

For a given RF transmitter power level and operating frequency

$$\begin{aligned} V &= \text{Fixed} = K_4 \\ f &= \text{Fixed} = K_5 \end{aligned} \quad (4.25)$$

therefore (4.20) can be written as

$$B_0 = \frac{10^4 K_4}{2\pi K_5 K_3} = K_6 \quad (4.26)$$

and, hence, (4.18) can be expressed as

$$P_V = a (K_6)^b \quad (4.27)$$

Therefore, for the saturable magnetic device the loss per unit volume of magnetic material for the HESA application is independent of core geometry and the number of turns. As such, the optimum design configuration would be one in which the heat transfer to the surrounding medium is maximized and one in which the thermal stresses are minimized in the magnetic material.

For the HESA application minimal transfer time for current to be transferred from the varistor device to the saturated inductor is obtained by minimizing L_S . Since L_S is related to L_U we can examine L_U for guidance. Recalling (4.2)

$$L_U = \frac{\mu_0 \mu_R N^2 A_C}{l_c} \quad (4.2)$$

Since for the HESA application

$$N A_C = K_3 \quad (4.24)$$

(4.2) can then be written as

$$L_U = \frac{\mu_0 \mu_R K_3 N}{l_c} = \frac{K_7 N}{l_c} \quad (4.28)$$

Therefore minimum L_u is obtained by minimizing N and maximizing I_C , down to the limits, of course, of minimum L_u for insertion loss considerations. Hence, the indication is to go to a coaxial (i.e., single turn) configuration.

Consider now the coaxial configuration shown in Figure 55. The unsaturated inductance for such a configuration is given by Kraus (Reference 4.1) as

$$L_u = \frac{\mu_0 \mu_R}{2\pi} S \ln \left(\frac{b}{a} \right) \quad (4.29)$$

and the operating flux density at a radius "r" into the material for a current I through the center of the material is given in MKS units by

$$B_0 = \frac{10^4 \mu_0 \mu_R I}{2\pi r} \quad (4.30)$$

For a thin walled coaxial core such that

$$\frac{b - a}{b} \sim \frac{b - a}{a} \ll 1 \quad (4.31)$$

then

$$r \sim \frac{b + a}{2} \quad (4.32)$$

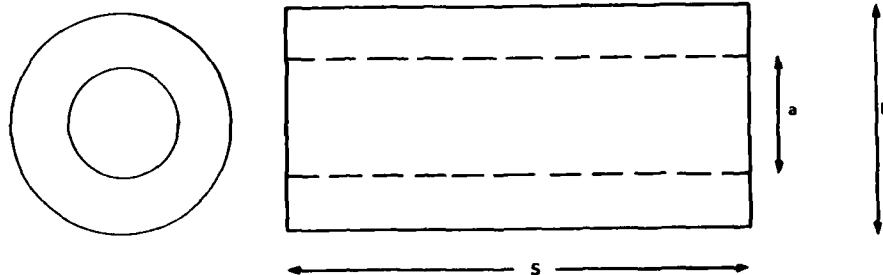


Figure 55. Coaxial geometry of magnetic material.

and (4.30) can be approximated by

$$I \sim \frac{10^{-4} (b + a) B_0}{\mu_0 \mu R} \quad (4.33)$$

For a square wave voltage of amplitude "V" and pulse width "t" which is much greater than the transit time through the coaxial assembly, (4.5) holds and, considering (4.29) and (4.33), we can write

$$(Vt) \sim 10^{-4} \frac{(b + a)}{2} S B_0 \ln(b/a) \quad (4.34)$$

and magnetic material saturation is reached when

$$(Vt)_{sat} \sim 10^{-4} \frac{(b + a)}{2} S B_{sat} \ln(b/a) \quad (4.35)$$

Recalling that

$$\ln X \sim 2 \left(\frac{X - 1}{X + 1} \right) \quad (4.36)$$

$$\text{for } X = 1 + \Delta \\ \text{and } \Delta \sim 0$$

then, for the thin walled coaxial core

$$\ln(b/a) \sim 2 \left(\frac{b - a}{b + a} \right) \quad (4.37)$$

Hence, (4.3.4) can be expressed as

$$(Vt)_{sat} \sim \frac{10^{-4} (b + a) 2 (b - a) S B_{sat}}{2 (b + a)} \quad (4.38)$$

$$(Vt)_{sat} \sim 10^{-4} (b - a) S B_{sat} \quad (4.39)$$

Note that (4.29) can be rewritten, considering (4.37), as

$$L_u \sim \frac{\mu_0 \mu_R}{\pi} S \frac{(b - a)}{(b + a)} \quad (4.40)$$

Now let us examine the relationship of core losses for Curie temperature effects between an "N" turn toroid and a coaxial core. The equivalence that we are seeking is based on dissipating, at CW conditions, the same power per unit volume " P_V " in the toroid as in the coaxial core when the coaxial core is designed for a particular " $(V_t)_{sat}$ ". First considering (4.32) we will rewrite (4.30) as

$$B_0 \sim \frac{10^4 \mu_0 \mu_R I}{\pi (b + a)} \quad (4.41)$$

Now, at CW conditions (4.19) holds

$$I = \frac{V}{2\pi f L} \quad (4.19)$$

and, using (4.40) we can write

$$I \sim \left(\frac{V}{2\pi f} \right) \frac{\pi (b + a)}{\mu_0 \mu_R S (b - a)} \quad (4.42)$$

Substituting (4.42) into (4.41) yields

$$B_{coax} \sim \frac{10^4 V}{2\pi f S (b - a)} \quad (4.43)$$

A similar relationship can be developed for an "N" turn toroid using (4.19), (4.1), and (4.2) such that

$$B_{toroid} = \frac{10^4 V}{2\pi f N A_c} \quad (4.44)$$

Recalling that (4.18) indicated that " P_V " is only dependent on " B_0 ," we can then equate (4.43) to (4.44) to establish the same value of " P_V " in both configurations. Doing this yields

$$N A_C = S(b - a) \quad (4.45)$$

From the toroid shown in Figure 20.

$$A_C = (r_o - r_i) h \quad (4.46)$$

If the coaxial assembly is made up of a number of toroids stacked one upon another (i.e., " $r_o = b$ " and " $r_i = a$ " and $h < S$), then

$$A_C = (b - a) h \quad (4.47)$$

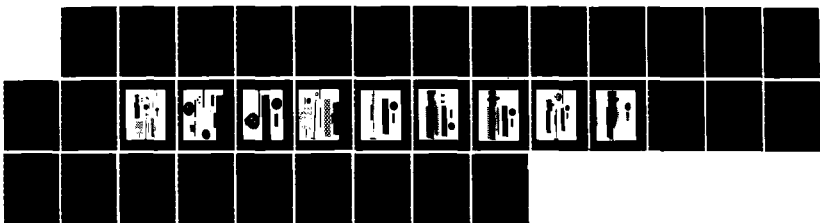
and

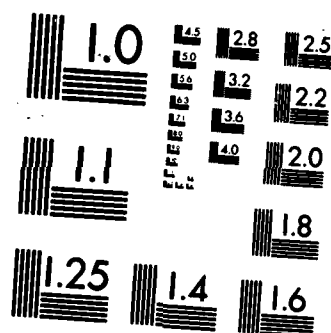
$$N = \frac{S}{h} \quad (4.48)$$

Equation (4.48) states that if "N" turns are wrapped around a toroid of thickness "h" the power per unit volume dissipated in the magnetic material will be the same as for "Nh" of those toroids configured in a coaxial assembly. Note that the equivalence is based on a power per unit volume basis. More total power is lost in the coaxial assembly than in the toroid configuration. The coaxial assembly, however, provides the configuration which provides the fastest time to transfer current from the varistor assembly to the saturated magnetic assembly.

Equation (4.48) also provides a convenient way of evaluating the CW temperature stability of any proposed coaxial configuration. Instead of fabricating costly and involved CW fixtures and assemblies, one can take a toroid version of the proposed geometry and experimentally perform a parametric evaluation of stability versus number of turns to establish the minimum stable coaxial assembly length for a given transmitter power level and operating frequency.

AD-A173 886 HIGH ENERGY SURGE ARRESTER TECHNOLOGY DEVELOPMENT PART
2(U) GENERAL ELECTRIC CO PHILADELPHIA PA SPACE SYSTEMS
DIV D M TRSCA 28 FEB 86 86SD54239 DNA-TR-86-85-PT-2
UNCLASSIFIED DNA001-82-C-0241 F/G 9/1 2/2 NL





MICROCOPY RESOLUTION TEST CHART
NATIONAL BUREAU OF STANDARDS-1963-A

Table 3 shows the results of one such thermal stability parametric test performed on toroids in support of the prototype design activities described in Section 5. The tests were designed to evaluate the thermal stability of various dielectric gap thicknesses in a particular CMI core type as a function of toroid turns when the toroids were placed across the output of an RF transmitter operating at 30 MHz and 1 Kilowatt RMS load power. The data shows the experimentally observed times to reach the Curie point for a number of turn/gap combinations. As seen, a minimum of 20 turns for cores with 20 and 30 mil gaps was required before thermal stability was established at the 30 MHz/1 KW conditions.

The final consideration for the coaxial assembly is that associated with the frequency-length constraints in order for the assembly to be considered as a lumped element for HESA response purposes. At high frequencies the coaxial assembly starts to behave as a short length of transmissions line terminated in a short circuit. The input impedance "Z_{in}" for a loss-less or low-loss transmissions line of length "S" terminated in a short circuit is given by (Reference 4.2)

$$Z_{in} = j \sqrt{\frac{L}{C}} \tan (\beta S) \quad (4.49)$$

where

$$\beta = 2\pi f \sqrt{LC} \quad (4.50)$$

and L and C are the inductance per unit length and capacitance per unit length respectively of the transmission line. The quantity " β " is the phase shift constant and can also be expressed in terms of " μ_R " and " ϵ_R " in MKS units as

$$\beta = \frac{2\pi f \sqrt{\mu_R \epsilon_R}}{3 \times 10^8} \quad (4.51)$$

For small values of "S"

$$\tan \beta S \sim \beta S \quad (4.52)$$

Table 3. Thermal stability test results for Ceramic Magnetics Incorporated dielectrically gapped CMD5005 toroids ($a = 1.27$ cm, $b = 2.72$ cm, $S = 0.889$ cm).

CORE SAMPLE S/N	CONFIGURATION		TIME TO REACH CURIE POINT FOR A CW LOAD OF 1 KW RMS @ 30 MHz
	GAP (MILS)	TURNS	
1	6	7	<1 MIN
		10	>2 MIN
		14	>5 MIN
		20	>25 MIN
2	20	7	<1 MIN
		14	8 MIN
		20	OK @ 30 MIN
3	20	20	OK @ 30 MIN
4	20	20	OK @ 30 MIN
5	30	14	11 MIN
		20	OK @ 30 MIN

and (4.49) can be written as

$$Z_{in} \sim j 2\pi f L S \quad (4.53)$$

Noting that

$$L S = L_u \quad (4.54)$$

we can see that the input impedance of the coaxial assembly will be that corresponding to a lumped element for small values of "S". A maximum error of 10% results when " $\beta S = 0.5$ radians." As such, an acceptable criteria for the HESA would be to limit " βS " to

$$\beta S \leq 0.5 \quad (4.55)$$

which results in one such limit on "S" of

$$S \leq \frac{3 \times 10^8}{4\pi f \sqrt{\mu_R \epsilon_R}} \text{ METERS} \quad (4.56)$$

However a less stringent limit on "S" would be based on restricting operation to below the point at which the transmission line assembly transitions from an inductive to a capacitive load. This occurs at quarter wave length, i.e.,

$$\beta S = \frac{\pi}{2} \quad (4.57)$$

Here "S" is controlled by

$$S < \frac{3 \times 10^8}{4f \sqrt{\mu_R \epsilon_R}} \quad (4.58)$$

SECTION 5

PROTOTYPE DESIGN

The design requirements for the proof-of-concept prototype HESA were defined in Section 2 and are repeated below:

Application

- 50 ohm RF Transmitter
- 2 kW peak power (1 kW RMS)
- 2-30 MHz operating frequency, with a 100 MHz upper limit goal

Threat

- 600 KV open circuit voltage
- 10 KA short circuit current
- 30 ns rise time
- 2 ms pulse width
- 5 pulses, 1 second apart

HESA Requirements

- clamp line to \leq 900 volts
- self recover
- insertion loss \leq 2 db

Since an optimization of the geometrical and material properties of the HESA elements were well beyond the scope of the present program, the baseline approach selected for the proof-of-principle prototype was to use an upper limit frequency of 30 MHz for all design aspects where a higher frequency would impact the HESA design achievable with the existing materials in hand.

5.1 SATURABLE MAGNETICS DESIGN.

The design of the saturable magnetics element was based on stacking "N_T" gapped cores of thickness "h" into a coaxial configuration as shown in Figure 56. The cores for the prototype HESA were perfect halves of CMD5005 type material supplied through the courtesy of Ceramic Magnetics Incorporated. The core dimensions were as follows:

$$\begin{aligned} a &= 0.00635 \text{ meters} \\ b &= 0.0136 \text{ meters} \\ h &= 0.00889 \text{ meters} \end{aligned}$$

From Section 4 the limiting design equations in MKS units are

- $(Vt)_{sat} \sim 10^{-4} (b - a) S B_{sat}$ (4.39)

- $\frac{1}{L_u} \leq \frac{4\pi f}{Z_0} \sqrt{10db/10 - 1}$ (4.17)

- $L_c \leq L_u \frac{\mu_0 \mu_R}{\pi} S \left(\frac{b - a}{b + a} \right)$ (4.40)

- $S \leq \frac{3 \times 10^8}{4f \sqrt{\mu_R \epsilon_R}}$ (4.58)

- Core Loss < P_y to reach Curie Temperature

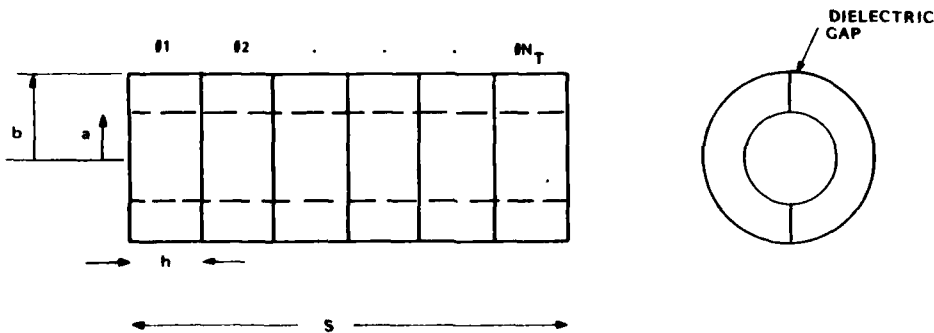


Figure 56. Coaxial configuration of the saturable magnetics element of the prototype HESA.

For the HESA application the magnetic element must be capable of holding-off the maximum "Vt" product imposed by the RF transmitter without switching into saturation. Maximum "Vt" product occurs at the lowest frequency, i.e., 2 MHz. Recalling that the average voltage value "V_{avg}" of a sine wave of peak value "V_p" is given by

$$V_{\text{avg}} = \frac{2 V_p}{\pi} \quad (5.1)$$

then we can write the "(Vt)" product for a half cycle of a 2 MHz sine wave as

$$(Vt) = \frac{2 V_p}{\pi} (2.5 \times 10^{-7}) \text{ Volt-Sec} \quad (5.2)$$

For a 2 kW peak power in 50 ohms "V_p" corresponds to

$$V_p = 316 \text{ volts} \quad (5.3)$$

therefore

$$(Vt) = 5.03 \times 10^{-5} \text{ Volt-Sec} \quad (5.4)$$

Using a design safety factor of "2", then the design point for magnetics switching is

$$(Vt)_{\text{sat}} \geq 10.06 \times 10^{-5} \text{ Volt-Sec} \quad (5.5)$$

For the CMD5005 material

$$B_{\text{sat}} = 3.1 \times 10^3 \text{ gauss} \quad (5.6)$$

Hence, equating (4.39) and (5.5) and solving for "S" using the core dimensions and magnetic properties yields

$$S \geq 0.0448 \text{ meters} \quad (5.7)$$

Laboratory tests described in Section 4 have established that 6 mil, 20 mil and 30 mil gapped cores, whose gaps are fabricated with bond paper saturated with Eastman 910 adhesive, are sufficiently stress relieved to withstand 2 kW peak transmitter power at 30 MHz. These tests (Table 3) have also indicated that the minimal number of turns (on a single toroid of the type used in the prototype HESA) required for thermal stability is 20 turns, but in only a 20 mil gapped core. Smaller and larger gaps required more turns for thermal stability. As such, the 20 mil gapped core was used for the prototype design. Equation (4.48) related the thermal stability equivalence between a coaxial geometry and a multi-turn toroid. For a 20 turn minimum the requirement for "S" is

$$\begin{aligned} S &\geq Nh \\ &\geq 0.178 \text{ meters} \end{aligned} \quad (5.8)$$

The insertion loss caused by the shunt inductor of the HESA increases with decreasing frequency. Hence, for the prototype application where Z_0 is 50 ohms, the limiting value of L_u for a 2 db insertion loss occurs at 2 MHz and is found from 4.17 as

$$L_u \geq 2.6 \times 10^{-6} \text{ henries} \quad (5.9)$$

For the CMD5005 cores with a 20 mil gap, Figure 37 showed that

$$\mu_R = 170 \quad (5.10)$$

and, since $\mu_0 = 4\pi \times 10^{-7}$ henries/meter in MKS units, then one limit on "S" is found from (4.40) as

$$S \geq 0.105 \text{ meters} \quad (5.11)$$

The limiting value of "S" where the change from an inductive element to a capacitive element transitions occurs at the highest frequency of operation for the HESA. Since $\epsilon_R \sim 1$ for the ferrite material, then using a 30 MHz point, (4.58) yields

$$S \leq 0.192 \text{ meters} \quad (5.12)$$

Therefore the allowable range of lengths for the coaxial assembly is found from the set of

$$S \geq 0.0448 \text{ meters for } (Vt)_{sat}$$

$$S \geq 0.178 \text{ meters for CW Thermal Stability}$$

$$\begin{aligned} S &\geq 0.105 \text{ meters} \\ S &\leq 0.192 \text{ meters} \end{aligned} \quad \left. \right\} \text{for } L_C \text{ Requirements}$$

Hence

$$0.178 \text{ meters} \leq S \leq 0.192 \text{ meters} \quad (5.13)$$

Now, since

$$h = 0.00889 \text{ meters}$$

Then, the number of cores " N_T " required for the coaxial assembly is

$$20 \leq N_T \leq 22 \quad (5.14)$$

Taking a design value of " $N_T = 20$ " cores for the coaxial assembly yields the following. From (4.39)

$$(Vt)_{sat} = 400 \times 10^{-6} \text{ Volt-Sec} \quad (5.15)$$

and from (4.40)

$$L_u = 4.4 \times 10^{-6} \text{ henries} \quad (5.16)$$

$$L_{sat} = 2.6 \times 10^{-8} \text{ henries} \quad (5.17)$$

5.2 METAL OXIDE VARISTOR DESIGN.

A 2 kW peak power level for the 50 ohms transmitter corresponds to a peak value of 316 volts. The X531 GE-MOV® Varistor has a 1 mAmp DC varistor voltage of 350 volts. This yields an "off-to-on" safety factor of 1.107 which is acceptable for the proof-of-principle design, but would be increased for an operational HESA. The CW/RF tests described in Section 3 have shown that series/parallel strings of Unitrode IN5811 diodes can be connected in series with the X531 device and placed across a 1 kW RMS transmitter at 30 MHz in ambient and survive (Table 1). However, from Section 3.5 it was shown that the total reverse breakdown voltage capability of the diode string " V_{TR} " must be greater than " $2 V_p$ ". Since the diode string is made up of " N_D " diodes in series, each with a minimum breakdown voltage of " V_R ", we can write

$$N_D V_R > 2 V_p \quad (5.18)$$

If we select diodes based on a " $V_R \geq 150$ volt" criterion then, since " $V_p = 316$ volts", we find the minimum value of N_D as

$$N_D > 4.2 \quad (5.19)$$

Hence, the diode string was selected to consist of five in series for the prototype.

In Section 3.5 it was identified that an optimization of diode junction area and package configuration was beyond the scope of our program. It was pointed out, though, that proof-of-concept could be more than adequately demonstrated using 1N5811 diodes in axial lead packages. However, in

order to obtain a higher forward current rating for demonstration purposes, individual diodes would be paralleled. Hence, in order to achieve CW thermal stability the baseline design selected for the prototype was to use a "5 series X 2 parallel" string of 1N5811 diodes in axial lead packages in series with an X531 varistor.

The insertion loss caused by the shunt capacitance of the diode/varistor combination increases with increasing frequency. Hence, for the prototype application where Z_0 is 50 ohms, the limiting value of capacitance " C_C " for a 2 db insertion loss occurs at 30 MHz and is found from 3.5 as

$$C_C \leq 1.62 \times 10^{-10} \text{ farads} \quad (5.20)$$

Figure 14 shows that the prototype HESA contains back-to-back diode/varistor strings. For a single string the equivalent capacitance circuit for the diode/varistor configuration is shown in Figure 57. Total capacitance " C_T " consists of two of the Figure 57 strings in parallel and is given by

$$C_T = \frac{4 C_D C_M}{2 C_D + 5 C_M} \quad (5.21)$$

Since the diode capacitance " C_C " decreases with increasing reverse voltage due to depletion width widening, maximum capacitance occurs at low voltages. For the IN5811 diode the experimental data given in Figure 17 indicates that the low voltage diode capacitance is

$$C_D = 29 \text{ picofarads} \quad (5.22)$$

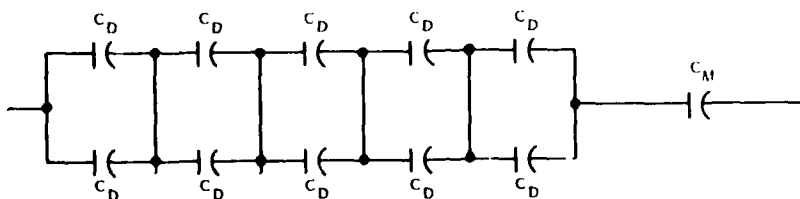


Figure 57. Equivalent capacitance circuit for each of the two diode/varistor strings used in the prototype HESA.

The GE-MOV® varistor exhibits a much smaller (~ 20%) but similar decrease of device capacitance with applied voltage (Reference 5.1). The experimental data shown in Figure 9 for the X531 device indicates a low voltage capacitance of

$$C_M = 660 \text{ pf} \quad (5.23)$$

Hence, the total capacitance of the diode/varistor assembly from (5.21) is

$$C_T = 22.8 \text{ pf} \quad (5.24)$$

Note that C_T is now controlled by the diode string capacitance. The significance of this is that a much larger area varistor can be used in an optimized design, resulting in lower clamping voltages. Since for the prototype design

$$C_T \ll C_C \quad (5.25)$$

and since the diode string was implemented in axial lead rather than chip form, it was qualitatively determined to counter this additional lead inductance by introducing a shunt capacitor of value "C_S" such that

$$C_S + C_T = C_C \quad (5.26)$$

or

$$C_S \leq 139 \text{ pf} \quad (5.27)$$

For a 10 Kilo-ampere threat the forward current through each of the parallel diodes is 5 Kilo-amperes. From Figure 16 the diode forward voltage drop " V_{DF} " at this current is

$$V_{DF} < 20 \text{ volts} \quad (5.28)$$

and the total voltage drop "V_{TF}" across the 5 diode string is

$$V_{TF} < 100 \text{ volts} \quad (5.29)$$

From Figure 7 the varistor voltage "V_M" at 10 Kilo-amperes is

$$V_M \sim 1100 \text{ volts} \quad (5.30)$$

Hence, the total clamping voltage is given by

$$V_{\text{clamp}} \sim 1200 \text{ volts} \quad (5.31)$$

Note again that the use of the diode string allows a much larger varistor area to be implemented in an optimized design, which would easily meet the 900 volt maximum clamping voltage design level.

Another requirement from Section 3.5 is that associated with the high current, forward conducting string reaching a high enough voltage to turn on the companion adjacent string in the reverse direction. The criteria which was given can be stated here as

$$(V_M + V_{TF}) @ \text{High } I < (V_{TR} + V_M) @ \text{Low } I$$

substituting the appropriate values yields

$$(V_M + V_{TF}) @ \text{High } I = 1200 \text{ volts} \quad (5.32)$$

$$(V_{TR} + V_M) @ \text{Low } I = 1100 \text{ volts} \quad (5.33)$$

which shows that the criteria is exceeded by 100 volts at the 10 KA level when using the X531 device. Examining Figure 7 we see that the criteria is met at threat currents of 5 KA or less when using the X531 device. In an optimized design where the varistor area can be quite large, the criteria can readily be met.

The effective resistance "R_E" of the diode/varistor string is given by

$$R_E = \frac{1200 \text{ volts}}{10,000 \text{ Amperes}} = 0.12 \text{ ohms} \quad (5.34)$$

The time required to transfer current from the diode/varistor string to the saturated magnetics element is related to the "L/R" time constant of the HESA. Since clamping voltage is somewhat independent of current level, as current is transferred from the diode/varistor string "R_E" increases and the instantaneous time constant decreases. Hence, the worst case time constant is

$$\tau = \frac{L_S}{R_E @ \text{MAX CURRENT}} \quad (5.35)$$

From (5.17) and (5.34) we obtain

$$\tau = \frac{2.6 \times 10^{-8}}{0.12} = 215 \text{ ns} \quad (5.36)$$

From (5.15) the time to reach magnetics saturation for a 1200 Volt clamping level is

$$t_{\text{sat}} = 333 \text{ ns} \quad (5.37)$$

If we consider that the total transfer of current from the diode/varistor string to the saturated magnetics occurs in "3τ", then the diode/varistor string conducts high current for a time given by

$$t = (t_{\text{sat}} + 3\tau) = 978 \text{ ns} \quad (5.38)$$

Maximum diode forward current rating for safe operation at 1 μs is 2000 amperes which gives a HESA rating for the parallel diode configuration of 4000 amperes and from Figure 18 a GE-MOV® varistor rating of > 10,000 amperes for the X531 device.

5.3 PROTOTYPE CONFIGURATION.

Figure 58 shows the schematic diagram of the prototype HESA which was developed from the preceding design analyses. Figures 59 through 67 are photographs of the prototype fabrication HESA at various levels of assembly. Although high current, high RF power testing of the prototype is to be covered under Phase II of the program, some low level characterization testing was performed in order to establish confidence in the prototype HESA hardware.

Table 4 shows the low level input impedance of the HESA at various stages of assembly. "Configuration 1: saturable magnetics only with open circuit at output" shows that the ferrite cores are slightly lossy (i.e., phase values other than $\pm 90^\circ$) which probably accounts for the observed phase change from inductive to capacitive occurring at 21 MHz as compared to a calculated value of 32 MHz. "Configuration 2" shows the capacitive influence of the diode/varistor string while "Configuration 3" shows the effects of the additional internal capacitors which were added for design conservatism. "Configuration 4" shows the input impedance of the HESA when terminated in 50 ohms. Tables 5 and 6 show the effects of the internal capacitors on the medium power VSWR characteristics of the prototype HESA.

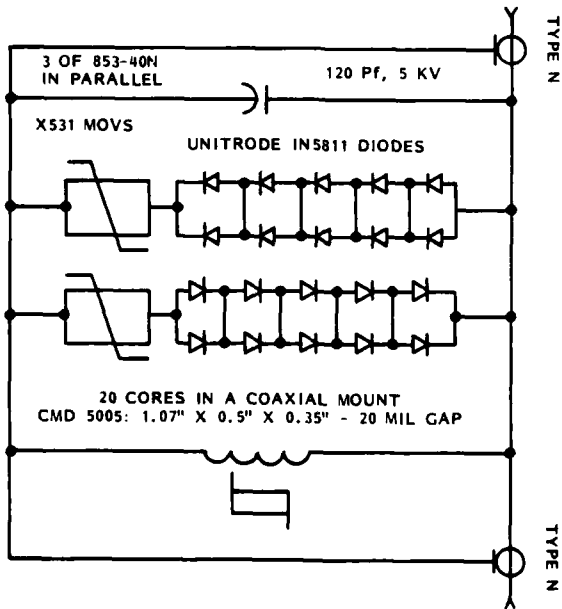


Figure 58. Schematic diagram of the prototype HESA.

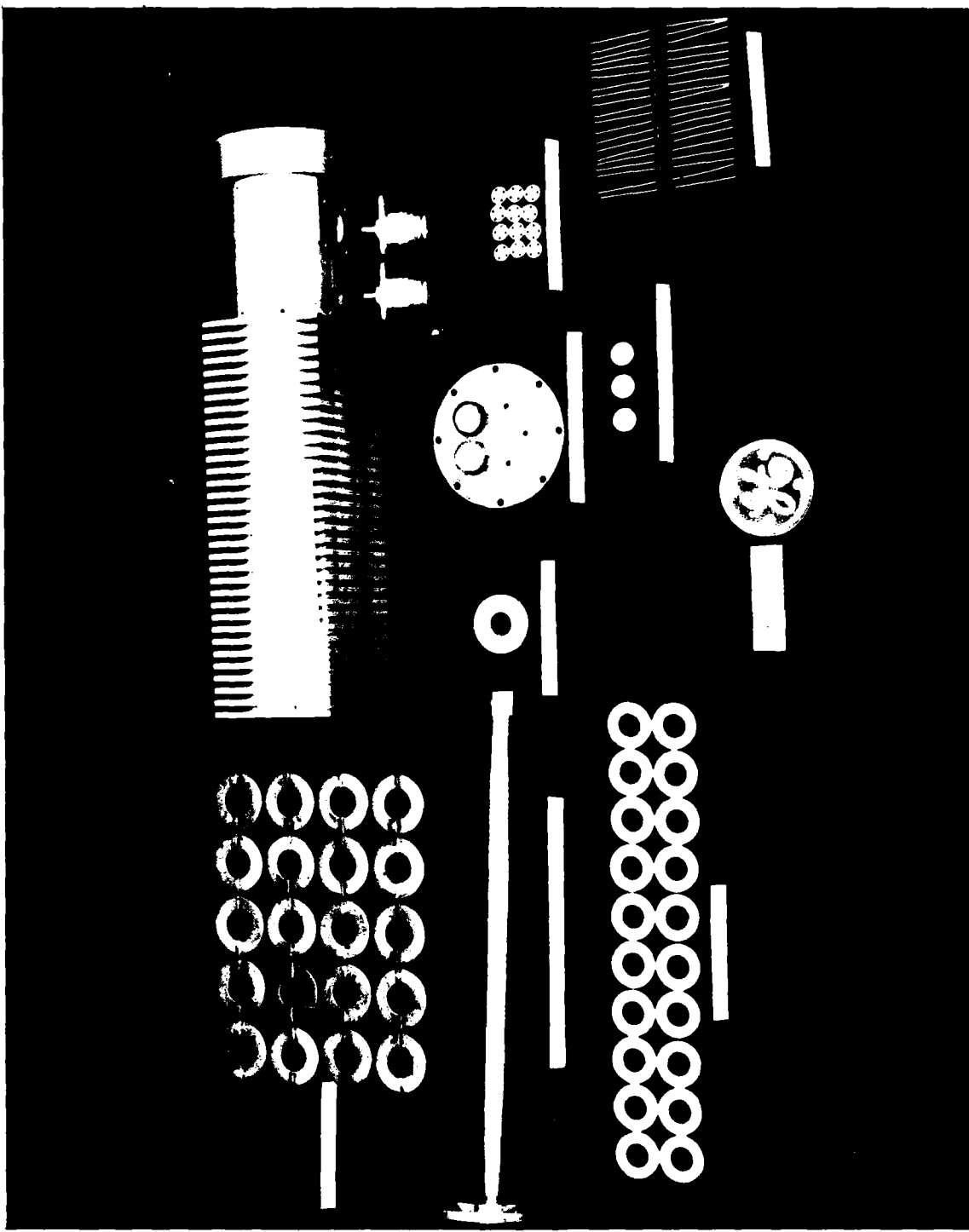


Figure 59. Total parts content of the prototype HESA.

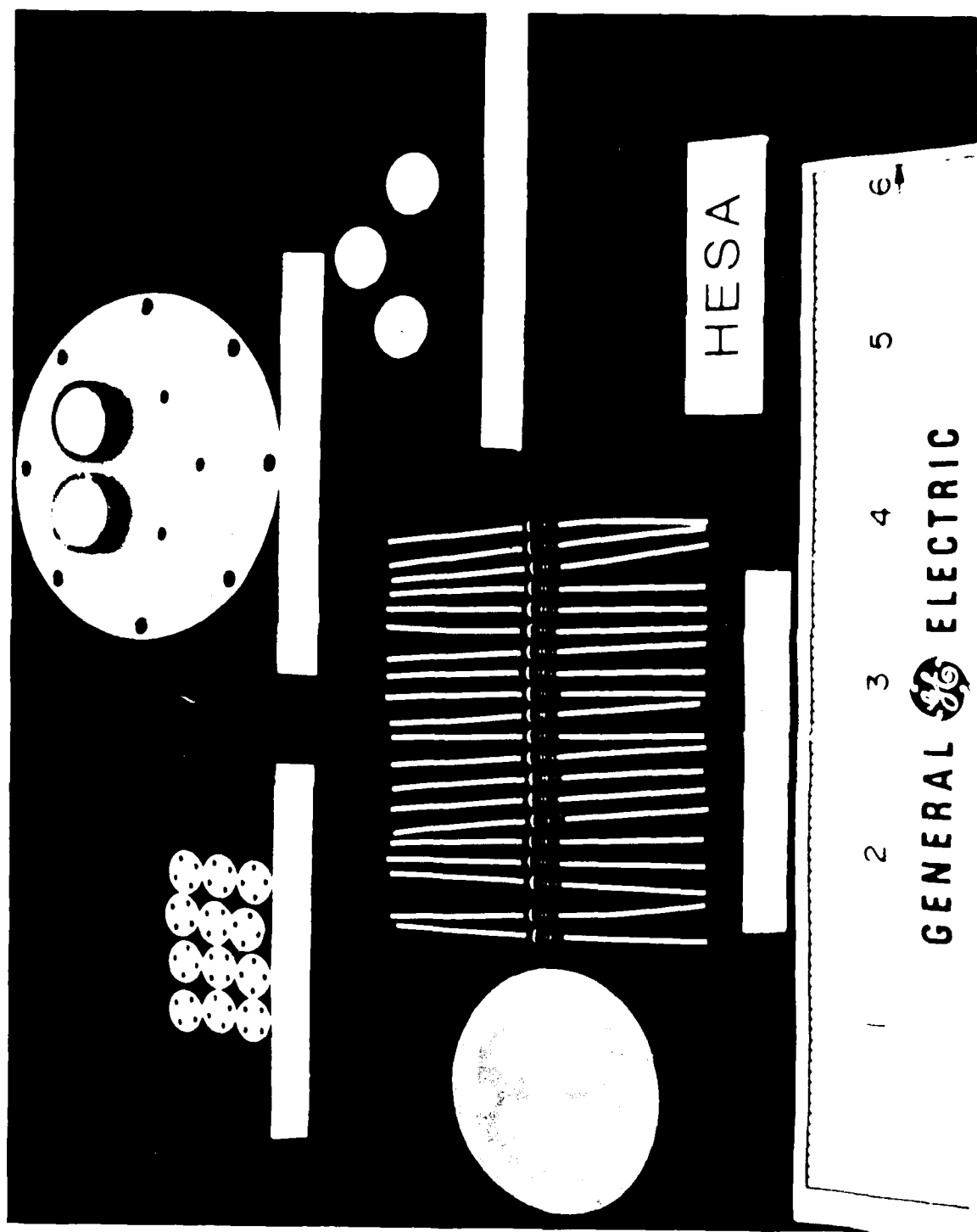


Figure 60. Total parts content of the diode/varistor/capacitor assembly.

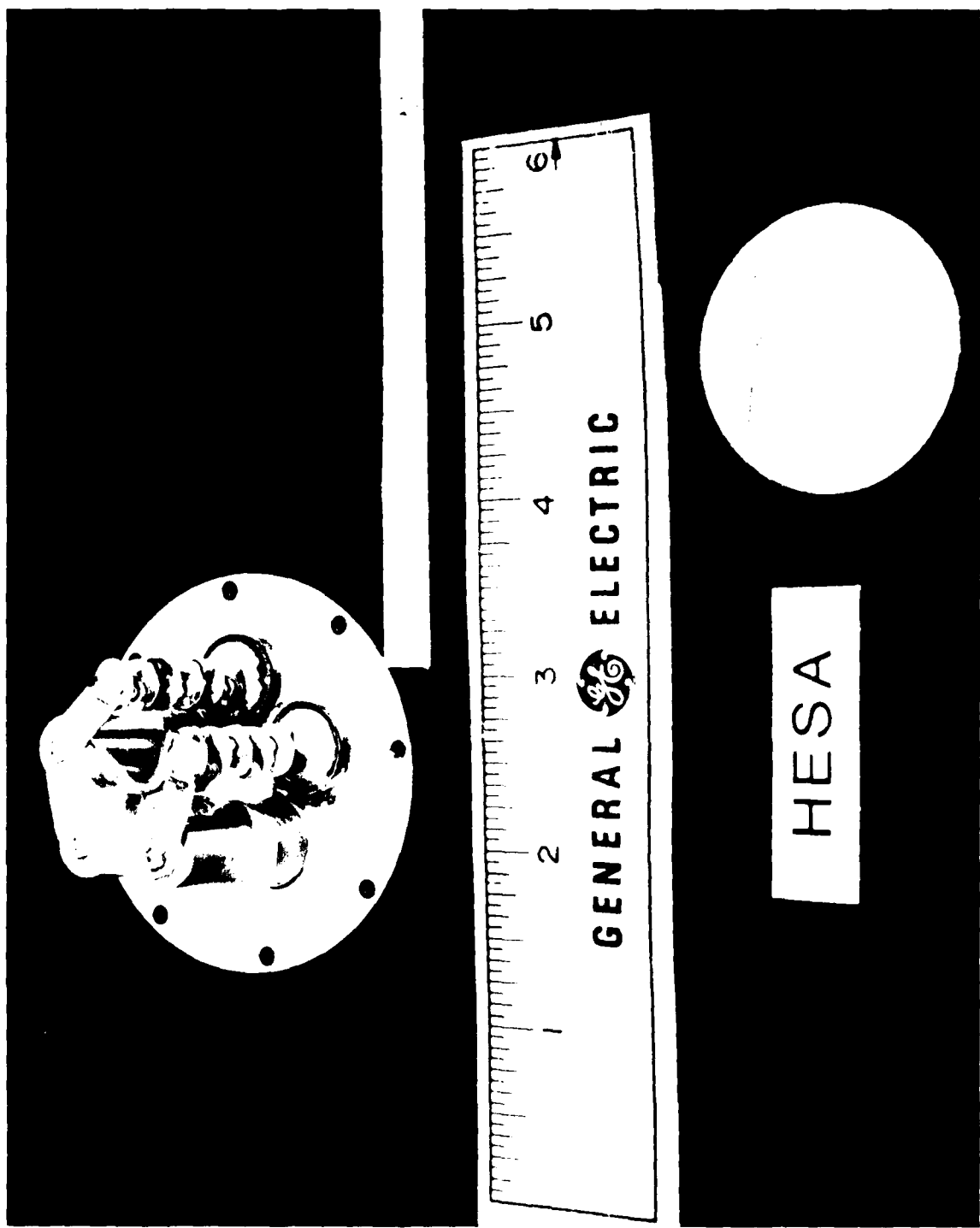


Figure 61. Diode/varistor/capacitor subassembly.

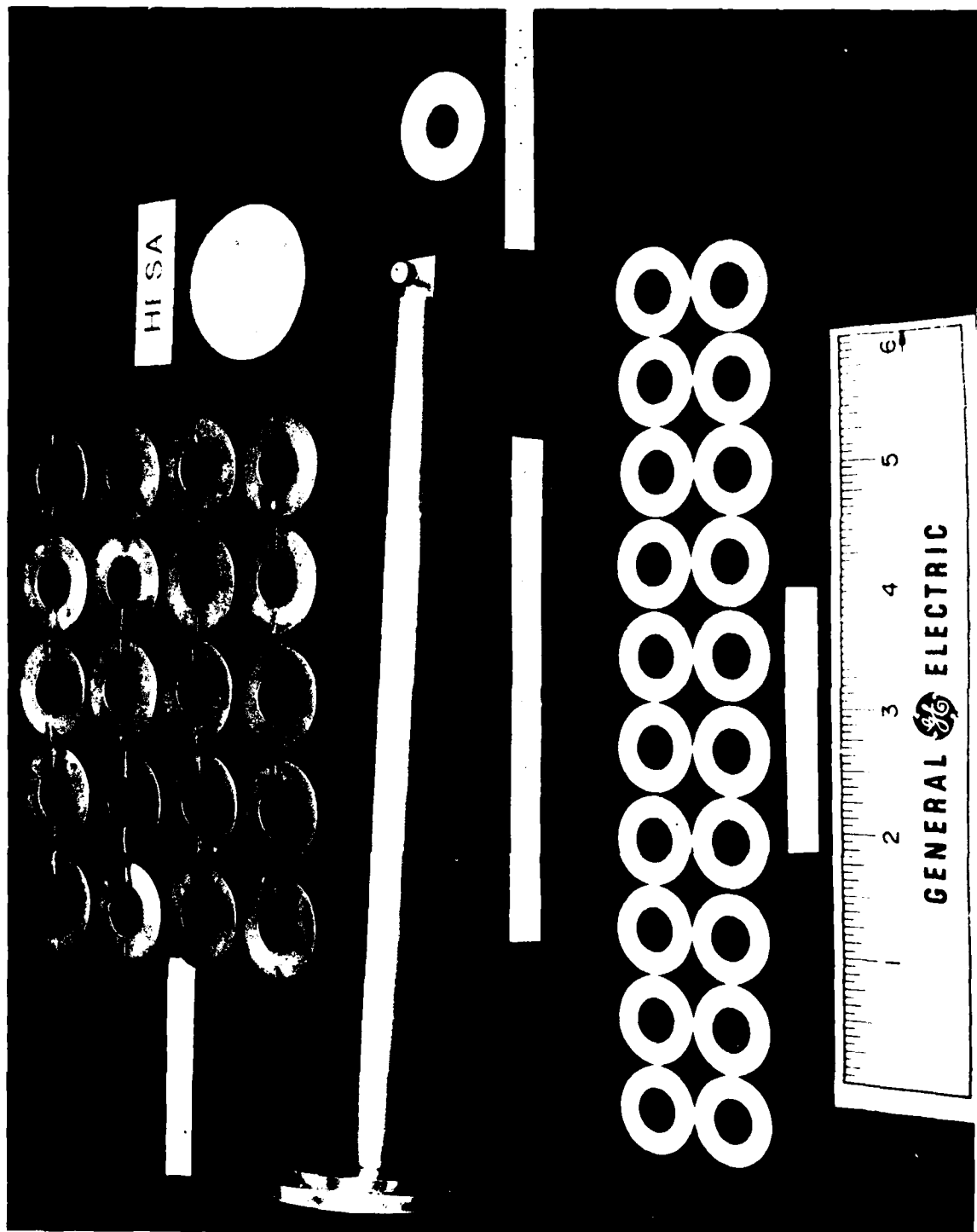


Figure 62. Total parts content of the saturable magnetics subassembly.

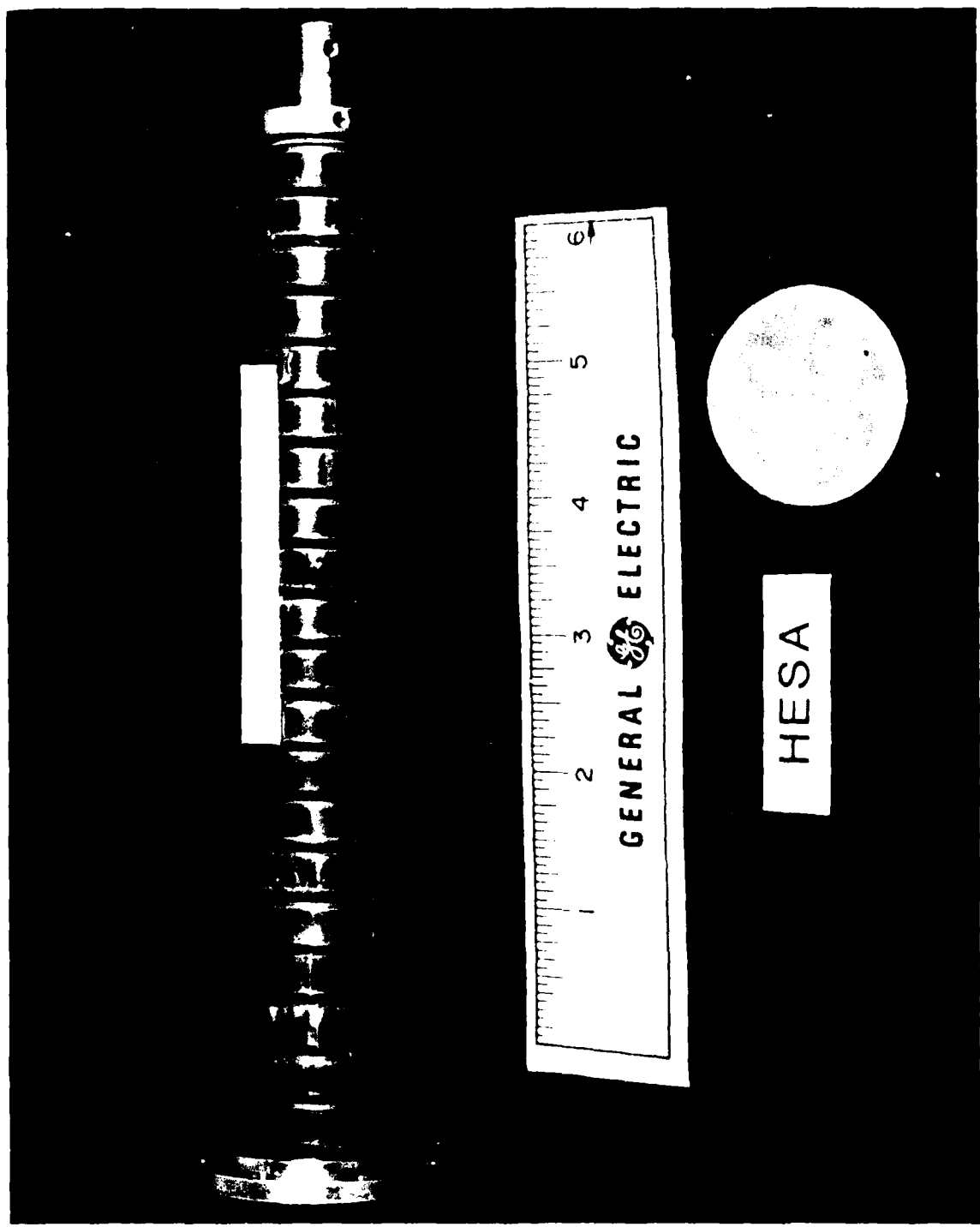


Figure 63. Saturable magnetics subassembly.

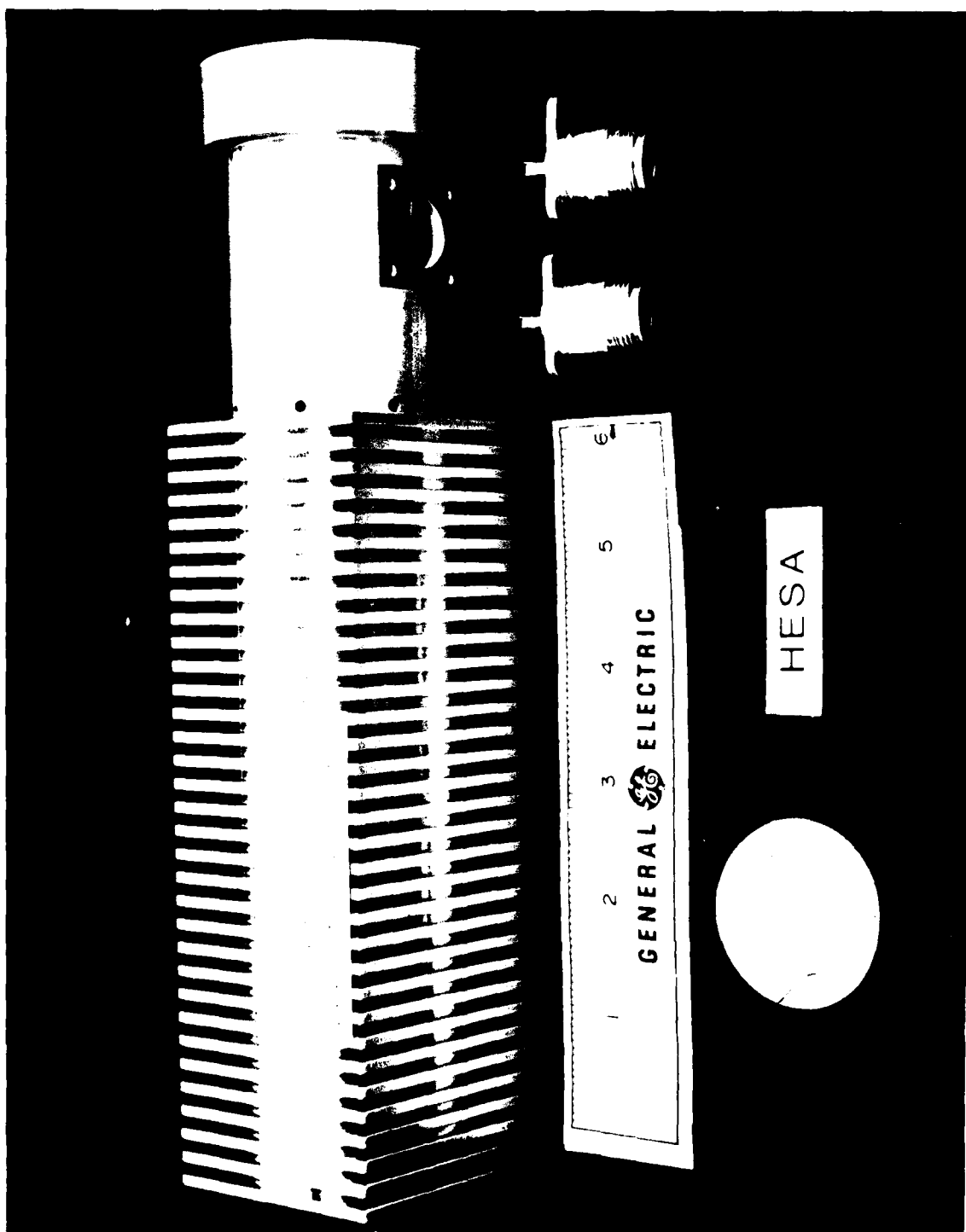


Figure 64. Total parts content of the housing subassembly.

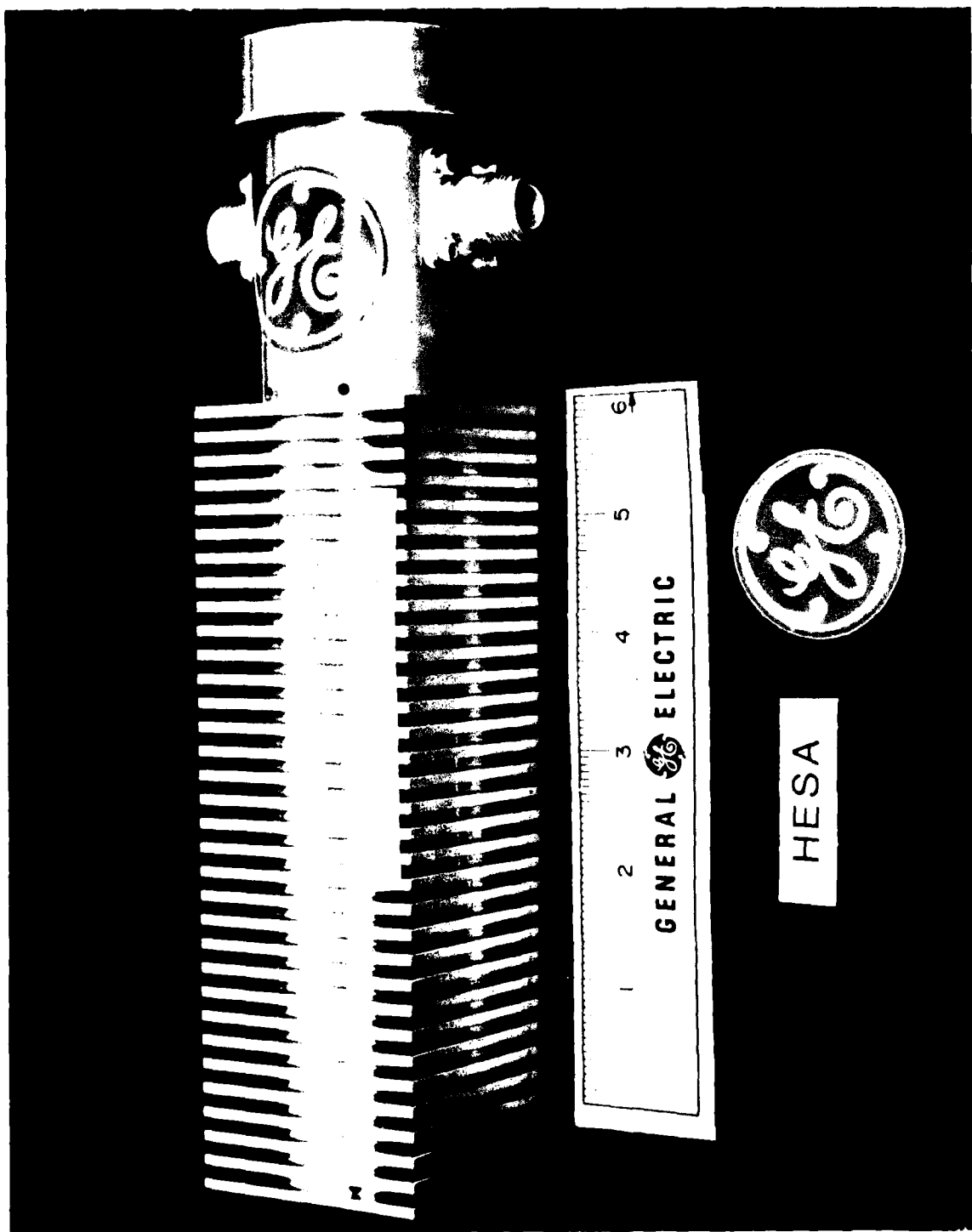


Figure 65. Housing subassembly.

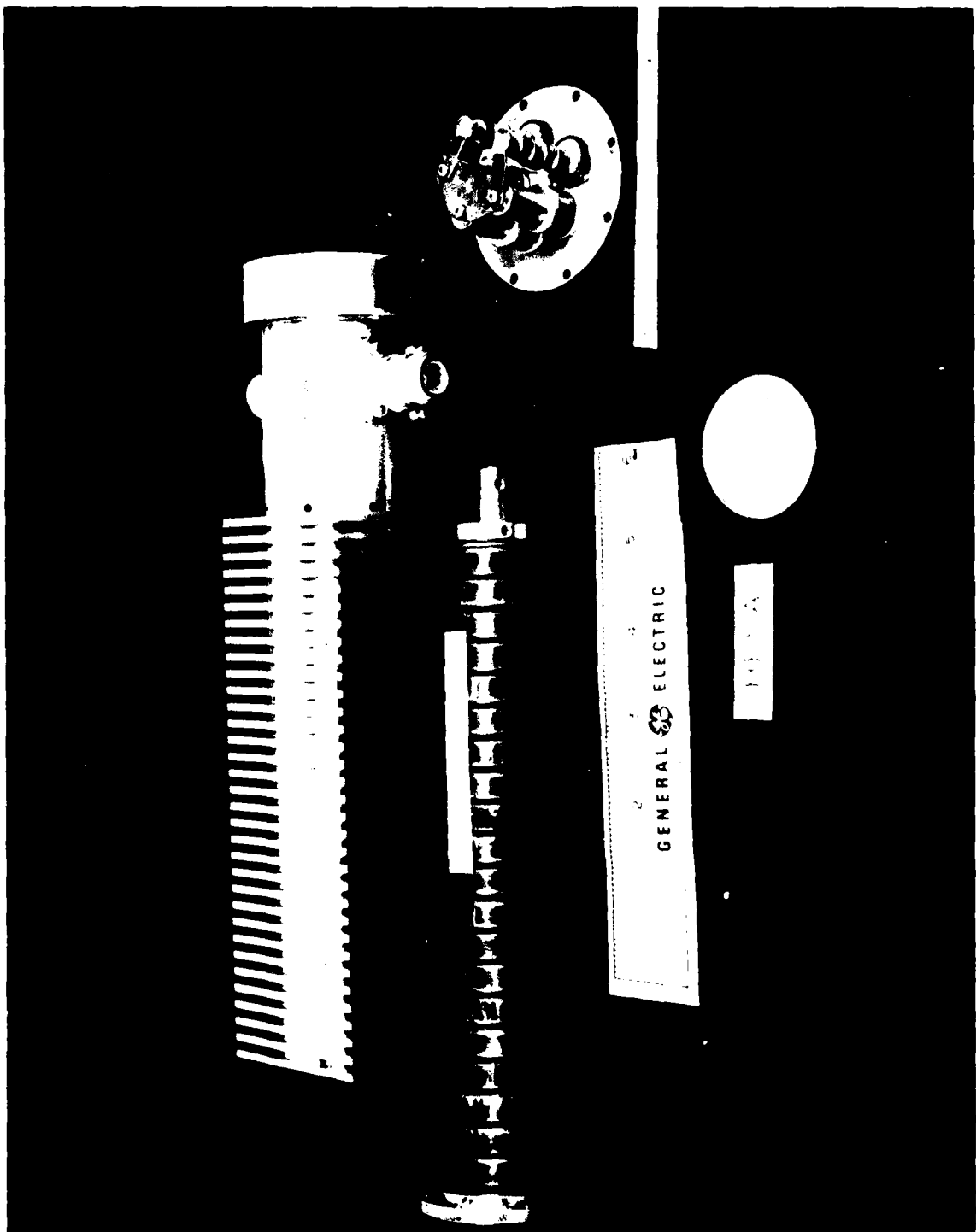


Figure 66. Housing, saturable magnetics and diode/varistor/capacitor subassemblies.

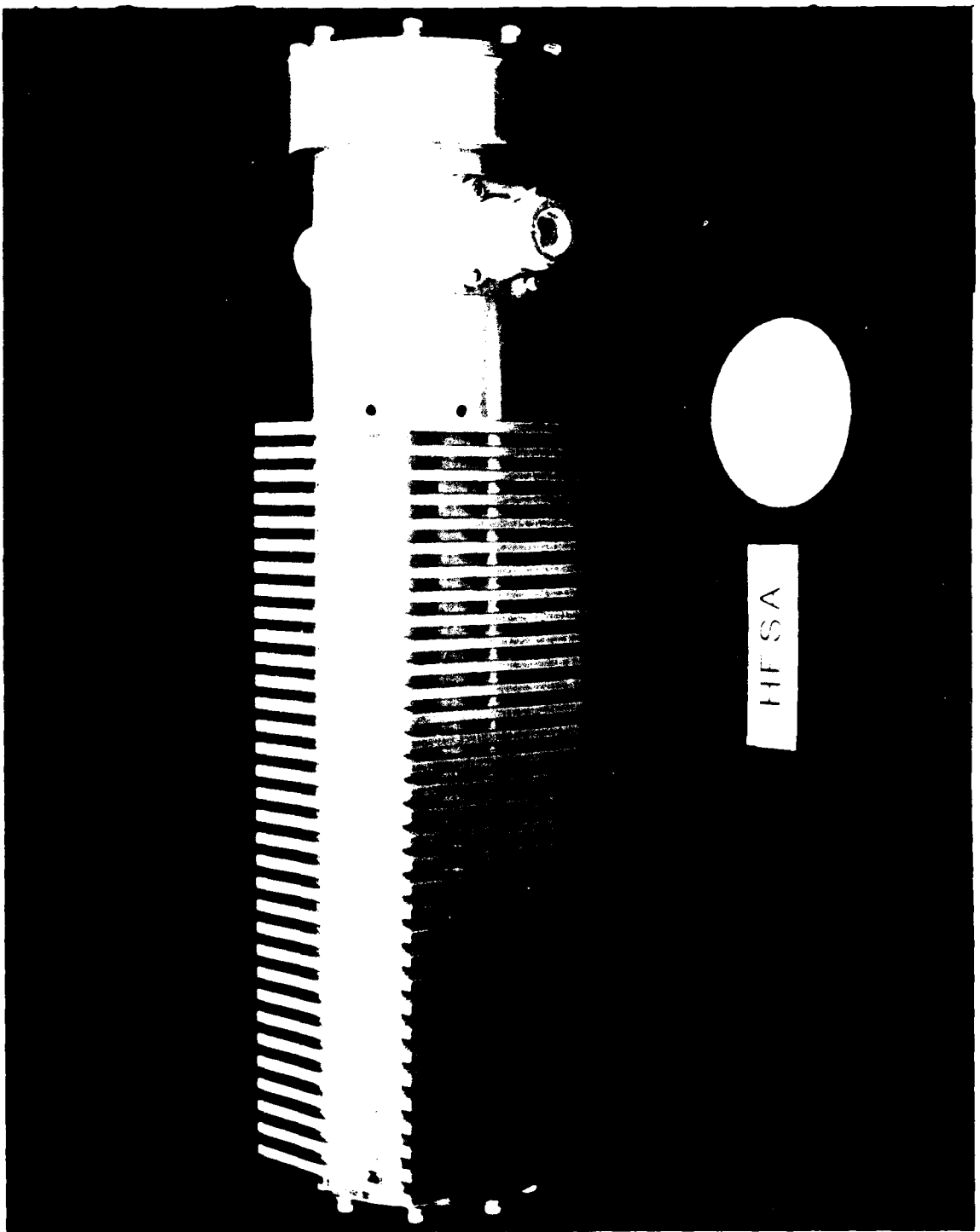


Figure 67. Completely assembled prototype HESA.

Table 4. Low level input impedance characteristics of a prototype HESA at various stages of assembly.

HESA CONFIGURATION	INPUT IMPEDANCE		
	FREQUENCY (MHz)	MAGNITUDE (OHMS)	PHASE (DEGREES)
1. SATURABLE MAGNETICS ONLY WITH OPEN CIRCUIT AT OUTPUT	1.0	40Ω	+88
	3.0	115	+82
	5.0	190	+78
	10.0	400	+70
	15.0	790	+52
	20.0	1.25K	+12
	21.0	1.3K	0
	25.0	1.05K	-34
	30.0	730	-54
2. SATURABLE MAGNETICS AND DIODE/VARISTOR STRINGS WITH OPEN CIRCUIT AT OUTPUT	1.0	40Ω	+85
	3.0	125	+80
	5.0	230	+74
	10.0	920	+23
	10.8	1K	0
	15.0	490	-62
	20.0	270	-74
	25.0	190	-78
	30.0	145	-80
3. COMPLETE HESA WITH OPEN CIRCUIT AT OUTPUT	1.0	42Ω	+88
	3.0	165	+77
	5.0	640	+22
	5.26	800	0
	10.0	135	-80
	15.0	73	-84
	20.0	50	-85
	25.0	37	-85
	30.0	30	-85
4. COMPLETE HESA WITH 50Ω AT OUTPUT	1.0	33Ω	+47
	3.0	46	+16
	5.0	47	+4
	5.8	46	0
	10.0	44	-15
	15.0	39	-28
	20.0	33	-35
	25.0	29	-42
	30.0	24	-45

Table 5. Medium power VSWR characteristics of a 50Ω terminated prototype HESA with internal capacitors removed.

FREQUENCY (MHz)	INCIDENT POWER (WATTS)	REFLECTED POWER (WATTS)	VSWR
2.0	100	6	1.65:1
3.0	100	3	1.42:1
5.0	100	~1.5	1.27:1
10.0	100	<1	1.22:1
15.0	100	<1	1.22:1
20.0	100	<1	1.22:1
25.0	100	<1	1.22:1
30.0	100	~1.5	1.27:1
35.0	100	2	1.34:1
40.0	100	~2.5	1.38:1
45.0	100	3.0	1.42:1
50.0	100	4.0	1.50:1
55.0	100	4.5	1.53:1
60.0	100	5.0	1.57:1
65.0	100	6.0	1.65:1

Table 6. Low power VSWR characteristics of a 50Ω terminated prototype HESA.

FREQUENCY (MHz)	INCIDENT POWER (WATTS)	REFLECTED POWER (WATTS)	VSWR
2.0	20	<0.5	<1.38:1
3.0	20	<0.5	<1.38:1
5.0	20	<0.5	<1.38:1
10.0	20	~1	1.56:1
15.0	20	2	2.17:1
20.0	20	4	2.64:1
25.0	20	6	3.35:1
30.0	20	7	3.87:1

SECTION 6

CONCLUSIONS AND RECOMMENDATIONS

The present program has shown that improved high energy surge arresters (HESA's) can be developed for practical RF/C³ applications. A unique and innovative all solid state, self recovery HESA design concept was developed using existing metal oxide varistor and saturable magnetic device technologies. Detailed analytical design equations were derived and extensive material characterizations were experimentally obtained in support of this development. Much of this work involved the generation of singular information which was required to support the solutions to a number of significant design problems encountered in meeting such a formidable design challenge using realistic hardware. Two proof-of-principle prototype units were designed and fabricated using the technology established in the program.

Based on the positive results obtained to date, and the interest exhibited by the survivability technical community, it is recommended that the Phase II portion of the program be initiated in order to establish detailed performance evaluations of the prototypes. Based on a successful conclusion of the Phase II work it would be further recommended that additional work be undertaken to optimize the performance characteristics achievable with the various elements comprising the HESA. It is envisioned that the HESA technology developed here can be transferred to use in operational systems once this is achieved.

SECTION 7

LIST OF REFERENCES

- 2.1 Private communications with G. Foster, et al, Hill Air Force Base, Ogden, Utah.
- 2.2 Private communications with M. Bell and A. Peterson, JAYCOR.
- 3.1 Tasca, D.M. and Peden, J.C., "EMP Surge Suppression Connectors Utilizing Metal Oxide Varistors," Final Technical Report, Contract No. DAAG39-72-C-0179, General Electric Report 73SD4293, December 1973, U.S. Army Harry Diamond Laboratory Report No. HDL-TR-179-1, August 1974.
- 3.2 Levinson, L.M. and Philip, H.R., "AC Properties of Metal Oxide Varistors," General Electric Report 75CRD175, September 1975.
- 3.3 Levinson, L.M. and Philip, H.R., "Metal Oxide Varistor -- A Multi-junction Thin-Film Device," General Electric Company Report 73CRD285, October 1973.
- 3.4 Martzloff, F.D., "Varistor Versus Environment: Winning the Rematch," General Electric Report 85CRD037, May 1985.
- 4.1 Kraus, J.D., "Electromagnetics," McGraw-Hill Book Company, Third Edition.
- 4.2 Jordan, E.C., "Electromagnetic Waves and Radiating Systems," Prentice-Hall Incorporated, Seventh Printing.
- 5.1 "Transient Voltage Suppression Manual," General Electric Company, Semiconductor Products Department, 1976.

DISTRIBUTION LIST

DEPARTMENT OF DEFENSE

ARMED FORCES STAFF COLLEGE
ATTN: LIBRARY

ASST SECY OF DEF CMD CONT COMM & INTEL
ATTN: ASST DIRECTOR (SYS)
ATTN: DASD(C3)
ATTN: DASD(I)
ATTN: DASD(I)
ATTN: DASD(P&R)

ASSISTANT SECRETARY OF DEFENSE
ATTN: DEP ASST SECY PROG DEV

ASSISTANT TO THE SECRETARY OF DEFENSE
ATTN: C31
ATTN: EXECUTIVE ASSISTANT

COMMANDER IN CHIEF, PACIFIC
ATTN: C3SRD

DEFENSE COMMUNICATIONS AGENCY
ATTN: COMMANDER

DEFENSE COMMUNICATIONS ENGINEER CENTER
ATTN: CODE R123 TECH LIB
ATTN: CODE R400
ATTN: CODE R720

DEFENSE INTELLIGENCE AGENCY
ATTN: DT SCI-TECH INTELL
ATTN: RTS-2A TECH LIB
ATTN: RTS-2B

DEFENSE NUCLEAR AGENCY
ATTN: RAAE
ATTN: RAEE
ATTN: RAEV
ATTN: STNA
ATTN: STRA
ATTN: STSP
4 CYS ATTN: STTI-CA

DEFENSE TECHNICAL INFORMATION CENTER
12 CYS ATTN: DD

FIELD COMMAND DNA DET 2
LAWRENCE LIVERMORE NATIONAL LAB
ATTN: FC-1

DNA PACOM LIAISON OFFICE
ATTN: DNA LNO
ATTN: DNA LNO

JOINT CHIEFS OF STAFF

ATTN: C3S EVAL OFFICE (HDOO)
ATTN: C3S, INFO SYSTEMS DIV
ATTN: J-3 NUC CONTINGENCY BR
ATTN: J-3 STRAT OPNS DIV
ATTN: J-5 NUCLEAR & CHEMICAL DIV
ATTN: JAD RM 1D936

JOINT STRAT TGT PLANNING STAFF

ATTN: JLAA
ATTN: JK (ATTN: DNA REP)
ATTN: JLKS
ATTN: JPPFA
ATTN: JPPFD
ATTN: JPSS
ATTN: JPTM
ATTN: JPTP

JOINT TACTICAL C3 AGENCY

ATTN: C3A-ARJS
ATTN: C3A-SES

NATIONAL COMMUNICATIONS SYSTEM

ATTN: NCS-TS

NATIONAL DEFENSE UNIVERSITY

ATTN: NWCO

NATIONAL SECURITY AGENCY

ATTN: CHIEF A GROUP

OFFICE OF THE SEC OF DEFENSE

ATTN: DOCUMENT CONTROL

U S EUROPEAN COMMAND/ECC3S-CC

ATTN: ECC3S-CC

U S FORCES KOREA

ATTN: DJ-AM-M
ATTN: EACJ-PON-NO

U S NATIONAL MILITARY REPRESENTATIVE

ATTN: U S DOCUMENTS OFFICER

UNDER SECY OF DEF FOR RSCH & ENGRG

ATTN: DEPUNDSEC COM SYS
ATTN: DEPUNDSEC C3I-STRATEGIC & C2 SYS
ATTN: STRAT & SPACE SYS (OS)
ATTN: STRAT & THEATER NUC FOR F VAJDA
ATTN: TACTICAL WARFARE PROG

DEPARTMENT OF THE ARMY	
DEFENSE COMMUNICATIONS SYSTEMS ATTN: DRCPM-COM-W-D	U S ARMY ENGINEER DIV HUNTSVILLE ATTN: HNDED-SR
DEP CH OF STAFF FOR OPS & PLANS ATTN: DAMO-ODW	U S ARMY INFO SYS ENGINEERING SUP ACT ATTN: ASBH-SES
DEP CH OF STAFF FOR RSCH DEV & ACQ ATTN: DAMA-CSM-N	U S ARMY INFORMATION SYS MNGT AGENCY ATTN: CCM-AD-LB LIBRARY
HARRY DIAMOND LABORATORIES ATTN: CHIEF DIV 10000 ATTN: SCHLD-NW-P ATTN: SLCHD-NE-EB ATTN: SLCHD-NW	U S ARMY INTELLIGENCE CENTER & SCHOOL ATTN: ATSI-CD-MD
2 CYS ATTN: SLCHD-NW-E ATTN: SLCHD-NW-EA 21100 ATTN: SLCHD-NW-ED ATTN: SLCHD-NW-EE ATTN: SLCHD-NW-R ATTN: SLCHD-NW-RA ATTN: SLCHD-NW-RC ATTN: SLCHD-NW-RH G MERKEL ATTN: SLCHD-NW-RH R GILBERT 22800 ATTN: SLCHD-NW-RJ G HUTTLIN ATTN: SLCIS-IM-TL 81100 TECH LIB	U S ARMY MATERIAL COMMAND ATTN: DRXAM-TL TECH LIB
HQ DEPARTMENT OF THE ARMY ATTN: DAMO-TCV-A	U S ARMY MATERIEL SYS ANALYSIS ACTVY ATTN: AMXSY-CR
JOINT MANAGEMENT OFFICE ATTN: JMO-TCS	U S ARMY NUCLEAR & CHEMICAL AGENCY ATTN: LIBRARY
RESEARCH & DEV CENTER ATTN: DRCPM-ATC ATTN: DRCPM-TDS-SD	U S ARMY STRATEGIC DEFENSE CMD ATTN: DACS-BM J KAHLAS
U S ARMY ARMOR CENTER ATTN: TECHNICAL LIBRARY	U S ARMY STRATEGIC DEFENSE CMD ATTN: DASD-H-SAV
U S ARMY ATMOSPHERIC SCIENCES LAB ATTN: SLCAS-AS	U S ARMY STRATEGIC DEFENSE COMMAND ATTN: ATC-R ATTN: ATC-T
U S ARMY BALLISTIC RESEARCH LAB ATTN: SLCBR-SS-T TECH LIB ATTN: SLCBR-VL	U S ARMY TEST AND EVALUATION COMD ATTN: TECH LIBRARY SI-F
U S ARMY BELVOIR RD & E CTR ATTN: STRBE-BT TECH LIB	U S ARMY TRADOC SYS ANALYSIS ACTVY ATTN: ATAA-TAC
U S ARMY COMB ARMS COMBAT DEV ACTY ATTN: ATZL-CAC-A ATTN: ATZL-CAN-I ATTN: ATZL-CAP	U S ARMY WAR COLLEGE ATTN: LIBRARY
U S ARMY COMD & GENERAL STAFF COLLEGE ATTN: LIBRARY	U S ARMY MISSILE COMMAND ATTN: AMSMI-RD-GC-P ATTN: AMSMI-SF ATTN: REDSTONE SCI INFO CTR
	DEPARTMENT OF THE NAVY
	NAVAL AIR SYSTEMS COMMAND ATTN: AIR 350F ATTN: AIR 5161
	NAVAL FACILITIES ENGINEERING COMMAND ATTN: 04E
	NAVAL OCEAN SYSTEMS CENTER ATTN: CODE 9642 TECH LIB
	NAVAL POSTGRADUATE SCHOOL ATTN: CODE 1424 LIBRARY

DEPARTMENT OF THE NAVY (CONTINUED)

NAVAL RESEARCH LABORATORY
ATTN: CODE 2627 TECH LIB

NAVAL SURFACE WEAPONS CENTER
ATTN: CODE R40
ATTN: CODE R43
ATTN: CODE 425

NAVAL SURFACE WEAPONS CENTER
ATTN: CODE H-21

NAVAL WEAPONS CENTER
ATTN: CODE 343 FKA6A2 TECH SVCS

OFC OF THE DEPUTY CHIEF OF NAVAL OPS
ATTN: NOP 098 OFC RES-DEV-TEST & EVAL
ATTN: NOP 506
ATTN: NOP 551
ATTN: NOP 654 STRAT EVAL & ANAL BR
ATTN: NOP 94
ATTN: NOP 981
ATTN: NOP 981N1

OFFICE OF NAVAL RESEARCH
ATTN: CODE 1114

SPACE & NAVAL WARFARE SYSTEMS CMD
ATTN: PME 117-21
ATTN: TECHNICAL LIBRARY

STRATEGIC SYSTEMS PROGRAMS(PM-1)
ATTN: NSP-L63 TECH LIB

THEATER NUCLEAR WARFARE PROGRAM OFC
ATTN: PMS 423

U S NAVAL FORCES, EUROPE
ATTN: N54

DEPARTMENT OF THE AIR FORCE

AERONAUTICAL SYSTEMS DIVISION, AFSC
ATTN: ASD/ENES P MARTH
ATTN: ASD/ENSSA
ATTN: ASD/YYEF

AIR FORCE/INE
ATTN: INA

AIR FORCE AERONAUTICAL SYS DIV/ENACE
ATTN: AFWAL/FIEA
ATTN: ASD/ENACE

AIR FORCE COMMUNICATIONS COMMAND
ATTN: C JAROCKI
ATTN: LG

AIR FORCE CTR FOR STUDIES & ANALYSIS
ATTN: AFCSA/SAMI R GRIFFIN

AIR FORCE GEOPHYSICS LABORATORY
ATTN: SULL

AIR FORCE INSTITUTE OF TECHNOLOGY/EN
ATTN: LIBRARY/AFIT/LDEE

AIR FORCE SPACE COMMAND
ATTN: LKA

AIR FORCE WEAPONS LABORATORY, AFSC
ATTN: NT
ATTN: NTAA
ATTN: NTYC
ATTN: SUL

AIR UNIVERSITY LIBRARY
ATTN: AUL-LSE

BALLISTIC MISSILE OFFICE/DAA
ATTN: ENSN

DEPUTY CHIEF OF STAFF
ATTN: LEEEU

DEPUTY CHIEF OF STAFF/AF-RDQI
ATTN: AF/RDQI

DEPUTY CHIEF OF STAFF/AFRDS
ATTN: AFRDS SPACE SYS & C3 DIR

DEPUTY CHIEF OF STAFF/XOX
ATTN: AFXOXM PLNS FRC DEV MUN PLNS

ELECTRONIC SYSTEMS DIVISION/SC
ATTN: SCS-1E

HEADQUARTERS U S AIR FORCES IN EUROPE/LG
ATTN: XPXF

NORAD
ATTN: NORAD/J5YX

ROME AIR DEVELOPMENT CENTER, AFSC
ATTN: TSLD

SPACE COMMAND/DE
ATTN: DEE

SPACE DIVISION/IN
ATTN: IND

SPACE DIVISION/YA
ATTN: YAR

STRATEGIC AIR COMMAND/DEPR
ATTN: DEPR

STRATEGIC AIR COMMAND/DOCSD
ATTN: DOCSD

DEPARTMENT OF THE AIR FORCE (CONTINUED)

STRATEGIC AIR COMMAND/INA
ATTN: INA

STRATEGIC AIR COMMAND/NRI-STINFO
ATTN: NRI/STINFO

STRATEGIC AIR COMMAND/SIP
ATTN: SAC/SIPA

STRATEGIC AIR COMMAND/XPFC
ATTN: XPFC

STRATEGIC AIR COMMAND/XPQ
ATTN: XPQ

TACTICAL AIR COMMAND/XPJ
ATTN: TAC/XPJ

U S RESEARCH & DEVELOPMENT COORD
ATTN: USRADCO

DEPARTMENT OF ENERGY

EMERGENCY ELECTRIC POWER ADM
ATTN: LIBRARY

UNIVERSITY OF CALIFORNIA
LAWRENCE LIVERMORE NATIONAL LAB
ATTN: L-53 TECH INFO DEPT LIB

LOS ALAMOS NATIONAL LABORATORY
ATTN: MS P364 REPORT LIBRARY

SANDIA NATIONAL LABORATORIES
ATTN: TECH LIB 3141 RPTS RCVG CLRK

OTHER GOVERNMENT

CENTRAL INTELLIGENCE AGENCY
ATTN: OSR/SE/C
ATTN: OSR/SE/F
ATTN: OSWR/NED
ATTN: OSWR/STD/MTB

FEDERAL EMERGENCY MANAGEMENT AGENCY
ATTN: SL-EM

NATIONAL BUREAU OF STANDARDS
ATTN: 723.03

DEPARTMENT OF DEFENSE CONTRACTORS

AGBABIAN ASSOCIATES, INC
ATTN: LIBRARY

ALLIED CORP
ATTN: DOCUMENT CONTROL

AT&T TECHNOLOGIES, INC
ATTN: W EDWARDS

BDM CORP
ATTN: CORPORATE LIB

BDM CORP
ATTN: LIBRARY

BOEING CO
ATTN: M/S 2R-00 D EGELKROUT
ATTN: M/S 82-09 R SCHEPPE
ATTN: M/S 83-66 H WICKLEIN

BOEING MILITARY AIRPLANE CO
ATTN: C SUTTER

BOOZ-ALLEN & HAMILTON, INC
ATTN: TECHNICAL LIBRARY

BOOZ-ALLEN & HAMILTON, INC
ATTN: L ALBRIGHT

BOOZ-ALLEN & HAMILTON, INC
ATTN: D DURGIN

CALSPAN CORP
ATTN: LIBRARY

COMPUTER SCIENCES CORP
ATTN: A SCHIFF

DIKEWOOD CORP
ATTN: K LEE

E-SYSTEMS, INC
ATTN: J F STOSIC

E-SYSTEMS, INC
ATTN: J MOORE

EG&G WASH ANALYTICAL SVCS CTR, INC
ATTN: A BONHAM
ATTN: C GILES

ELECTRO-MAGNETIC APPLICATIONS, INC
ATTN: D MEREWETHER

GENERAL ELECTRIC CO
2 CYS ATTN: D TASCA

GENERAL ELECTRIC CO
ATTN: C HEWISON

GRUMMAN AEROSPACE CORP
ATTN: L-01 35 TECH INFO CENTER

GTE GOVERNMENT SYSTEMS CORPORATION
ATTN: TECH LIBRARY

DEPT OF DEFENSE CONTRACTORS (CONTINUED)

HARRIS CORP
ATTN: T W TOMBLER

HERCULES, INC
ATTN: W WOODRUFF

HONEYWELL, INC
ATTN: S&RC LIBRARY

HONEYWELL, INC
ATTN: LIBRARY

HUGHES AIRCRAFT CO
ATTN: CO TECH DOC CTR

IIT RESEARCH INSTITUTE
ATTN: I MINDEL

INSTITUTE FOR DEFENSE ANALYSES
ATTN: CLASSIFIED LIBRARY
ATTN: TECH INFO SERVICES

JRT CORP
ATTN: B WILLIAMS
ATTN: R W STEWART

ITT TELECOMMUNICATIONS CORP
ATTN: R SCHWALLIE

JAYCOR
ATTN: E WENAAS

JAYCOR
ATTN: LIBRARY

JOHNS HOPKINS UNIVERSITY
ATTN: P PARTRIDGE

KAMAN SCIENCES CORP
ATTN: LIBRARY

KAMAN SCIENCES CORP
ATTN: E CONRAD

KAMAN SCIENCES CORPORATION
ATTN: TECHNICAL LIBRARY

KAMAN TEMPO
ATTN: DASIA
ATTN: R RUTHERFORD

KAMAN TEMPO
ATTN: DASIA

LITTON SYSTEMS, INC
ATTN: E EUSTIS

LITTON SYSTEMS, INC
ATTN: J SKAGGS

LOCKHEED MISSILES & SPACE CO, INC
ATTN: TECH INFO CTR D/COLL

LTV AEROSPACE & DEFENSE COMPANY
ATTN: LIBRARY

LUTECH, INC
ATTN: F TESCHE

MCDONNELL DOUGLAS CORP
ATTN: TECHNICAL LIBRARY

METATECH CORP
ATTN: R SCHAEFER

METATECH CORPORATION
ATTN: W RADASKY

MISSION RESEARCH CORP
ATTN: EMP GROUP

MISSION RESEARCH CORP
ATTN: J LUBELL
ATTN: J R CURRY

MISSION RESEARCH CORP, SAN DIEGO
ATTN: V VAN LINT

MITRE CORP
ATTN: M FITZGERALD

PACIFIC-SIERRA RESEARCH CORP
ATTN: H BRODE, CHAIRMAN SAGE

PHOTOMETRICS, INC
ATTN: I L KOFSKY

PHYSICS INTERNATIONAL CO
ATTN: DOCUMENT CONTROL

R & D ASSOCIATES
ATTN: DOCUMENT CONTROL
ATTN: W KARZAS

R & D ASSOCIATES
ATTN: LIBRARY

RAYTHEON CO
ATTN: H FLESCHER

RCA CORP
ATTN: G BRUCKER

RESEARCH TRIANGLE INSTITUTE
ATTN: M SIMONS

ROCKWELL INTERNATIONAL CORP
ATTN: G MORGAN
ATTN: J ERB

DEPT OF DEFENSE CONTRACTORS (CONTINUED)

ROCKWELL INTERNATIONAL CORP
ATTN: B-1 DIV TIC (BAOB)

S-CUBED
ATTN: A WILSON

SCIENCE & ENGRG ASSOCIATES, INC
ATTN: V JONES

SCIENCE APPLICATIONS INTL CORP
ATTN: W CHADSEY

SCIENCE APPLICATIONS, INC
ATTN: E ODONNELL
ATTN: P J DOWLING

SINGER CO
ATTN: TECH INFO CENTER

SPERRY CORP
ATTN: R LAZARCHIK

SPERRY CORP
ATTN: J INDA

SPERRY CORP
ATTN: TECHNICAL LIBRARY

SRI INTERNATIONAL
ATTN: A PADGETT

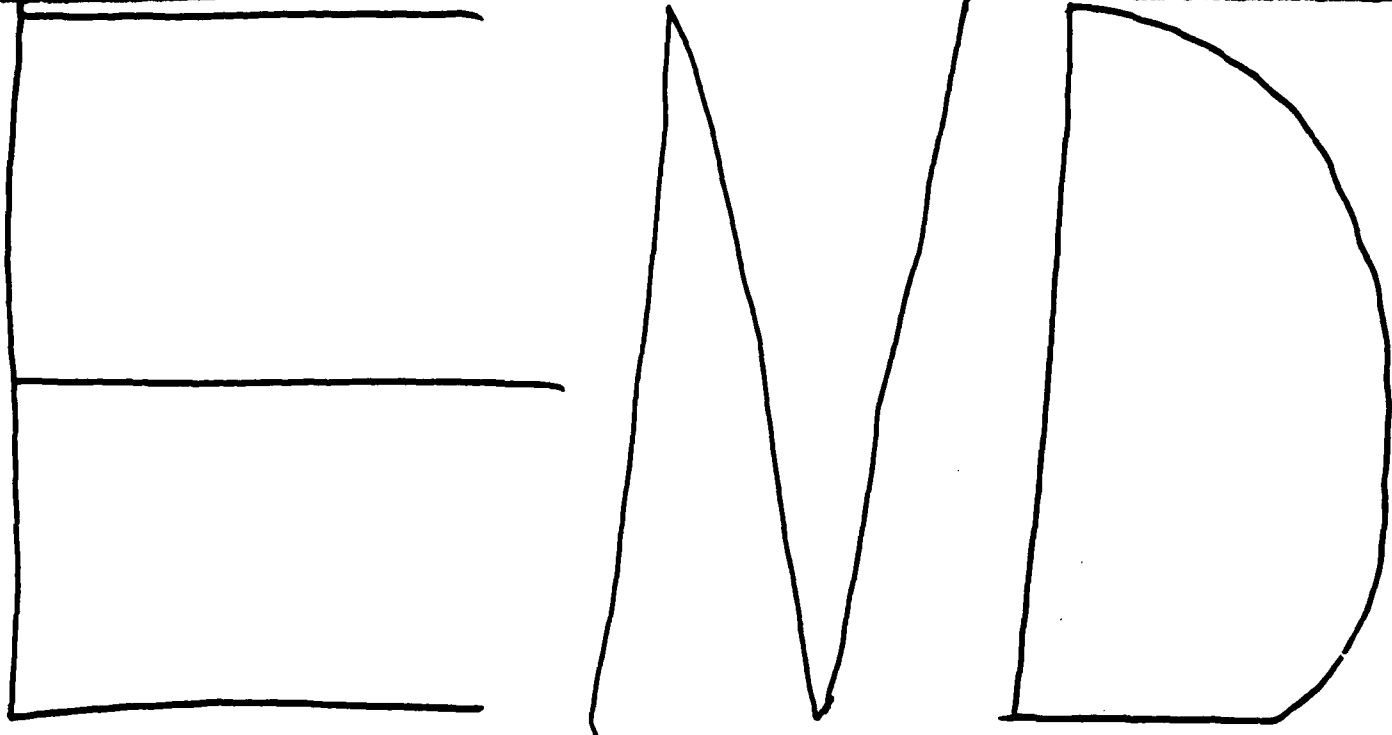
TELEDYNE BROWN ENGINEERING
ATTN: F LEOPARD

TEXAS INSTRUMENTS, INC
ATTN: TECHNICAL LIBRARY

TRW ELECTRONICS & DEFENSE SECTOR
ATTN: J BROSSIER
ATTN: J PENAR

TRW ELECTRONICS & DEFENSE SECTOR
ATTN: R HENDRICKSON

TRW ELECTRONICS & DEFENSE SECTOR
ATTN: LIBRARIAN



12-86

